論文 / 著書情報
Article / Book Information

題目(和文)	スメクティック液晶における電荷輸送のモデル化
Title(English)	Modeling of charge carrier transport in smectic mesophases
著者(和文)	大野玲
Author(English)	akira oono
出典(和文)	学位:博士(理学), 学位授与機関:東京工業大学, 報告番号:甲第5672号, 授与年月日:2004年3月26日, 学位の種別:課程博士, 審査員:
Citation(English)	Degree:Doctor (Science), Conferring organization: Tokyo Institute of Technology, Report number:甲第5672号, Conferred date:2004/3/26, Degree Type:Course doctor, Examiner:
学位種別(和文)	博士論文
Type(English)	Doctoral Thesis

Modeling of Charge Carrier Transport in Smectic Mesophases

2004

Akira Ohno

Department of Information Processing
Tokyo Institute of Technology

Contents

Chapter 1

Introduction

1.1 Motivations and Background

Organic molecular materials, crystalline or amorphous, are essentially composed of organic molecules which, even in the condensed phase, preserve their physical identity well. In organic crystals, the electronic-energy state is known to form a band structure with only small band gaps of the order of 100meV. Electronic transport is well described by a band model, and charge mobility is field independent [1-3]. For amorphous (or disordered) organic materials such as polymers, molecularly doped polymers, and glasses, the features of isolated molecules are more pronounced than in crystals. Electronic transport is well described by a random walk by electrons and holes consisting of a series of thermally activated hops between the isolated molecules. Characteristics of hopping conductivity in these systems, such as the electric-field and temperature dependence of the mobility, has been studied for over three decades by experimental approaches [4-6], theoretical approaches [7,8] and numerical simulations [9-11].

Another important class of organic materials which have been used as electro-optical materials are the liquid crystals. Liquid crystalline materials represent an intermediate class of materials between single crystals and amorphous disordered materials, and have only recently received attention [12-17]. The interest in liquid crystals stems from the numerous potential applications where electronic charge

generation and transport processes are involved. However, the charge transport mechanism in liquid crystals is not well understood and there is no comprehensive charge transport theory available at present.

Liquid crystals have the electronic properties of both crystalline and amorphous materials because they exhibit complicated features depending on the molecular structure of constituents and also on the condensation conditions such as temperature, pressure, existing impurities, and applied electric field. In this respect, it is of interest here that recent studies by Funahashi and Hanna and others have shown that some liquid crystals exhibit remarkably fast electronic conduction. The mobility obtained were over 10^{-2} cm^2/Vs in columnar mesophases of discotic (disk like) liquid crystals [18-20] and also in smectic mesophases of calamitic (rod like) ones [21,22], whose charge transport, especially in the calamitics, had been believed to be ionic inherently for a long time because of its liquid-like fluidity.

In addition to above mentioned features, which are of interest from the fundamental point of view, the liquid crystals enable cheap, lightweight, portable, and large area

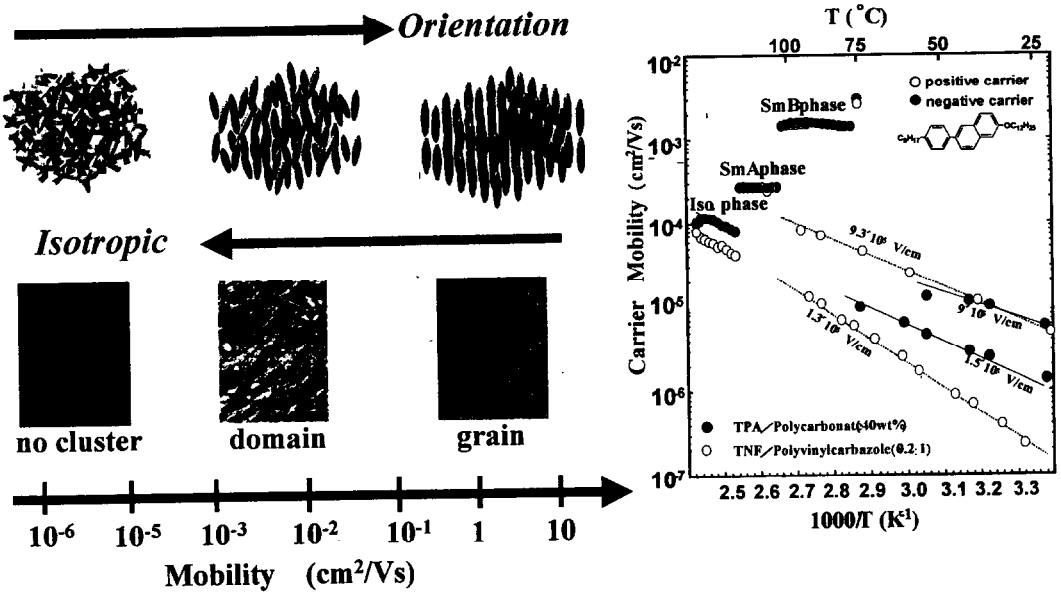

Fig. 1.1 Liquid Crystalline Semiconductor

displays, with promising applications for various fields. Very attractive electronic behaviors are reported that seldom happen in the disordered solids, such as bipolar carrier transport [22] and field- and temperature-independent mobility [22-24]. The liquid crystal is being recognized as an important new class of molecular semiconductors, i.e., self-organizing molecular semiconductor. Self-organizing organic semiconductors will possibly find useful applications in fabricating new devices. Ordered organic molecular materials exhibiting high charge carrier mobility and stable current may provide new LEDs. They may also be used for LC-displays without back light, and possibly for use as plastic lasing materials.

Electronic transport in organic solids is generally slow because exchange of a conduction electron or hole between neighboring molecules is not a very efficient process. The mobilities of such systems are low and exhibit a strong temperature and electric field dependence. Thus, previous studies [21-24] have focused on charge transport mainly attributable to hopping. However, high carrier mobilities, varying only weakly with electric field, are generally desirable for application purposes. For this purpose, it is essential to fully understand the fundamental physics of electrical transport through liquid crystals.

1.2 Aims of this Study

The purpose of the present work is to fully understand the fundamental physics of charge transport in liquid crystalline phases, particularly in smectic mesophases. Molecules in smectic mesophases are known to form two-dimensional molecular layers. We can investigate transport property in the materials with regard to molecular movement or orientation as mentioned in a previous section. The method for this

study is to employ time-of-flight (TOF) technique to observe transient current-time curve for the liquid crystalline sample and attempt to understand the physics of charge transport by using the multiple-trapping model (MTM) to analyze the experimentally-observed phenomena (phenomenological approach) and also by using Monte Carlo simulation to examine the validity of disorder model (microscopic approach).

In TOF experiments for the liquid crystalline phases, the sample is sandwiched between two blocking electrodes. A laser-pulse generates charge carriers near the top electrode and these charges are swept toward the counter electrode under applied electric fields, while the current being recorded. The transit time at which most of the charges arrive at the counter electrode may be measured, from which the mobility may be determined.

The multiple trapping model is a heuristic description of charge transport, in which the hopping sites are divided into two groups, the free sites between which transport can take place, and the trap sites into which charges may become immobilized for long periods of time. Its advantage is that it is analytically tractable, and lends itself easily to comparison with experimental data. Its disadvantage is that in the real system the distinction between free states and trap states may become blurred. The method of Monte Carlo simulation is superior to the MTM in that it enables us to study the exact microscopic aspect of charge carrier transport in the materials and how it depends on possible models for the underlying hopping rate. Its disadvantage is that it is more difficult to make quantitative comparisons with experimental data.

1.3 Contents of the Thesis

The present thesis is composed of three parts: The first part includes Chapters 1 and 2. Chapter 1 describes the backgrounds, research motivations, and aims of the work. Chapter 2 summarizes the properties of smectic liquid crystals as promising new electronic organic materials, and charge transport mechanisms in crystalline and amorphous organic solids which have already been studied, together with consideration of the predicted charge transport properties in liquid crystals. The validity of the Time-Of-Flight measurement for use as evaluation method of charge transport properties in materials will be discussed.

The second part includes Chapters 3, 4, and 5. Here, an attempt is made to analyze the information obtained from the experimental TOF-photocurrents on the basis of multiple-trapping model (MTM). In Chapter 3 we discuss charge transport due to hole migration in smectic-liquid phases, comparing the calculated results with experiments. A field-independent mobility which is consistent with the Einstein relation was found for the first time for smectic phases in low electric field region. This has never before been observed for disordered organic solids. In Chapter 4, experimental finding of ionic transport_occurring in smectic phases is demonstrated. We introduce a useful model to clarify the phenomenon and distinguish electron transport from ionic transport. In Chapter 5 we introduce a new method based on the MTM for obtaining the trap-density distribution in the material from transient TOF-photocurrent decay curve. We demonstrate this procedure by applying it to measurements taken on the smectic phase.

The third includes Chapters 6 and 7., Here we attempt to deterimine what aspect of disorder is dominant in determining carrier dynamics. This is followed by a presentation of the useful results obtained in this work for fabrication of new electronic devices.

References

[1] E. A. Silinsh and V. Čápek, *Organic Molecular Crystals* (American Inst. of Phys, New York, 1994)

[2] R. Farchioni and G. Grosso (Eds.) *Organic Electronic Materials* (Springer-Verlag, Berlin Heiderberg New York, 2001)

[3] J.-P. Farges *Organic conductors : fundamentals and applications* (Marcel Dekker, New York, 1994)

[4] W. D. Gill and G. Pfister, J. Appl. Phys. **43**, 5033 (1973).

[5] G. Pfister, Phys. Rev. B. **16**, 3676 (1977).

[6] G. Pfister and C. H. Griffiths, Phys. Rev. Lett. **40**, 659 (1978).

[7] B. Derrida, J. Stat. Phys. **31**, 433 (1982).

[8] D. H. Dunlap, P. E. Parris, and V. M. Kenkre, Phys. Rev. Lett. **77**, 542 (1996).

[9] H. Bassler, Phys. Status Solidi B **175**, 15 (1993).

[10] D. Hertel, H. Bassler, U. Scerf, and H. H. Horhold, J. Chem. Phys. **110**, 9214 (1999).

[11] Y. N. Garstein and E. M. Conwell, J. Chem. Phys. **100**, 9175 (1994).

[12] D. Demus, J. Goodby, G. W. Grey, H. W. Spiess, and V. Vill, *Handbook of Liquid Crystals*, (Wiley-VCH, Weinheim, 1998)

[13] D. Demus, J. Goodby, G. W. Grey, H. W. Spiess, and V. Vill, *Physical Properties of Liquid Crystal*, (Wiley-VCH, Weinheim, 1999).

[14] S. Chandrasekhar and S. K. Prasad, Contemp. Phys. **40**, 237 (1999).

[15] S. M. Kelly and M O'Neil, *Handbook of Advanced Electronic and Photonic Materials* (ed. H. S. Nalwa, Academic Press, San Diego, CA, 2000)

[16] I. Shiyanovskaya, K. D. Singer, R. J. Twieg, L. Sukhomlinova, and V. Gettwert, Phys. Rev. E **65**, 41715 (2002).

[17] M. O'Neill and S. M. Kelly, Adv. Mater. **15**, 1135 (2003).

[18] D. Adam, F. Closs, T. Frey, D. Funfoff, D. Haarer, H. Ringsdorf, P. Scuhmacher, and K. Siemensmeyer, Phys. Rev. Lett. **70**, 457 (1993).

[19] D. Adam, P. Scuhmacher, L. Haussling, K. Siemensmeyer, K. H. Etzbach, D. Haarer, H. and H. Ringsdorf, Nature **371**, 141 (1994).

[20]J. Simmerer, B. Glusen, W. Paulus, A. Kettner, P. Schuhmacher, D. Adam, K. H. Etzbach, K. Siemensmeyer, J. H. Wendorf, H. Ringsdorf, and D. Haarer, Adv. Mater. **8**, 815 (1996).

[21] M. Funahashi and J. Hanna, Jpn. J. Appl. Phys., Part 2 **35**, L703 (1996).

[22] M. Funahashi and J. Hanna, Appl. Phys. Lett. **71**, 602 (1997).

[23] M. Funahashi and J. Hanna, Phys. Rev. Lett. **78**, 2184 (1997).

[24] M. Funahashi and J. Hanna, Mol. Cryst. Liq. Cryst. **304**, 429 (1997).

Chapter 2

Charge Migration in Liquid Crystals

2.1 Introduction

In this section we introduce the structure and properties of liquid crystals with particular emphasis on smectic liquid crystals (SmLCs). We then discuss the general electrical transport properties of disordered organic materials. We assume that the mechanisms for hopping transport process in disordered organic materials are also applicable for SmLC. Although smectic liquid crystals have molecular orientation, the reason that band-like transport does not occur, at least for a scale larger than tens of angstrom, is because the long-translational order is broken by thermal fluctuations [1-5]. Measurements in TOF experiments show that the mobility is independent of the field and temperature [6]. This feature is completely different from organic disorder materials. However, we need to be careful in our interpretation of the TOF measurement, because most of photocurrent signals are broadened by diffusion and trapping process of charge migration. The analytical method for extracting the information of carrier transport in SmLC is presented on chapter 3. Here, we also show the experimental set up of TOF and the experimental result. The results are useful for understanding the carrier transport in SmLC.

The procedure of this chapter is therefore as follows. First we introduce the materials of liquid crystals which show electronic conduction. Then we explain the significance of the TOF measurement, the TOF experiment set up, and the experimental result. Finally, we review the carrier transport properties of conventional organic disordered materials, for comparison with the properties of SmLC.

2.2 Smectic Liquid Crystals

2.2.1 Liquid Crystal Showing Charge Conduction

Liquid crystals having electronic conduction were only found in the past decade, and include the following types: discotic LC [7-11], smectic LC [5,12] and Polimeric LC [13,14] (Fig. 2.1).

Discotic materials consist of molecules with a flat, disk-like aromatic core which is due to the fact that the orbital overlap between the p-orbitals of adjacent core atoms is optimal for a planer conformation. This results in extensive molecular π-orbitals, above and below the plane of disk, in which the p-electrons are delocalized. Peripherical substitution of these aromatic macrocycles with long hydrocarbon chains can result in materials with mesomorphic properties. Thus, in addition to a crystalline solid phase, they often display an

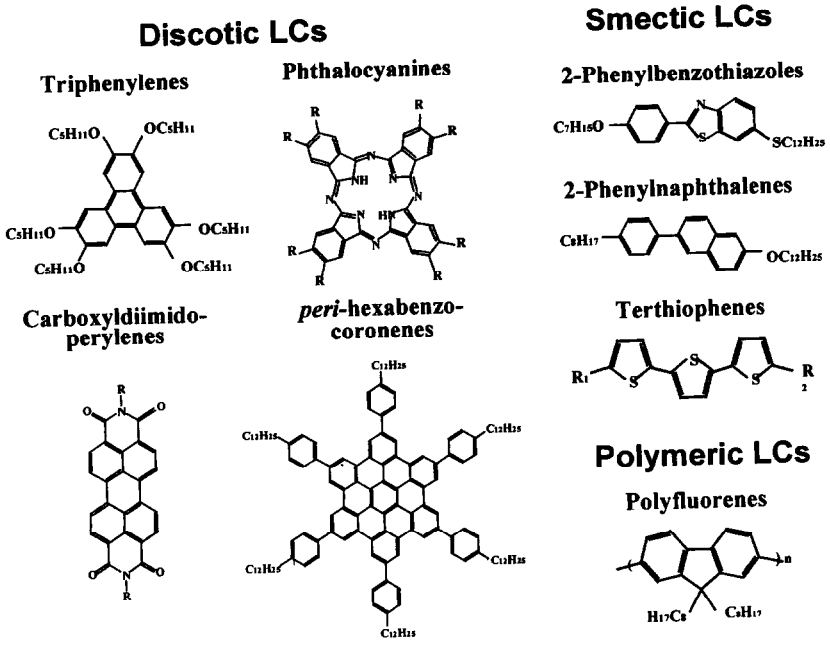

Fig. 2.1 :Typical Liquid crystals showing electrical conduction

intermediate liquid crystalline phase prior to melting to an isotropic liquid phase [15]. The dischotic mesophase has the ability to form self-assembling, one-dimensional conducting pathways. The molecules self-organize into long columnar stacks which are packed in a two-dimensional hexagonal lattice (Fig.2.2-(a)). With in the columnar aggregates, the π-systems of neighboring aromatic cores overlap and a one-dimensional pathway for charge transport along the axis of the columns is created. The resulting "molecular wires" are coaxially insulated from each other by their long hydrocarbon chains.

Smectic materials also consist of molecules with a flat, aromatic core. But this time, the core component is not disk-like. The molecules have a rod-like component with long hydrocarbon chains on both sides of a core component. This results in also extensive molecular π-orbitals, above and below the plane of the core component in which the p-electrons are delocalised. Peripherial substitution of these aromatic macrocycles with long hydrocarbon chains can result in materials with mesomorphic properties. They often display an intermediate liquid crystalline phase prior to melting to the isotropic liquid. The molecules of the smectic mesophase also self-organize, but this time, they are packed in a two-dimensional plane layer structure (Fig.2.2-(b)). In the SmA phase, molecules are

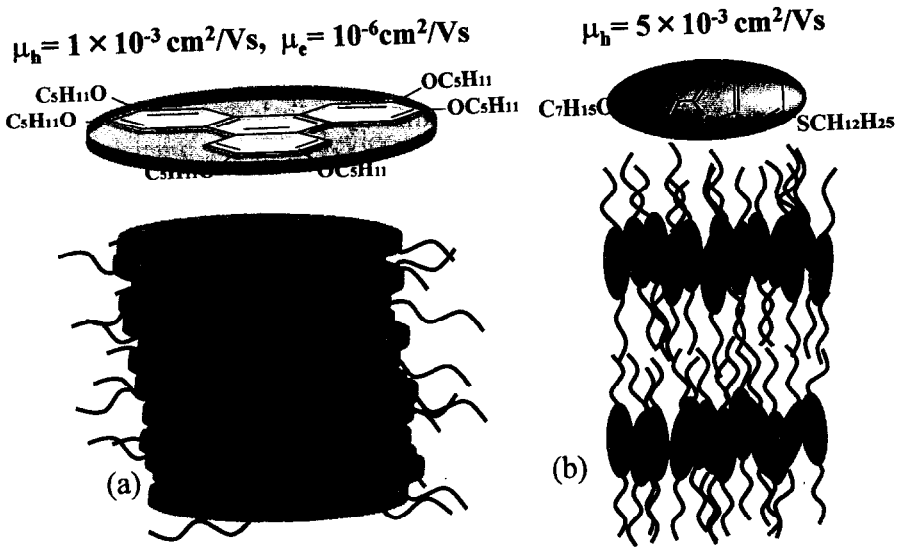

Fig. 2.2 :Discotic LC and Smectic LC: Self-assembly of disk-like and rod-like molecules

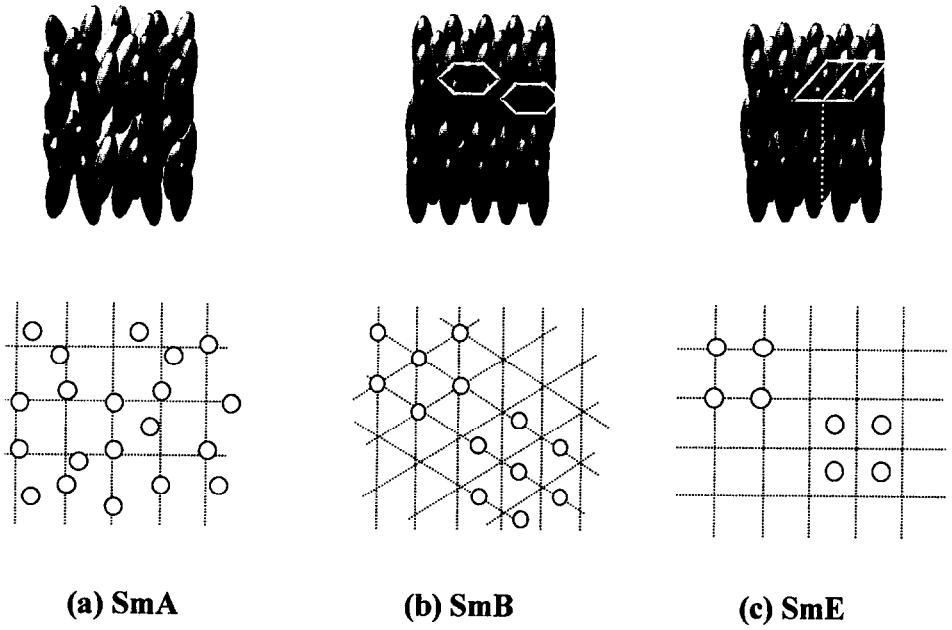

Fig. 2.2 :Smectic mesophases and molecular alignment

aligned randomly in the layer with a perpendicular orientation to the plane. The SmB phase and SmE phase form self-assembling and two-dimensional conducting pathways. The molecules are aligned in a hexagonal and rectangular lattice in the layer, respectively. Within the aggregates, the π-systems of neighboring aromatic cores overlap, and a two-dimensional pathway for charge transport along the plane layer is created. The resulting "molecular planes" are insulated from each other by their long hydrocarbon chains.

2.2.2 Molecular alignment in Smectic phase [1-5]

As we discussed previously, the primary feature of the smectic mesophase is that the molecules stack with layer structure. In the SmA phase, their alignment in the layer is random, as it would be in a liquid. On the other hand they behave elastically for the other direction. The long range order of the layer structure, however, is broken by root-mean square of positional fluctuation (**Landau-Peierls instability**) whose radial distribution function decays as $\sim r^{-\eta}$ where r is the distance between molecules and η is the exponent depending on temperature. On the other hand, in the SmB and SmE phases, the molecules

have a long-range order of bonding-orientation and a short-range order of translation; the direction of the bond between molecules has long-range order, but the order of translation is broken at a few times the intermolecular distance. The layer structure also shows Landau-Peierls instability. There is no inherent periodic alignment in the layer. (Fig.2.2)

2.3 Detection Techniques of Charge Migration [16,17]

The movement of charges in the medium needs to be proved for understanding the charge migration. Several detection techniques have been developed, some of which make use of a constant electric field (dc) and others implementing an oscillating electric field (ac). The dc techniques use a pulsed excitation, and rely on a time-resolved measurement. An ac field can be established with a contacting electrode, or by means of microwave radiation. Here we discuss dc techniques.

2.3.1 Carrier Densities and Detection

The processes of charge injection and carrier transport govern the electrical characteristics of organic electric devices. Without charge injection, disordered organic materials have negligible intrinsic carrier concentrations and a very high room temperature resistivity. One way to introduce charges is through optical generation of electron-hole pairs which dissociated under the applied field. Two general approaches are then used to measure the carrier mobility:

(1) Measuring the transit time across thin films [18,19].

(2) Fitting the I-V curve of diodes or FETs [20-23].

Although charge carriers can also be introduced into organic materials by doping, the dopant ions significantly modify the intrinsic electronic transport properties. Consequently, introducing excess charges in this manner is not particularly helpful for understandig the intrinsic mechanisms for carrier transport [24]. Conventional Hall effect measurements

have also not been useful for determining carrier mobilities in these insulating organic materials and photo-Hall measurements are complicated by short carrier lifetimes and relatively large exciton binding energies. Hopping transport in a disordered organic material leads to a mobility that often depends strongly on both electric field and carrier density. Organic diodes typically operate at an electric field of several times 10^5 V/cm and at carrier densities of up to a few $10^{17}cm^{-3}$ [25]. In contrast, field-effect transistors operate at lateral electric fields of few 10^4V/cm and at carrier densities above $10^{18}cm^{-3}$. For carrier densities below about $10^{17}cm^{-3}$, typical of diode operation, the mobility does not depend strongly on the carrier density[26]. In this low density limit, interactions between carriers and state filling effects are not significant. In contrast, for carrier densities above about 10^{18} cm^{-3}, typical for FET operation, the occupation of lower energy hopping sites enhances the carrier mobility. Because of the random molecular structure and differences in the operating regimes, the transport in these limits can be very different.

Three techniques have been used to determine carrier mobilities in disordered oraganic materials: (i)time-of-flight (TOF) transient current measurement ,(ii) fitting of single-carrier space charge limited (SLC) diode I-V curves and (iii) analysis of field-effect transistor I-V curves. These three mobility measurement techniques sample different electric field and charge density regemes. TOF techniques can measure the carrier mobility for electronic fields up to 10^6V/cm but they are restricted to very low volume averaged carrier densities of about $10^{13}cm^{-3}$ or less. Because the TOF technique is restricted to very low carrier densities, it is difficult to measure the carrier mobility in the presence of extrinsic trap states. Fitting the single carrier SLC diode I-V curve can provide the mobility for electric fields densities from about about 10^5 to 10^6 V/cm and for carrier densities form $10^{16}$to $10^{18}cm^{-3}$. These measurements are much less sensitive to trapping effects than TOF measurements because the comparatively large density of injected carriers can fill moderate densities of traps without significantly perturbing the mobility measurement. In SCL diode measurements, the electric field and carrier density are functions of position within the device structure. Thus, fitting the measured I-V curves requires assumptions about the carrier density and electric field dependence of mobility. Nevertheless, the TOF methhod and the SLC diode method usually yield consistent results for the mobility.

In FET mobility measurements, the lateral electric fields that are responsible for current flow are typically in the 10^4 V/cm range and the charge is confined to a thin region of organic disordered material adjacent to the gate insulator. This leads to very high charge carrier densities of about $10^{19}cm^{-3}$. These carrier densities are high enough to significantly modify the mobility due to changes in the occupation of hopping sites. In addition, the results are sensitive to the local molecular structure near the interface that may differ significantly from that typical of bulk films[27]. The FET mobilities are often significantly larger than TOF and SCL diode results made on the same material. The higher mobility inferred from FET measurements is attributed to either the different carrier density regimes in which the measurements are made, or to variations in the local molecular structure in the two kinds of devices.

2.4.2 Time-of Flight Mobility Measurements

In the Smectic materials which we investigate here, about the carrier density is low, on the order of 10^{10}~10^{12} cm^{-3}. We treated very thin cells in which the sample thickness L is

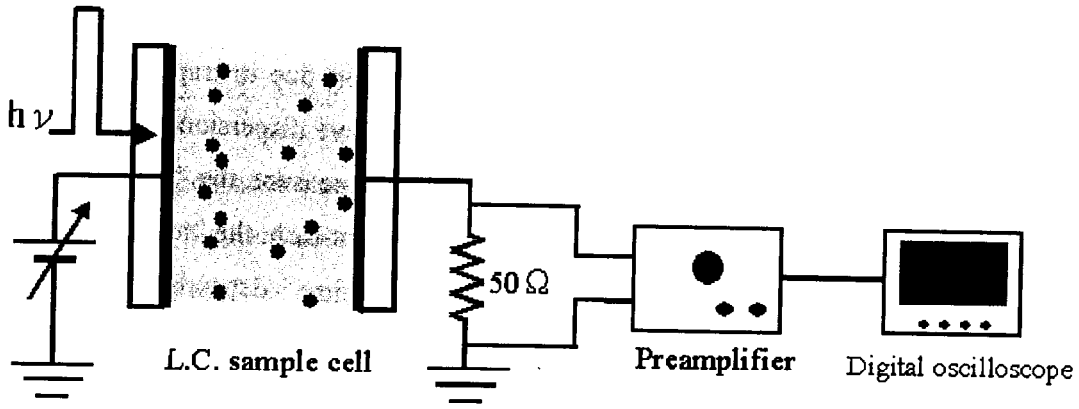

Fig. 2.4 :Time-of-Flight set up

about 5~20μm. In this case, we think the TOF technique is best application, provided that we are careful to reduce the pulsed light intensity in order to prevent space charge effects. The TOF set up is as follows (Fig.2.4). Our SmLC sample is mainly composed of 2-phenyl naphthalene derivatives (6-(4'-octylphenyl)-2-dodecyloxynaphthalene (8-PNP-O12). The LC sample was sandwiched by ITO or Al coated glasses spaced by a silica spacer. An N_2 dye Laser (Laser hotonics LN203C, wavelength =337nm, pulth width =600ps, and power = 40 μJ/pulse) was flushed from the side of +biased electrode for hole transport or – biased electrode for electron transport. The photo-excitation of SmLC by Laser irradiation (λ=320nm) into the main absorption band of the SmLC resulted in the creation of electron-hole pairs in a very thin layer (Light penetration depth less than 1μm) near the illuminated electrode. Depending on the polarity of the applied electric field, one charge carrier is eliminated at the illuminated electrode, while the other one moves through the sample towards the counter electrode. The charge motion creates a displacement current, which is measured by a digital oscilloscope (Nicolet Pro92).

In principle, if the moving charge packet had no dispersion, the current shape would be of a rectangular form. The ideal current signal would then have a "cut off" at the time when the carriers arrive at counter electrode. From the time of "this cut off", i.e, transit time, we can determine the drift velocity, and thus the mobility of the carrier transport. However, in reality, the transit time for different carriers has variation due to trapping and diffusion processes. For this reason, the real photocurrent signals have dispersion. In such a case, the conventional way to determine the transit time is to measure the "kink point" at the transition between the plateau and the tail. This is different from the "true transit time" and the manner in which it deviates from the "true transit time" depends on the underlying processes which contribute to the dispersion. This problem is discussed on Chapter 3. An example of the mobility as determined by the kink poin is shown in Fig.3.2.

2.4 Charge Transport Processes [16,17,28]

2.4.1 Gill's Empirical Law

In this section we will survey the properties of carrier transport in disordered organic materials such as polymers and molecularly doped polymers. In MDPs, isolated dopants exist in polymer host. Charges hop between the dopant molecules in a matrix of host polymer. The first TOF measurements on molecularly doped polymers (MDPs) showed a field-dependent mobility with a Poole-Frenkel field dependence [29,30],

$$\mu \propto \exp(\gamma\sqrt{E}). \tag{2.1}$$

The "Poole-Frenkel factor" γ was found to be a decreasing function of the temperature. A phenomenological description of this dependence was proposed by Gill, who introduced a fitting formula for poly (*N*-vinyl carbazole)-trinitrofluorenone (PVK-TNF) complexes, specifically [30]

$$\mu = \mu_0 \exp\left(-\frac{\Delta_0 - \beta\sqrt{E}}{kT_{eff}}\right), \tag{2.2}$$

where Δ_0 is a low field activation or barrier energy, β a constant, k the Boltzmann constant, T the absolute temperature, and

$$\frac{1}{T_{eff}} = \frac{1}{T} - \frac{1}{T_0}, \tag{2.3}$$

T_0 being the compensation temperature at which, hypothetically, the mobility becomes field-independent. In the Gaussian disorder model explained below, we will see that the microscopic origin of T_0 is attributed to a competition between the energetic disorder and positional or orientational disorder [31].

2.3.2 Scher-Montroll Theory[32]

One of the early problems with analyzing the time of flight experiments was that the mobility could not be directly related to the transit time because the photocurrent transients were highly dispersive. An understanding of dispersion could be had through an analysis of a continuous-time-random-walk (CTRW) model between sites where the carrier is time-

dependently released (waiting time distributions, WTD's). It was expected that disorder should give rise to a broad distribution of WTD's. By introducing a WTD of the form

$$\psi(t) \sim t^{-(1+\alpha)}. \tag{2.4}$$

Scher and Montroll were able to show that the associated current must feature a time dependence of the form

$$I(t) \sim \begin{cases} t^{-(1-\alpha)}, & t \le t_{tr} \\ t^{-(1+\alpha)}, & t \ge t_{tr}. \end{cases} \tag{2.5}$$

α is the dispersion parameter, and t_{tr} the effctive transit time. The CTRW formalism for exponential density of state (DOS) leads to the same behavior as the multiple trapping model [33]. The motion of the independent charge carriers at the edge of the transport state (or valence band) is interrupted by temporally trapping events by localized states. This model is described in detail and discussed to apply to our material in Chapter 3.

2.3.3 Gaussian Disorder Model

Bässler and coworkers extensively studied the Poole-Frenkel type field dependent mobility in disordered organic materials by using Monte Carlo simulation on the basis of a three-dimensional Gaussian disorder model (GDM) [34, 35]. For organic disordered system, where the carrier transport occurs through hopping process, we can reasonably assume that the energy localized state is usually characterized by Gaussian density of states (DOS)

$$\frac{1}{\sqrt{2\pi\sigma^2}} \exp\left[-\frac{\varepsilon^2}{2\sigma^2}\right], \tag{2.6}$$

where σ is the energy deviation of DOS, the energy being measured relative to the center of DOS. The energetic disorder characterized by σ reflects the fluctuation in the polarization energy as well as dipolar interactions in the case of asymmetric molecules or impurity molecules at a low density. A reasonable transition rate for hopping process was suggested by Miller and Abrahams [36]. It is the product of pre-factor ν_0, a carrier wave-function overlap factor, and a Boltzmann factor for jumps upward in energy, i.e. the jump rate between sites i and j, the distance between the sites being r_{ij}, is

$$\nu_{ij} = \nu_0 \exp\left(-\frac{2r_{ij}}{\alpha}\right)\begin{cases}\exp\left[-\dfrac{\varepsilon_j - \varepsilon_i - e\boldsymbol{E}\cdot\boldsymbol{r}_{ij}}{kT}\right] & (\text{for } \varepsilon_j - \varepsilon_i - e\boldsymbol{E}\cdot\boldsymbol{r}_{ij} > 0.)\\ 1 & (\text{for } \varepsilon_j - \varepsilon_i - e\boldsymbol{E}\cdot\boldsymbol{r}_{ij} < 0.)\end{cases} \tag{2.7}$$

Here α is a specific decay length of the wave function in the localized states and k is Boltzmann constant. This formulation assumes an electron-phonon interaction for phonon-assisted thermal activation hopping process neglecting polaronic effects. Using extensively the computer aided random walk of Monte Carlo simulation, they thought that they found the Poole-Frenkel like field dependent mobility were observed in their simulation. But this dependence of simulation appear in much higher field than that of experiment and that region is very narrow. They derived the disorder formalism as

$$\mu_{3D} = \mu_0 \exp\left[-\left(0.67\frac{\sigma}{kT}\right)^2\right]\exp\left\{C\left[\left(\frac{\sigma}{kT}\right)^2 - \Sigma^2\right]\sqrt{E}\right\} \tag{2.8}$$

for $\Sigma \geq 1.5$, by asymptotic fitting to the simulation-result.

Garstein and Conwell [37] showed that a spatial correlation in the site energy distribution for the carriers can explain the experimental field dependent mobility. If there is a spatial correlation of energy between sites, the energy of neighboring sites may become close to one another. In such a case, a charge can easily hop between neighbors. A strong field dependence of the mobility then occurs when the potential difference (eEl) across a relevant length scale l becomes compatible to kT. In the uncorrelated case, $l = a$, a distance which is so small that field dependence only occur in high field region. A spatial correlation introduces a new l, over which the site energies are correlated. The correlation must be occur in order to cause a field dependent mobity in the low field region where it is often observed.

Novikov and Vannikov [38] investigated a plausible mechanism for correlations in the disorder. The showed that the charge-carrier and permanent dipole interaction gives rise to a long-range correlation that falls off algebraically with distance y, as 1/y. A one-dimensional Master equation with nearest neighbor hopping has been exactly solved by

Derrida [39]. In the case of correlated disorder, Dunlap *et al*, [40-42], showed that, in the continuum limit, the result is [40],40,41,42

$$\mu = \frac{\mu_0}{\gamma \int_0^\infty dy e^{-\gamma y} \left\langle e^{-\beta\varepsilon(0)+\beta\varepsilon(y)} \right\rangle}, \tag{2.9}$$

where $\gamma = \beta eE$, E the electric field, $\varepsilon(y)$ is the site energy at position y. μ_0 is the mobility if all site energies were the same. Using a Gaussian approximation to calculate the correlation function and the $(1/y)$ dependence for the correlation function $< \varepsilon(y)\varepsilon(0) >$ given by both the charge dipole interaction gives

$$\mu = \frac{\mu_0 e^{-\beta\sigma^2}}{(2\beta\sigma\sqrt{\beta eEa})K_1(2\beta\sigma\sqrt{\beta eEa})} \tag{2.10}$$

where σ is the standard deviation of the density of site energies, a the lattice constant, and $K_1(z)$ is the first-order modified Bessel function of the third kind. In the charge dipole disorder model the standard deviation of the site energy distribution is

$$\sigma = \sqrt{e^2 P^2 n_0 / 12\pi\varepsilon^2 a}, \tag{2.11}$$

where P is the dipole moment and n_0 is density of dipoles. Using an asymptotic expansion for $K_1(z)$ ($\sim(\pi/2z)^{1/2}\exp(-z)$), the the mobility becomes

$$\mu = \mu_0(E)\exp\left(-\beta^2\sigma^2\right)\exp\left(2\beta\sigma\sqrt{\beta eEa}\right). \tag{2.12}$$

This solution obeys the Poole-Frenkel like form Eq.(2.1). Novikov *et al* [43] have performed simulations on the correlated dipoler-disorder model (CDM) in three dimensions which confirm the findings of the analytic result in one dimension. A parameterization of these simulations over a wide range of parameters has shown that the Poole-Frenkel mobility may be described by the formula

$$\mu = \mu_0 \exp[-A_1\hat{\sigma}^n + A_2(\hat{\sigma}^m - A_3)\sqrt{eaE/\sigma}], \tag{2.13}$$

where A_1, A_2 and A_3 are constants, and n=m=2 in the standard in the standard GDM. The CDM formula provides the first direct method to link the parameters for a microscopic

model for the Poole-Frenkel mobility to the results of experiment. A physical interpretation of the role of correlations is discussed in reference [44],

2.5 Discussion

In the sections above we have overviewed the structure of the Smectic liquid crystal (SmLC), the TOF experimental set up, and disorder formalism as applied to a disordered organic solid. We should now consider what kind of models is applicable to the smectic liquid crystal, how we should interpret the experimental results, and how we can compare the experimental result with the model. First we saw that the molecular alignment in the smectic layer does not have long-range order of translation. The periodical alignment is broken in the short length order of the distance from a few times the inter-molecular distance. For this reason, we think that carrier transport is dominated by hopping transport as it is in the disordered organic materials. The molecules of our material, 8-PNP-O12, almost never have a permanent-dipole, and the observed experimental mobility does not have field dependence for the range of measured field range. It is therefore inappropriate to apply the CDM of charge-dipole interaction. For this reason, we adopt GDM for SmLC in Chapter 6. Before we examine the GDM to SmLC, we should consider the estimation of TOF-application to SmLC. Then we tried to analyze the TOF photocrrent by using phenomenological way, mutiple trapping modele as showed in next chapter.

References

[1] S. Chandrasekhar F.R.S., *LIQUID CRYSTALS*, 2th edition (CAMBRIDGE UNIVERSITY PRESS, 1992)

[2] Ian. W. Hamley, *Introduction to Soft Matter -Polymers, Colloids, Amphiphiles and Liquid Crystals* (John Wilely & Sons, Ltd, 2000)

[3] G. W. Gray and J. W. Goodby, *Smectic Liquid Crystals* (Leonard Hill, Glasgow, 1984)

[4] P. G. de Gennes and J.Prost, *The Physics of Liquid Crystals* (2nd Edition, Oxford University Press, Oxford, 1993)

[5] G. Vertogen, W. H. de Jeu, *Thermotropic Liquid Crystals,Fundamentals* (Springer, Heiderberg, 1988)

[6] M. Funahashi and J. Hanna, Jpn. J. Appl. Phys. **35**, L703 (1996)

[7] D. Adam, F. Closs, T. Frey, D. Funfoff, D. Haarar, H. Ringsdorf, P. Schuhmacher, and K. Siemensmeyer, Phys. Rev. Lett. **70**, 457 (1993)

[8] D. Adam, P.Schumacher, L. Haussling, K. Siemensmeyer, K. H. Etzbach and D. Haarar, H. Ringsdorf, Nature **371**, 141 (1994).

[9] R. J. Bushby, and O. R. Lozman, Curr. Opin. Colloid Interface Sci, **7**, 343 (2002)

[10] G. Lüssem, J.H. Wendorff, Plym. Adv. Technol.**9**, 443 (1998).

[11] A. M. van de Craats, J. Phys Chem. B **102**, 9625 (1998)

[12] M. Funahashi and J. Hanna, Appl. Phys. Lett. **76**, 2574 (2000)

[13] M. Redecker, D. D. C. Bradley, M. Inbasekaran, E. P. Woo, Appl. Phys. Lett. **74**, 1400 (1998)

[14] M. Redecker, D. D. C. Bradley, M. Inbasekaran, E. P. Woo, Appl. Phys. Lett. **73**, 1565 (1998)

[15] S. Chandrasekhar, B. K. Sadashiba, and K. A. Suresh, Pramana **9**, 471 (1977).

[16] P. M. Borsenberger and D. S. Weiss, *Organic Photorecepters for Xerography* (Marcel Dekker, 1998)

[17] C. E. Swenberg and M. Pope, *Electronic Processes of organic Crystals and Polumers*, (Oxford University Press, Oxford, 1999)

[18] I. H. Campbell, D. L. Smith, C. J. Neef, and J. P. Ferraris, Appl. Phys. Lett. **74**, 2809 (1999).

[19] M. Redecker, D.D.C. Bradley, M. Inbasekaran, and E. P. Woo, Appl. Phys. Lett. **73**, 1565 (1998).

[20] G. Horowitz, Adv. mat. **10**, 365 (1998).

[21] L. Torsi, A. Dodabalapur, L. J. Rothberg, A. W. P. Fung, and H. E. Katz, Phys. Rev. B **57**, 2271 (1998).

[22] G. G. Malliiaras., J. R. Salem, P.J. Brock and Scott,Phys. Rev. B **58**, R13411 (1998).

[23] L. Torsi, A. Dodabalapur, L. J. Rothberg, A. W. P. Fung, and H. E. Katz, Phys. Rev. B **57**, 2271 (1998).

[24] D. Chen., M. J. Winokur, M. A. Masse, and F. E. Kartasz, Phys. Rev. B **41**, 6759 (1990).

[25] B. K. Cornel, I. H. Campbell. P.S. Davids, D. L. Smith, C. J. Neef, and J. P. Ferraris, J. Appl. Phys. **86**, 5767 (1999).

[26] Z. G. Yu, D. L. Smith, A. Saxena, R. L. Martin, and A. R. Bishop, Phys. Rev. Lett. **84**, 721 (2000).

[27] D.D.C. Bradly, M. Grell, A. Grice, A. R. Tajbakhsh, D. F. Obrien, and A. Bleyer, Opt. Mat. **9**, 1 (1998).

[28] I. H. Campbell and D. Smith, Sol. Stat. Phys. **55**, 1 (2001).

[29] D. M. Pai, J. Chem. Phys. **52**, 2285 (1970).

[30] W. D. Gill, J. Appl. Phys. **43**, 5033 (1972).

[31] Z. G. Soos, S. Bao, J. M. Sin, and G. W. Hayden, Chem. Phys. Lett **24**, 631 (2000).

[32] H. Scher, and E. W. Montroll, Phys. Rev. B **12**, 2455 (1975).

[33] M. Pollak, Philos. Mag. **36**, 1157 (1977).

[34] H. Bassler, Phys. Stat. Sol (b) **175**, 15 (1993).

[35] D. Hertel,H. Bassler, U. Scherf, and H. H. Horhold, J. Chem. Phys. **110**, 9214 (1999).

[36] A. Miller and E. Abrahams, Phys. Rev. **120**, 745 (1960).

[37] Y. N. Gartstein, Chem. Phys. Lett. **217**, 41 (1995).

[38] S. V . Novikov and A. V. Vannikov, Chem. Phys. ???? (1995)

[39] B. Derrida, J. Stat. Phys. 31, 433 (1982).

[40] D. H. Dunlap, P. E. Parris, and V. M. Kenkre, Phys. Rev. Lett **77**, 542 (1996).

[41] P. E. Parris, M. Kus, D. H. Dunlap, and V. M. Kenkre, Phys. Rev. E **56**, 5295 (1997).

[42] V. M. Kenkre, M. Kus, D. H. Dunlap, P. E. Parris, Phys. Rev. E **58**, 99 (1998).B.

[43] S. V. Novikov, D. H. Dunlap, V. M. Kenkre, P. E. Parris, and A.V. Vannikov Phys. Rev. Lett **81**, 4472 (1998).

[44] D. H. Dunlap, P. E. Parris, and V. M. Kenkre, J Imag. Sci. Tech. (1999).

Chapter 3

Macroscopic Analysis Using Multiple-Trapping Model and TOF Technique

3.1 Introduction

In recent years, time of flight (TOF) measurements have been employed for studying electron and hole transport in discotic (DLCs) [1-8] and smectic (SmLCs) [9-15] liquid crystals. As we have discussed in Chapter 2, the TOF technique is used to obtain photocurrent transients from which time of flight is determined as it would be for conventional disordered organic materials [16-18]. The behavior of the mobility for liquid crystals, however, differs from that for disordered organic materials. The charge carrier mobility in liquid crystals exhibits only a week dependence on both the electric field and the temperature, although for some cases a strong field and temperature dependence for a wide range of field and temperature has been observed [3,19,20]. In contrast, the mobility in disordered organic materials noramlly has a strong temperature and electric field dependence. The shape of the photocurrlent transient in SmLC is also less dispersive as compared with that which is normally observed in highly disordered materials [16,17,18]. The TOF current in SmLC might even be called "nondispersive" were it not for the fact that it tends to have an unusually long tail which vanishes very slowly.

Although the charge transport properties of liquid crystals are somewhat different from what is found in conventional disordered organic systems, we suggest that they can be

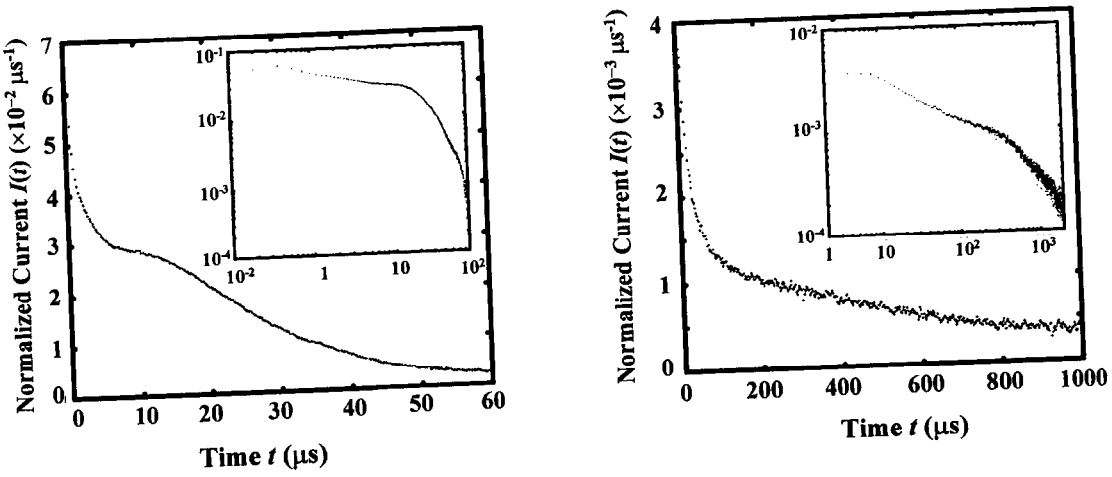

Fig. 3.1: Typical transient photocurrent in SmB phase of 8-PNP-O12 (a) at E=2 10^4 V/cm and (b) at E=10^3 V/cm. Insets are on double log scale.

explained by the same disorder formalism, beginning with the assumption of the Miller-Abrahams type hopping rates which have been discussed in Chapter 2.

In the TOF method, a thin-film sample sandwiched between two electrodes and subjected to an applied field is illuminated with pulsed-laser flash producing a thin-sheet like-shaped carrier distribution near one electrode. The current is then monitored as a function of time. The observed photocurrent transients have an initial spike, a plateau, and a long tail (see Fig. 3.1). Normally the transit time t_a is measured from the intersection of two asymptotes, one to the plateau and the other to the trailing edge of the transient photocurrent [21]. Because the carrier distribution spreads with time as it moves across the film, charges arrive at a variety of different times, and consequently the photocurrent transient does not have a purely rectangular-current shape. Since the drift velocity $v = L / t_a$ is the sample thickness divided by the transit time, the mobility of the charge carriers, μ_a, can be calculated from t_a according to

$$\mu_a = \frac{L^2}{Vt_a}, \tag{3.1}$$

where L is the sample thickness and V the applied voltage. Figure 3.1 shows the typical transient photocurrent signal in the smectic liquid crystal (a) for high-applied field

(10^4V/cm), and (b) for low-applied field (~10^3V/cm). In most organic disordered materials, the TOF current signal can not be measured at such low-applied field on the order ~10^3V/cm. In liquid crystals, on the other hand, a relatively sharp photocurrent signal can even be measured at low-applied fields. Figure 3.2 shows the field dependence of the mobility which is obtained from t_a by using Eq. (3.1).

In order to understand the nature of the charge transport in bulk samples, we want to measure the "mean mobility" μ_m rather than μ_a. If we want to find μ_m by using Eq. (3.1), we must measure a "real" transit time t_{tr} (not t_a) which is defined as,

$$t_{tr} = \frac{L}{<v>}, \tag{3.2}$$

where $<v>$ is the average drift velocity. If the carrier distribution were to remain narrow, there would be no distinction between these two, for in such a case the current time curve would have a rectangular shape, and two transit times $t_a = t_{tr}$ *are the same.* The difficulty arises because the current-time curve is broadened from the ideal rectangular shape by dispersion of the carrier distribution. We consider here three sources for dispersion. First, diffusion brings about a broadening of the transient when the applied field E is low (or the sample is thin) so that after a time t_a the rms of the charge distribution, $\sqrt{2Dt_{tr}}$, is

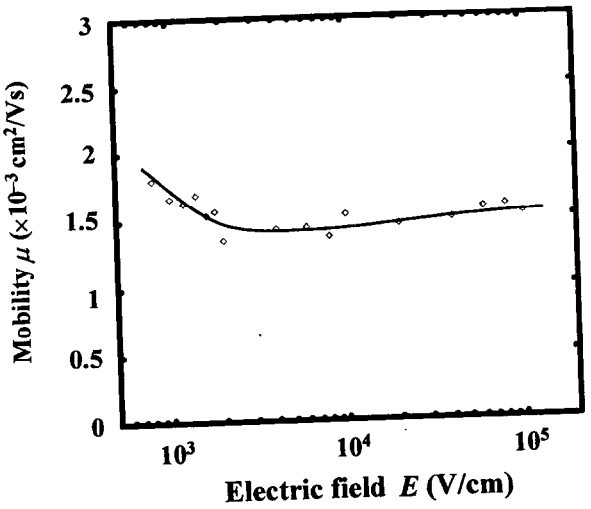

Fig. 3.2 :Field dependence of the mobility in SmB pahse of 8-PNP-O12 derived from conventional method.

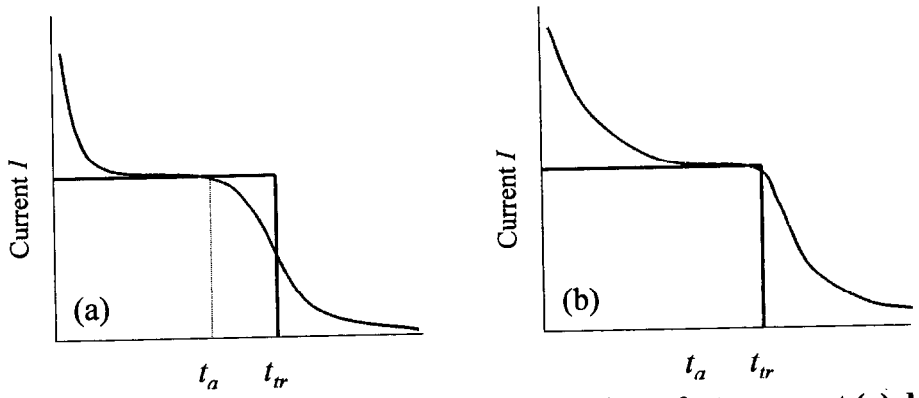

Fig. 3.3: Schematic image of dispersion of transient photocurremt (a) due to diffusion and (b) due to delay of charge transport caused by trapping and de-trapping process.

comparable or greater than its displacement vt_{tr} due to drift. Since $L = vt_{tr}$ and $D = kTv/eE$, if the Einstein relation holds, we can express this criteria,

$$\sqrt{\frac{2kT}{eV}} \geq 1, \tag{3.3}$$

in terms of the ratio of the thermal energy kT to the voltage $V = eEL$. Thus, for $kT = 30.4$ meV which corresponds to 80°C in SmB phase of 8-PNP-O12, diffusion should have a small effect for E larger than 10^3 V/cm. The second source of broadening may be caused by slow equilibration in the transport manifold due to extensive spatial and energetic disorder. The third source is the delay of charge transport caused by trapping and de-trapping process, with the trap-site energy, which is lower than the transport-state energy and distributed more or less at random in the bulk film.

In the transient current, the first and second sources tend to increase the transit time t_{tr} (Fig. 3.3-(a)), which causes the measured kink time t_a to become smaller than t_{tr}. The third source causes a delay of the drifting charge, because the kink point is not particularly sensitive to the effect of deep trapping, t_a is almost the same as t_{tr}. Understanding of the distinction between t_a and t_{tr} in disordered organic materials has been carefully studied for a long time [22-30]. Until now, only the conventional measurement of t_a had been determined in experiments on SmLC, under the expectation that the dynamics of the carrier distribution in SmLC should be almost the same as that found in disordered organic

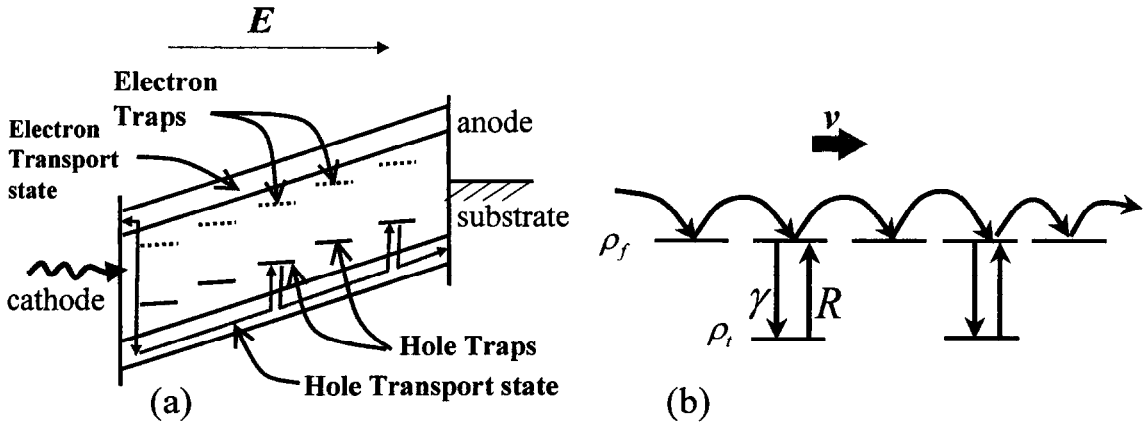

Fig. 3.4 :Scheme of single trapping model (a) denoting energetic level and (b) denoting in the view of transport level

materials. Here, we try to go further and examine the TOF photocurrent based on a combination of the diffusion equation and the multiple-trapping model (MTM) suggested by Noolandi [23,24]. We found there that the carrier transport in our materials can be explained by MTM with diffusion under the assumption of a Gaussian distribution of traps. Furthermore, in the low field region, the carrier transport properties are consistent with Einstein relation. The Einstein relation has never been directly observed in organic disordered solids.

3.2 Multiple-Trapping Model without Diffusion

3.2.1 Generalized MTM with $D = 0$

In this section we discuss the applicability of the well-known multiple-trapping model , a two state heuristic model which assumes that charges are free to drift in a transport manifold under the action of an applied field, but occasionally become localized in randomly placed traps. It is simplest form, the effects of diffusion in the transport manifold are considered to be unimportant as compared to the dispersion caused by trapping and

release events We will show that this simple model is not applicable to the SmLC material, and that the inclusion of both effects, trapping and diffusion, is required to provide an adequate description of the photocurrent transients.

This MTM is discussed in detail in Refs [23,26]. It is a heuristic representation of the real trapping process that go on in the sense that the importance of the spatial location of the individual traps is neglected. Instead, trapping events are simply described by two rates, a trapping rate γ and release rate R. The term "trap state" is used for any localized states in which a carrier cannot move for some time. In contrast, the term "transport state" is used for any fundamental state which define the microscopic mobility, μ_m, of a charge carrier. We assume that the density of traps is small enough so that the traps are spatially isolated from each other, so that direct transitions between them are negligible. Transport states, on the other hand, are spatially interconnected so as to allow transport with an observable drift speed. Thus the microscopic mobility is determined by transitions between transport states, whereas γ and R determine the transitions between transport states and traps. A schematic description of the model is shown in Fig. 3.3. Consider, for example, the case of positive charge (hole) transport. Let us assume that the distribution of holes is generated in immediate vicinity of the illuminated electrode (cathode), and denote the location of the charge packet to be $x = 0$ at time $t = 0$. The holes subsequently drift (under the applied field E) toward the anode located at x = L (sample length). The transitions that take place in the MTM are described by two coupled master equations,

$$\frac{\partial \rho_h(x,t)}{\partial t} = -v_h \frac{\partial \rho_h(x,t)}{\partial x} - \gamma \rho_h(x,t) + R\rho_t(x,t) + \delta(x)\delta(t), \tag{3.4}$$

$$\frac{\partial \rho_t(x,t)}{\partial t} = \gamma \rho_h(x,t) - R\rho_t(x,t), \tag{3.5}$$

where $\rho_h(x,t)$ and $\rho_t(x,t)$ are locally-normalized population of the transport state and trap state, respectively. In equations (3.4) and (3.5) we have only included one variety of trap state. If the system has n species of traps, each having a different trapping rate γ_i and release rate R_i (i = 1~ n), the model can be expressed by n+1 equations as

$$\frac{\partial \rho_h(x,t)}{\partial t} = -v_h \frac{\partial \rho_h(x,t)}{\partial x} - \sum_i \gamma_i \rho_h(x,t) + \sum_i R_i \rho_{ti}(x,t) + \delta(x)\delta(t) \tag{3.6}$$

$$\frac{\partial \rho_{ti}(x,t)}{\partial t} = \gamma_i \rho_h(x,t) - R\rho_{ti}(x,t), \tag{3.7}$$

where i is the label for each traps, i-th localized state. Here we define the total trapping rate as $\gamma = \sum_i \gamma_i$. The contribution of γ for each i th trap depends on distribution of traps, so,

$$\gamma_i = \gamma W_i, \tag{3.8}$$

where W_i denotes the weight for i th trap distribution normalized as $\sum_i W_i = 1$. The equations (3.6) and (3.7) can be solved using Laplace transforms. The Laplace transform of $\rho_h(x,t)$ and $\rho_{ti}(x,t)$ are defined as

$$\tilde{\rho}_h(x,s) = \int_0^\infty dt \rho_h(x,t) e^{-st} \tag{3.9}$$

$$\tilde{\rho}_{ti}(x,s) = \int_0^\infty dt \rho_{ti}(x,t) e^{-st} \tag{3.10}$$

Then the Eqs. (3.6) and (3.7) are transformed in the Laplace domain as

$$s\tilde{\rho}_h(x,s) = -v_h \frac{\partial \tilde{\rho}_h(x,t)}{\partial x} - \gamma \tilde{\rho}_h(x,s) + \sum_i R_i \tilde{\rho}_{ti}(x,s) + \delta(x) \tag{3.11}$$

$$s\tilde{\rho}_{ti}(x,s) = \gamma_i \tilde{\rho}_h(x,s) - R\tilde{\rho}_{ti}(x,s). \tag{3.12}$$

Substituting the solution for $\tilde{\rho}_{ti}(x,s)$ from Eq. (3.12) into Eq. (3.11), we find a closed equation for $\rho_h(x,t)$;

$$s\tilde{\rho}_h(x,s) = -v_h \frac{\partial \tilde{\rho}_h(x,t)}{\partial x} - \gamma \tilde{\rho}_h(x,s) + \gamma \sum_i \frac{R_i W_i}{s + R_i} \tilde{\rho}_h(x,s) + \delta(x). \tag{3.13}$$

Equation (3.13) is easily integrated. By imposing the normalization condition that the total charge is 1, we find that gives

$$\tilde{\rho}_h(x,s) = \frac{1}{v} \exp\left(-\frac{A(s)x}{L}\right), \tag{3.14}$$

and

$$\tilde{\rho}_i(x,s) = \frac{\gamma_i}{v(s+R_i)} \exp\left(-\frac{A(s)x}{L}\right), \tag{3.15}$$

where the function:

$$A(s)=\frac{L\gamma\, s}{v}\tau(s), \tag{3.16}$$

depends on the trapping time

$$\tau(s)=\frac{1}{\gamma}+\frac{1}{s+R} \qquad \text{for one trap,} \tag{3.17}$$

$$=\frac{1}{\gamma}+\frac{1-\tilde{\psi}(s)}{s} \qquad \text{for multiple traps.} \tag{3.18}$$

In equation (3.18) we have introduced the average trap dwell time distribution function,

$$\tilde{\psi}(s)=\sum_i \frac{R_i W_i}{s+R_i}. \tag{3.19}$$

Writing the trap state distribution as a function of ε measured from transport state, the summation in (3.19) may be replaced to the integral, i.e.,

$$\tilde{\psi}=\int_{-\infty}^{\infty} d\varepsilon\, \rho(\varepsilon)\frac{R(\varepsilon)}{s+R(\varepsilon)}, \tag{3.20}$$

where $\rho(\varepsilon)$ is distribution of trap energies. Combining (3.14) and (3.15), the total carrier distribution in the Laplace domain is given by

$$\tilde{\rho}(x,s)=\tilde{\rho}_h(x,s)+\sum_i \tilde{\rho}_{ti}(x,s)=\frac{A(s)}{sL}\exp\left(-\frac{A(s)x}{L}\right). \tag{3.21}$$

It can be shown that the normalized photocurrent $I(t)/\tilde{I}(0)$, which is the current divided by total charge $Q=\tilde{I}(0)$, is given by

$$\frac{I(t)}{\tilde{I}(0)}=\frac{1}{L}\frac{d}{dt}\left[\int_0^t dx x\rho(x,t)+L\int_t^{\infty} dx\rho(x,t)\right]. \tag{3.22}$$

The first term is the expectation value of the location of carrier in the bulk. Then the derivative of time becomes drift velocity. The reason why we need the second term is as follows. The holes that arrive at the anode cannot move, because they strongly recombine with the electrons at the anode. Substituting Eq. (3.21) into Eq. (3.22), we find that the Laplace transformed normalized current of Eq. (3.22) is given by

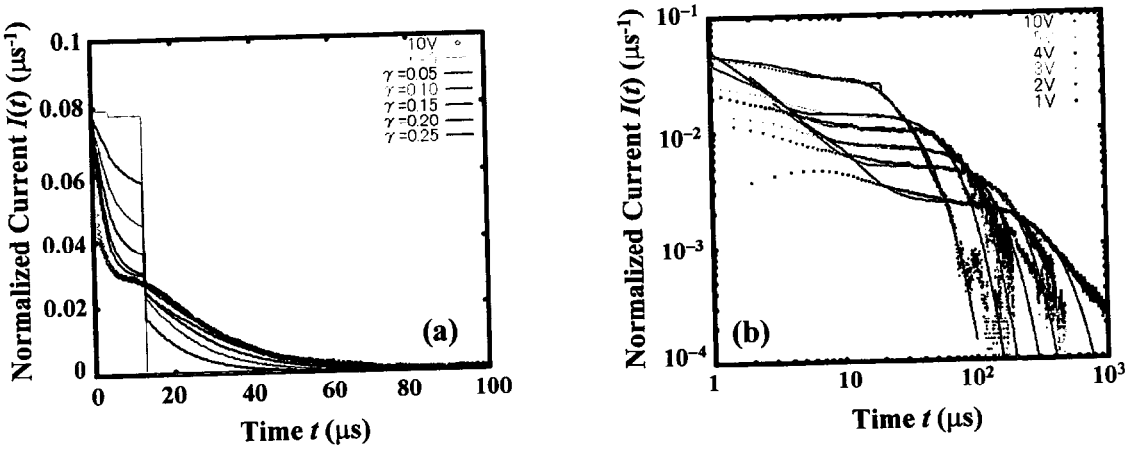

Fig. 3.5 :One trapping model comparing with experimantal photocurrent (a) various trapping rate. The Points are experimental result in SmB of 8-PNPO-12 for V=10V. (b)Fitting of the model for each Voltage

$$\frac{\tilde{I}(t)}{\tilde{I}(0)} = s\int_0^L dx x\tilde{\rho}(x,s) + sL\int_L^\infty dx\tilde{\rho}(x.s)$$

$$= \frac{1}{A(s)}(1-e^{-A(s)}). \qquad (3.23)$$

The photocurrents can be obtained from Eq. (3.23) by using a numerical inverse Laplace transform. In this manner, we can handily produce current-time curves for any trap distribution. There are several ways to implement these types of calcuations [24].Figure 3.4-(a) shows the derived photocurrent as obtained from the inverse Laplace transform of Eq. (3.23) for the one-trap model described by Eq. (3.17). Although we have implemented a numerical procedure, we should point out that the photocurrent of one-trap model can be obtained analytically as described in Ref [24,25].

Figure3.4-(a) shows the photocurrent traces, parametric in trapping rate γ. The sample length $L = 5\mu$ m, drift velocity $v = 40$ cm/s and release rate $R = 0.12\mu s^{-1}$. In this case, thus, the transit time $t_{tr} = L/v = 12.5$ μs. $1/\gamma$ is the average lifetime of a free carrier. If the $1/\gamma > t_{tr}$, a trapping event is not important for dispersion of the current, because most of the carriers will not be trapped before the transit time. In such a case the shape of photocurrent will be close to rectangular (See the current for $\gamma = 0$ and 0.05 μs^{-1}; $1/\gamma = \infty$ and 20μs in Fig 3.4-

(a)). As γ becomes large, trapping events occur more frequently, causing a dispersion of the transient. As long as there is a reasonable probability that a carrier may not be trapped, a sharp kink point may still be observed. This sharp kink point becomes smaller as γ increases further. For comparison, we have plotted the experimental data. We note that when $\gamma = 0.25\ \mu s^{-1}$, the shape of the derived photocurrent from the model is close to the results found in experiment. We fitted one trapping model to the experimental data by using the method of least squares. A total of 30 sampling points in the experimental data in the neighborhood around the kink point were used. The best fits are reasonable in the neighborhood of the kink point, but it is difficult to fit the tail for long times. This suggests that one trapping model can not explain the features of charge transport delay observed in the experiment. Another indication of this failure is that the model predicts that the derived parameters (γ and R) must be independent of field. Unfortunately, the fitting parameters change systematically with field, as shown in Table 3.1. In Fig. 3.5, we fixed parameters γ=0.126 μs^{-1} and R = 0.44μs^{-1}, and we examined the dependence of the photo transient on remaining parameter v. The fixed parameters were chosen to be a best fit for experimental photocurrent at V = 3V. In the current of one-trapping model, most carriers are trapped but can be released (1/R = 22 μs). This cannot lead to a sufficient dispersion of the current. In high-field region, carriers can drift without being trapped (1/γ =7.9μs). The carriers, which are not trapped, produce a sharp kink point which could not be observed, however, in our materials in high-field range (10^3~5×10^5 V/cm). If we extend the analysis to include two traps, or three traps, the fitting improves. However, we find an inconsistency in that the the trap parameters must change systematically with field in order to fit the data.

Thus, we think that trapping alone is insufficient to describe what is happening in our

TABLE 3.1 Derived parameters by fitting of one-trapping model

V (V)	10V	5V	4V	3V	2V	1V
v (cm/s)	39	26	17	14	6.5	5.2
γ (μs^{-1})	0.28	0.22	0.18	0.13	0.11	0.082
R (μs^{-1})	0.15	0.12	0.12	0.044	0.053	0.0395

materials.

3.2.2 Diffusion equation

Diffusion can also be considered as one of the sources of the current dispersion. For an initially photo-generated delta-function like charge distribution inside the sample, at x=a, the diffusion equation is expressed as

$$\frac{\partial \rho_h(x,t)}{\partial t} = -v_h \frac{\partial \rho_h(x,t)}{\partial x} + D\frac{\partial^2 \rho_h(x,t)}{\partial x^2} + \delta(x-a)\delta(t), \tag{3.24}$$

where D is diffusion constant. To describe charge which is injected at the anode, at x=0, the limit $a \to +0$ will be taken. Equation (3.24) is transformed in Laplace domain as

$$s\tilde{\rho}_h(x,s) = -v_h \frac{\partial \tilde{\rho}_h(x,s)}{\partial x} + D\frac{\partial^2 \tilde{\rho}_h(x,s)}{\partial x^2} + \delta(x-a). \tag{3.25}$$

Then, using a Fourier transformation over space, the general solution can be derived as

$$\tilde{\rho}_h(x,s) = \begin{cases} C_1 e^{(1+\kappa)vx/2D} + C_2 e^{(1-\kappa)vx/2D} + \dfrac{1}{\kappa v} e^{(1-\kappa)(x-a)/2D} & \text{for } x \geq a, \\ C_1 e^{(1+\kappa)vx/2D} + C_2 e^{(1-\kappa)vx/2D} + \dfrac{1}{\kappa v} e^{(1+\kappa)(x-a)/2D} & \text{for } x \leq a, \end{cases} \tag{3.26}$$

where

$$\kappa = \sqrt{1+4Ds/v^2}\,. \tag{3.27}$$

We take the boundary conditions as reflection at the anode (carrier injection) and absorption at the cathode , i.e.,

$$J(x=0) = v\rho_h(x,t) - D\left.\frac{\partial \rho_h(x,t)}{\partial x}\right|_{x=0} = 0 \qquad \text{at anode,} \tag{3.28}$$

$$\tilde{\rho}_h(x=L) = 0 \qquad \text{at cathode.} \tag{3.29}$$

By using condition Eq. (3.28) applying to Eq. (3.26) for $x \leq a$ and condition Eq. (3.29) applying to Eq.(3.26) for $x \geq a$, the constants C_1 and C_2 may be determined;

$$C_1 = -\frac{2e^{-\kappa vL/2D}}{\kappa+1+(\kappa-1)e^{-\kappa vL/D}}; \tag{3.30}$$

$$C_2 = \frac{(\kappa-1)(1-e^{-\kappa vL/D})}{\kappa\left[\kappa+1+(\kappa-1)e^{-\kappa vL/D}\right]}. \tag{3.31}$$

If we decide

$$C_1' = -\frac{2e^{vL/2D}}{\kappa+1+(\kappa-1)e^{-\kappa vL/D}}, \tag{3.32}$$

expression for the Laplace transform of the current may be written as follows:

$$\frac{\tilde{I}(s)}{\tilde{I}(0)} = \frac{D}{vL}\left(C_1' e^{-(1+\kappa)vd/2D} + C_2 + \frac{1}{\kappa}\right) + \frac{2DC_1'}{vL(1+\kappa)}\left(1-e^{-(1+\kappa)vd/2D}\right) + \frac{2D(C_2+\kappa^{-1})}{vL(1-\kappa)}\left(1-e^{(1-\kappa)vd/2D}\right). \tag{5.36}$$

The photocurrent can be obtained by a numerical inverse Laplace transform of (5.36), as described in Fig.3.6. The carrier distribution for various times for a sample length L= 10 μm is also shown in Fig. 3.7. (In the figure, x = 0 is the position of cathode and x = 10μm is the position of anode.). The experimental results were fitted numerically as shown in Fig. 3.10. From this figure, we can see that the measured transit time t_a is the time when the

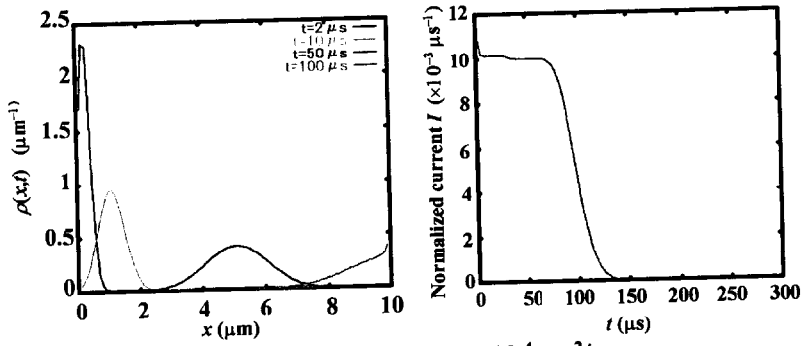

(a) $v = 10$ cm/s, $D = 10^{-4}$ cm^2/s

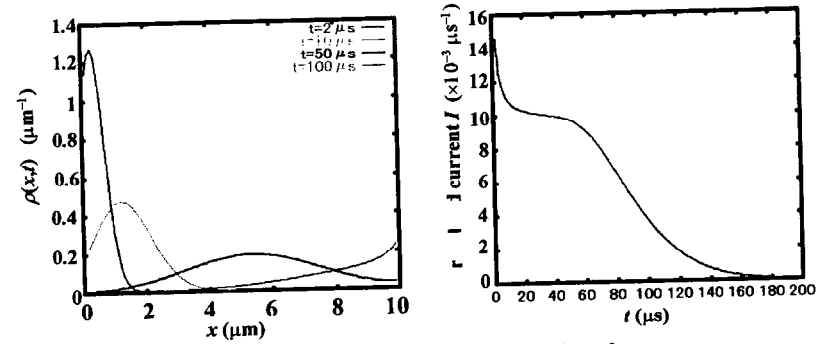

(b) $v = 10$ cm/s, $D = 5 \times 10^{-4}$ cm^2/s

Fig. 3.6 :Diffusion model : Carrier distribution traces in parametric time (left side) and corresponding transient current

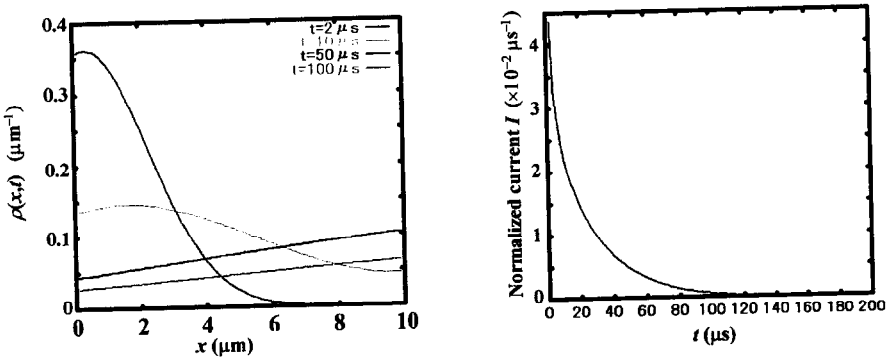

(c) $v = 10$ cm/s, $D = 5\times10^{-2}$ cm^2/s

Fig 3.7 :Diffusion model: Carrier distribution traces in parametric time (left side) and corresponding transient current

carrier distribution begins to arrive at the anode, and t_{tr} is the time at which the center of the carrier distribution to arrives at the anode. These features have been studied

in detail by Hirao *et al* [29,30]. Figure 3.9 shows the current and corresponding carrier distribution for each D values. In this case, diffusion dispersion is very large as diffusion motion is faster than drift motion ($\sqrt{<x^2>} = \sqrt{2Dt_{tr}} = 14\mu m > L$). If diffusion is independent of field, t_a will be found to be field independent, and the mobility will appear to decrease with increasing field. On the other hand, if the sample length is large enough, so that $\sqrt{<x^2>} \sim \sqrt{t}$, the drift ($x \sim t$) is more important than diffusion , and the mobility will appear to be a constant. In a dispersive transient, the conventional t_a can be measured easily plotting the transient on a double log scale, as shown in Fig. 3.10. The condition under which this dispersive current

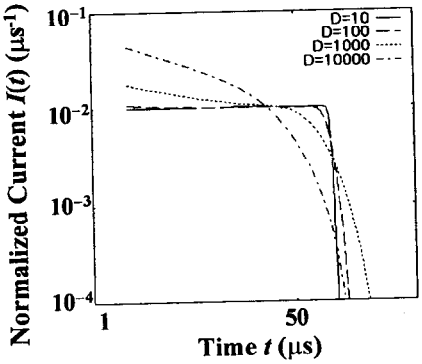

Fig. 3.9 :Double log scale of diffusion model for each diffsion constants

behavior occurs, denoted in Eq.(3.3). We may conclude that the filed dependent mobility can be observed in Fig. 3.2 for low field region.

Fitting the data with the diffusion model was carried out using the method of least squares. We fit to a reduced data set consisting of 30 points per transient. The quality of the fits is quite good, as shown in Fig. 3.10. There are only two fit parameters, the mobility μ (which is calculated by v/E) and the diffusion constant D. In order to maintain good fits for all the data, these values must change with field, is shown in Fig.3.11. When we look at fitting photocurrent in detail, we find that w fail to fit the long-time tail (see double log plot in inset of the figure). This means that features of dispersion are are not due to diffusion alone. Furthermore, the derived parameters in Fig. 3.11 show a strong field dependence.

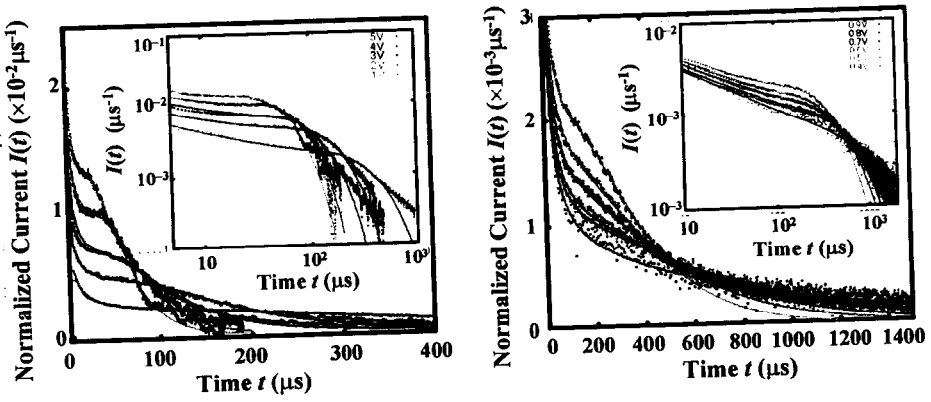

Fig.3.10 Fitting the diffusion model to experimental data

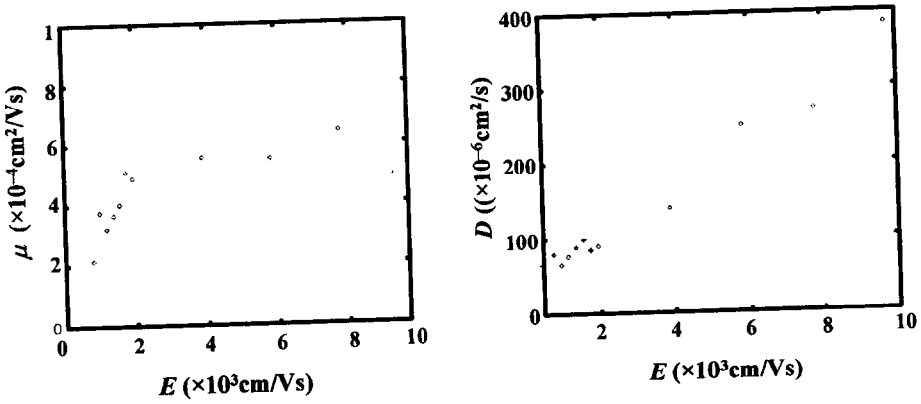

Fig. 3.11 :Field dependence of derived parameter μ,D form diffusion model

This field dependence seems to change in low field (< 2×10^3 V/cm) range for which the mobility dependence measured by conventional method is shown in Fig. 3.2. If the model is appropriate, such a change of the intrinsic parameters with field must not occur. Thus we may conclude that convection and diffusion alone cannot explain transport in SmLC.

3.3 Multiple-Trapping Model with Diffusion

3.3.1 Formulation

In a previous section we showed that neither the simple MTM nor the diffusion model alone can explain the behavior of experimental photocurrents. It is natural to ask, therefore, if a combination of trapping and diffusion will provide a suitable description of transport in SmLC. We suggest that the dispersion is dominated by diffusion in low field region (~10^3 V/cm), and that diffusion is as important as the trapping in the low and middle-field regions (~10^4 V/cm). The higher-field region (10^4 ~10^5 V/cm) will be discussed in Chapter 6.

To modify the multiple trapping model to include diffusion, we simply add a diffusion term to the equations of transport state;

$$\frac{\partial \rho_h(x,t)}{\partial t} = -v_h \frac{\partial \rho_h(x,t)}{\partial x} + D\frac{\partial^2 \rho_h(x,t)}{\partial x^2} - \sum_i \gamma_i \rho_h(x,t) + \sum_i R_i \rho_{ti}(x,t) + \delta(x-a)\delta(t) \tag{3.37}$$

$$\frac{\partial \rho_{ti}(x,t)}{\partial t} = \gamma_i \rho_h(x,t) - R_i \rho_{ti}(x,t)\,. \tag{3.38}$$

After Lapace transformation of Eqs. (3.37) and (3.38) and setting $\tilde{\rho}_{ti}(x,s)$ to zero, we find that

$$s\tilde{\rho}_h(x,s) = -v_h \frac{\partial \tilde{\rho}_h(x,t)}{\partial x} + D\frac{\partial^2 \tilde{\rho}_h(x,t)}{\partial x^2} - \gamma\tilde{\rho}_h(x,s) + \gamma\sum_i \frac{R_i W_i}{s+R_i}\tilde{\rho}_h(x,s) + \delta(x-a)\,. \tag{3.39}$$

By combining Eqs. (3.16) ~(3.19), equation (3.39) may be written as

$$\frac{Av}{L}\tilde{\rho}_h(x,s) = -v_h \frac{\partial \tilde{\rho}_h(x,t)}{\partial x} + D\frac{\partial^2 \tilde{\rho}_h(x,t)}{\partial x^2} + \delta(x-a) \tag{3.40}$$

By comparing Eq. (3.40) with Eq. (3.25), and considering the same boundary conditions as used in the diffusion model, the solutions are formally the same as in the diffusion model, i.e., Eq. (3.26) and Eqs. (3.30)~(3.36) except for the definition of κ; instead of Eq. (3.27), we have

$$\kappa = \sqrt{1+4DA/vL}\ . \tag{3.41}$$

3.3.2 One or Two trapping

Figure 3.11 shows the results of fitting by a two-trap model with diffusion. We fitted the experimental data for V=5V with the six parameters; v, D, γ_1, γ_2, R_1 and R_2.. After fitting the 5V data, the trapping parameters, γ_1, γ_2, R_1 and R_2, were fixed. We then fitted the data for the other voltages,1~4 V, adjusting only two parameters, v and D . The fits in the tail region have improved.. With decreasing field, however, the fits are not as good as they were for the fits of the convection-diffusion equation alone, with no traps. . Apparently the trapping parameters must also be allowed to change with field in order to fit a wide range of voltages with the two-trap model..

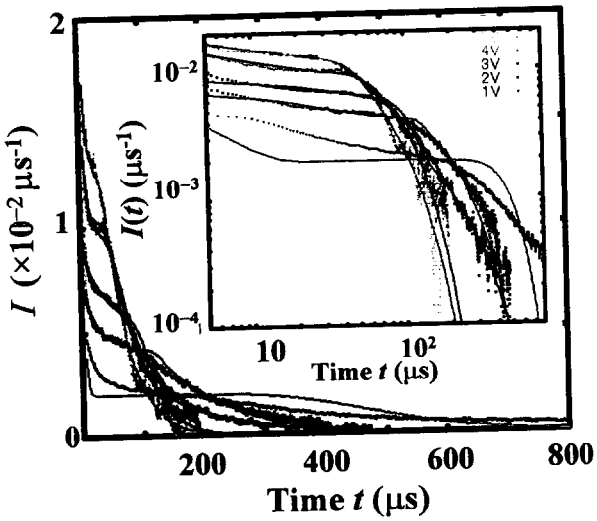

Fig. 3.11 :Fitting by using two trapping model with diffusion

3.3.3 Exponential distribution of traps

As a few- (one- or two-) trap model could not explain the field dependence over a wide range, we considered the MTM with a continuous distribution of traps. We examed two cases: (i) an exponential distribution of traps, and (ii) a Gaussian distribution of traps. Let us first discuss the exponential distribution. We can reasonably assume that trapped carrier will be released by by a thermally activated rate, i.e.

$$R(\varepsilon) = \nu_0 \exp\left(-\frac{\varepsilon}{kT}\right), \tag{3.41}$$

where the energy ε is the trap depth and ν_0 is attempt frequency. An exponential trap distribution can be described as

$$\rho(\varepsilon) = \eta \exp(-\eta\varepsilon). \tag{3.42}$$

After subsituting Eqs. (3.41) and (3.42), Eq. (3.20) becomes

$$\tilde{\psi}(s) = \int_0^\infty d\varepsilon \eta e^{-\eta\varepsilon} \frac{\nu_0 e^{-\beta\varepsilon}}{s + \nu_0 e^{-\beta\varepsilon}}. \tag{3.43}$$

Using the normalization $\int_0^\infty d\varepsilon \eta e^{-\eta\varepsilon} = 1$,

it follows that

$$1 - \tilde{\psi}(s) = \int_0^\infty d\varepsilon \eta e^{-\eta\varepsilon}\left(1 - \frac{\nu_0 e^{-\beta\varepsilon}}{s + \nu_0 e^{-\beta\varepsilon}}\right) = \frac{s\eta}{\nu_0}\int_0^\infty d\varepsilon \frac{e^{-\eta\varepsilon}}{s/\nu_0 + e^{-\beta\varepsilon}}, \tag{3.43}$$

where $\beta = 1/kT$.

Substituting $z = \exp(-\beta\varepsilon)$, and $\alpha = \eta/\beta$ (<1 for convergence of integration), expression (3.43) takes the form,

$$1 - \tilde{\psi}(s) = \frac{s\eta}{\nu_0}\int_0^1 \frac{dz}{\beta z} \frac{z^{\eta/\beta}}{s/\nu_0 + z} = \frac{s\alpha}{\nu_0}\int_0^1 dz \frac{z^{\alpha-1}}{s/\nu_0 + z}$$

$$= \frac{s\alpha}{\nu_0}\left[\int_0^\infty dz \frac{z^{\alpha-1}}{s/\nu_0 + z} - \int_1^\infty dz \frac{z^{\alpha-1}}{s/\nu_0 + z}\right]. \tag{3.44}$$

Extending the integral over a contour in the complex z plane, the principal value of the first integral in (3.44) is

$$\int_0^\infty dz \frac{z^{\alpha-1}}{s/\nu_0 + z} = \frac{\pi(s/\alpha)^{\alpha-1}}{\sin(\pi\alpha)}. \tag{3.45}$$

This same integral is discussed in more detail in Chapter 5. The second integration in (3.44) can be performed for small s << ν_0 ,i.e.,

$$\int_0^\infty dz \frac{z^{\alpha-1}}{s/\nu_0 + z} \xrightarrow{s\to 0} \int_0^\infty dz z^{\alpha-2} = -\frac{1}{\alpha - 1}. \tag{3.46}$$

It follows that asymptotically,

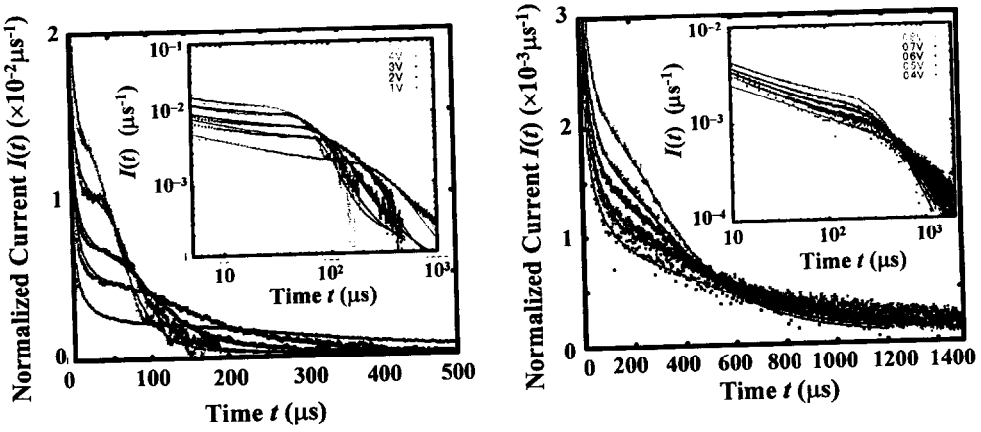

Fig.3.13 Fitting of the exponential trap model with diffusion to experimental data

$$1-\tilde{\psi}(s)\xrightarrow{s\to 0}\frac{s\alpha}{\nu_0}\left[\frac{\pi(s/\nu_0)^{\alpha-1}}{\sin(\pi\alpha)}-\frac{1}{1-\alpha}\right] \quad . \tag{3.47}$$

As transit-time scale is large compared with reciprocal of the attempt frequency nu0, the asymptotic approximation is a good one. Substituing (3.47) into Eqs. (3.16) and (3.18), we find that the trapping function may be expressed as follows:

$$A(s)=\frac{L}{v}\left[s\left(1-\frac{\gamma\alpha/\nu_0}{1-\alpha}\right)+\frac{\pi\alpha}{\sin(\pi\alpha)}\left(\frac{s}{\nu_0}\right)^{\alpha}\right]\xrightarrow{s\to 0}\frac{L}{v}\frac{\pi\alpha}{\sin(\pi\alpha)}\left(\frac{s}{\nu_0}\right)^{\alpha} \tag{3.48}$$

Subsituting (3.48) into (3.36) then gives an expression for the current in the Laplace domain which can be readily inverted.

The fitting was performed by numerically inverting the Laplace transform for 30 representative data points from each of the transients. The results of the fitting are shown in Fig. 3.12. The theory seems to work quite well, even in the region of the tail. The field dependence of the fitted parameters is shown in Fig. 3.13. The mobility is calculated by dividing v by E. v/E, and the ratioD/μ, shows the deviation from the Einstein relation. We see that the mobility is field independent for the low field region (~10^3 V/cm).However, we can see a field-dependent region at higher fields. This may be caused by "the second source" mentioned in introduction of this chapter. We will discuss this high-field region further in Chapter 6. The diffusion constant Dseems to aquire a field-dependence between

low field region (~10^3 V/cm) and high field region (~10^4 V/cm). In low field region, however, D is almost field independent and the value of D/μ is close to kT/e=0.030.4 V which is what would be expected from the Einstein relation. Thus both D and mu are field independent in the low-field region. Although this is what one would expect, we should remark that a field-indpendent mobility together with a field-independent diffusion constant have never before been inferred from time of flight measurements on a disordered organic semiconductor mAt higher fields, the mobility begins to acquire a field dependence. The flaw in all of this is that trapping rate γ exhibits a strong field dependence, decreasing with increasing E. This is not consistent, for since D is constant, the diffusion-limited trapping

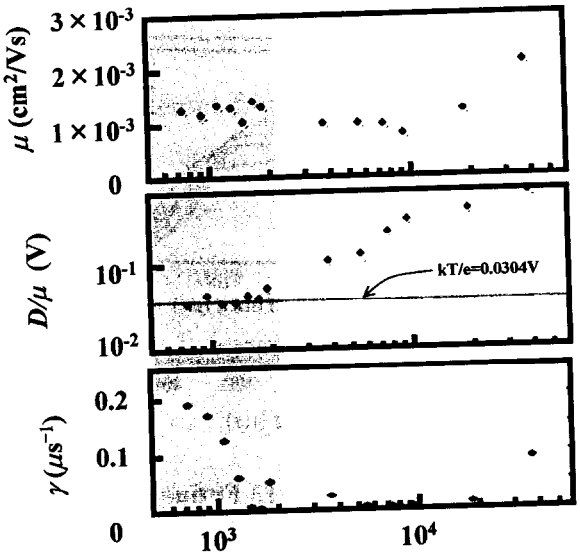

Fig. 3.14:Derived parameters from fitting exponential trap to experimental data

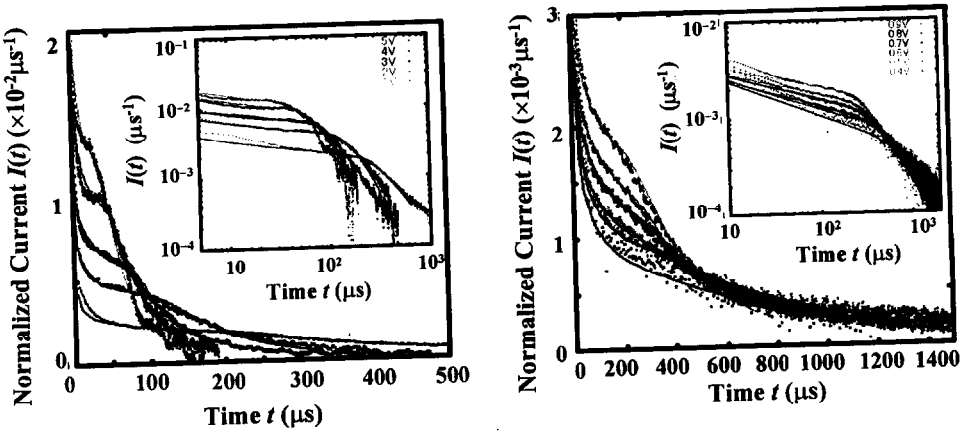

Fig.3.15 Fitting of the Gaussian trap model with diffusion to experimental data

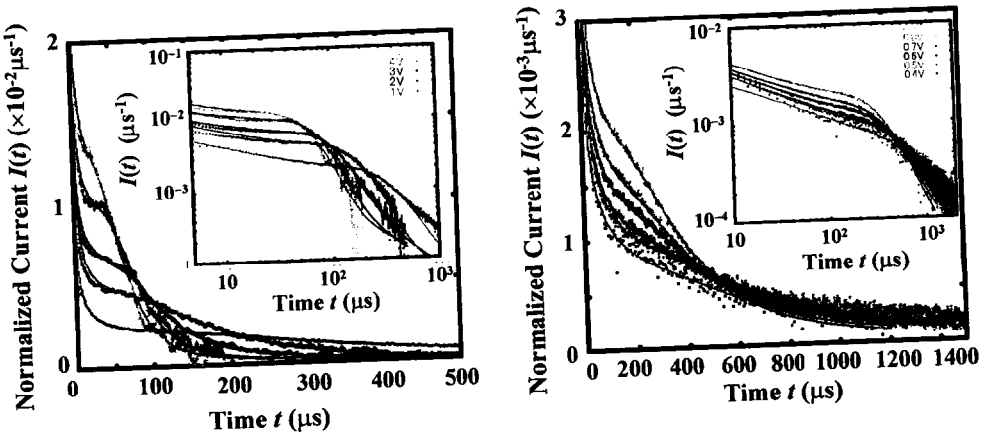

Fig.3.13 Fitting of the exponential trap model with diffusion to experimental data

rate should also be constant. Thus, we must conclude that an exponential distribution of traps is inadequate.

3.3.3 Gaussian distribution of traps

In this section we will examine the Gaussian trap distribution , described as

$$\rho(\varepsilon) = \frac{A}{\sqrt{2\pi\sigma^2}} \exp\left[-\frac{(\varepsilon-\varepsilon_0)^2}{2\sigma^2}\right], \tag{3.49}$$

where σ is the standard deviation and ε_0 is the mean. The fitting procedure is the same as that which we followed above for the case of the exponential trap distribution. In this case, however, we will obtain an expression for $A(s)$ in the form of a series expansion,

$$1-\tilde{\psi} = 1-\frac{A}{2}\left(1-\frac{\pi^2}{3!}\hat{\delta}^2+\frac{\pi^4}{5!}\hat{\delta}^4-\cdots\right)\left[\mathrm{Erf}\left(\frac{\lambda-\varepsilon_0}{\sqrt{2}\sigma}\right)+\mathrm{Erf}\left(\frac{\varepsilon_0}{\sqrt{2}\sigma}\right)\right]\Bigg|_{\lambda=kt\ln(s/\nu_0)} \tag{3.50}$$

where the operator $\hat{\delta} = \beta^{-1}\partial/\partial\lambda$. The details of this expansion will be explained in section 5.4.1, Chapter.5. We truncated the series after the 5th order in delta, and then performed the numerical Laplace inversion to fit the data at this level of approximation. In addition, we assumed the validity of the Einstein relation, $D = \mu kT/e$. Figure 3.14 shows the results. The model seems to work well, even for describing the tail region of the transient. The field dependence of the fiterived parameters is shown in Fig.3.14. The mobility is field-independent, and as is the diffusion constant. The standard deviation of the Gaussian trap

distribution is also a constant. This is all consistent with the idea of field-independent trap distribution. Unfortunately, γ seems to change with field. However, the region over which γ is field-independent is much broader than it was in the case of the exponential trap distribution. We conclude that the model is internally consistent in the range $E<10^4$ V/cm.

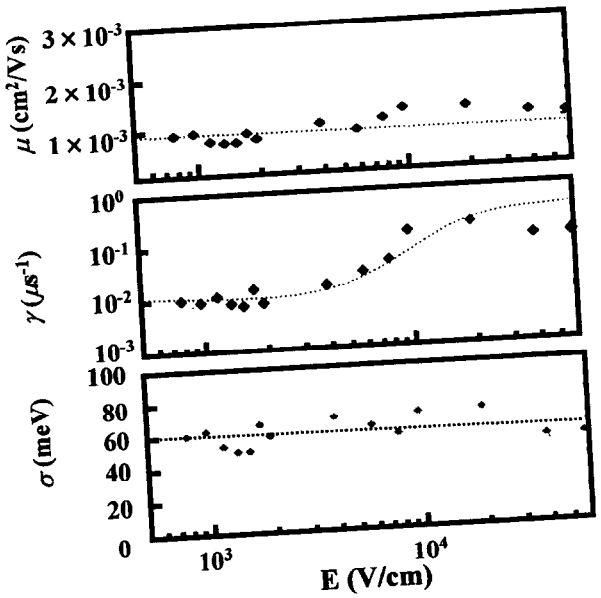

Fig. 3.14: Derived parameters from fitting Gaussian trap trap to experimental data

In evaluating the Gaussian trap distribution, the standard deviation σ is found to be 60 meV. This is comparable to the energetic disorder, as explained in Chapter 2 but it is rather small compared that found in most disordered organic materials . By fitting, we can also derive the parameter ε_0, but this is meaningless because we do not know the value for attempt frequency ν_0, which we have assumed arbitrarily, and the value of ε_0 depends on our choice of ν_0. This means that we can evaluate the width of the Gaussian trap distribution, but we can not find its absolute location relative to the energy of the transport manifold.

3.4 Conclusion

We have investigated carrier transport in smectic-liquid crystals (SmLC) by applying the multiple-trapping model (MTM) to describe the experimental photocurrent transients. We find that neither the simple MTM with convection but without diffusion, nor the convection-diffusion model without trapping, mare sufficient. We conclude therefore that trapping together with diffusion are important for describing the dispersion of the transients.. We then fit the experimental data with the MTM together with diffusion, and examined the results for several assumptions of the underlying trap distribution. We found

that a Gaussian trap distribution with a standard deviation of 60meV can explain the carrier transport in SmLC for a wide range of electric field in the low-field regime. These fits can be achieved while maintaining a field-indpendent mobility and agreement with the Einstein relation. has Although agreement with the Einstein relation is expected for low fields, it has never before been verified for a disordered organic system.

References

[1] D. Adam, F. Closs, T. Frey, D. Funfoff, D. Haarar, H. Ringsdorf, P. Shuhmacher and K. Siemensmeyer, Phys. Rev. Lett. **70**, 457 (1993)

[2] D. Adam, P. Shuhmacher, J. Siemmerer, L. Häussling, K. Siemensmeyer, K. Etzbach, F. Closs, H. Ringsdorf, and D. Haarar, Nature (London) **371**, 141 (1994)

[3] D. Adam, P. Schumacher, P. Simmerer, L. Häussling W. Paulus, K. Siemensmeyer, K. Etzbach, H. Ringsdorf, and D. Haarar, Adv. Mater. **7**, 276 (1995)

[4] R. Bilke, A. Schreiber, I. Bleyl, and D. Haarar, J. Appl. Phys. **87**, 8 (2000)

[5] D. Adam, P. Schumacher, L. Haussling, K. Siemensmeyer, K. H. Etzbach, D. Haarar and H. Ringsdorf, Nature **371**, 141 (1994).

[6] N. Boden, R. J. Bushby, A. N. Cammidge, J. Clements, R. Luo, and K. J. Donovan, Mol. Cryst. Liq. Cryst. Sci. Technol., Sect A **261**, 251 (1995).

[7] N. Boden, R. J. Bushby, J. Clements, B. Movaghar, K. J. Donovan and T. Kreouaius, Phys. Rev. B **52**, 13274 (1995).

[8] H. Nakayama, M. Ozaki, W. F. Schmidt, and K. Yoshino, Jpn. J. Appl. Phys. Part 2 **38**, L10358 (1999).

[9] M. Funahashi and J. Hanna, Jpn. J. Appl. Phys., Part 2 **35**, 703 (1996).

[10] M. Funahashi and J. Hanna, Appl. Phys. Lett. **71**, 602 (1997)

[11] M. Funahashi and J. Hanna, Phys. Rev. Lett. **78**, 2184 (1997).

[12] M. Funahashi and J. Hanna, Appl. Phys. Lett. **73**, 3733 (1998)

[13] M. Funahashi and J. Hanna, Appl. Phys. Lett. **76**, 2574 (2000)

[14] M. Funahashi and J. Hanna, Mol. Cryst. Liq. Cryst., **368**, 4071 (2001).

[15] I. Shiyanovskaya, K. D. Singer, R. J. Twieg, L. Sukhomlinova, and V. Gettwert, Phys. Rev. E, **65**, 041715 (2002).

[16] L. B. Schein, *Electrography and Development Physics*, 2nd edition (Springer, New York, 1992)

[17] P. M. Borsenberger, *Organic Photoreceptors for Xerography*, (Dekker, New York, 1998)

[18] I. H. Campbell and D. L. Smith, Sol. Stat. Phys. **55**, 1 (2001).

[19] A. Ohno and J. Hanna, Appl. Phys. Lett. **82**, 751 (2003).

[20] M. Funahashi and J. Hanna, Mol. Cryst. Liq. Cryst., in press.

[21] R. C. Enck and G. Pfister, *in Photoconductivity and Related Phenomena*, edited by J. Mort (Elsevier, New York, 1976), Chap. 7.

[22] H. Sher, and E. W. Montroll, Phys. Rev. B **12**, 2455 (1975).

[23] J. Noolandi, Phys. Rev. B **16**, 4466 (1977).

[24] J. Noolandi, Phys. Rev. B **16**, 4474 (1977).

[25] F. W. Schmidlin, Phys. Rev. B **16**, 2362 (1977).

[26] P. M. Borsenberger, L. T. Pautmeier, and H. Bässler, Phys. Rev. B **48**, 3066 (1993).

[27] J. C. Scott. L. T. Pautmeier, and L.B. Shein, Phys. Rev. B **46**, 8603 (1992).

[28] J. P. Bouchaud and A. Georges, Phys. Lett. **63**, 2692 (1989).

[29]A. Hirao, H. Nishizawa, and M. Sugiuchi, Phys. Rev. Lett **75**, 1787 (1995)

[30] A. Hirao, and H. Nishizawa, Phys. Rev. B **54**, 4755 (1996).

3. Macroscopic Analysis Using MTM and TOF Technique

Chapter 4

Study of Ionic and Electronic Transport

4.1 Introduction

In the previous chapter, the TOF-transient photocurrents for hole-transport in smectic liquid crystal (SmLC) materials were measured and analyzed using multiple-trapping model (MTM) with diffusion. In this chapter, we will concentrate on the transport of negative charge. Recent works [1,2] have shown that some smectic crystalline materials exhibit bipolar conduction in which the transport is quite different for positive and negative carriers. In TOF measurements for some negatively biased SmLC cells the photocurrent shows two kink points. We believe that the first kink point is due to the arrival of electrons, and the second signifies the arrival of anions. It is possible that the anions were originally neutral impurities which became ionized in the process of photoinjection. . Ionic conduction is not a new phenomenon in liquid crystals, and has been studied for a long time in the nematic phase [3-8]. In this chapter, we analyze negative carrier transport and investigate the relation between electronic transport and ionic transport by modeling the electron transport with the MTM, and modeling the ionic transport with the convection-diffusion equation.

4.1.1 Ionic transport in nematic liquid crystals

For the last three decades it has been believed that charge carrier transport in liquid crystalline materials is dominated by ionic conduction. . In most cases of NLCs, in fact, transient current studies have shown that the charge carriers are mobile-impurity ions. The effect of impurity ions in NLC has been extensively studied for the improvement of the device performance of NLC displays. The experimental techniques include measuring absorption current [3], transient current [4-6], leakage current [7] and complex dielectric constant as derived from the effect of ionic-space chargepolarization [8]. Mobile-impurity ions are a problem in displays because they build up at the

electrodes, causing an electrical field change in the bulk. This causes a degredation of the transmission-voltage characteristics.

Over the past five years, Sawada *et al*, has measured the complex dielectric constant of NLC(5CB) in low frequency regions ($<10^3$Hz) quantitatively in order to assess the effect of ionic-space charge polarization [9]. They measured the complex dielectric constant of 8CB for the temperature region in which the material exhibits both Nematic and Smectic phases [10]. The mobility was found to be on the order of 10^{-10}cm^2/Vs for the SmA phase , showing an activated temperature dependence. There was no indication of a discontinuity of the activation energy as would be expected from a phase transition.. In accordance with the Walden rule or, furthermore, Stokes-Einstein equation, the relationship between the mobility μ and the viscosity η can be expressed as,

$$\mu\eta = \frac{e}{6\pi r_s} \tag{4.1}$$

where r_s is the Stokes radius. If the ionic species remains the same in each phase, the product of the mobility and the viscosity should be a constant, independent of temperature. However, the product diverges near the vicinity of Nematic-Smectic phase transition in Nematic phase region, where the viscosity diverges . The divergence occurs due to the appearance of cybotactic clusters in the SmA phase [11]. Mobile ions can drift through the regions outside of the cybotactic clusters, i.e. regions with much lower viscosity (Fig.4.1), and for this reason the mobility does not depend on the

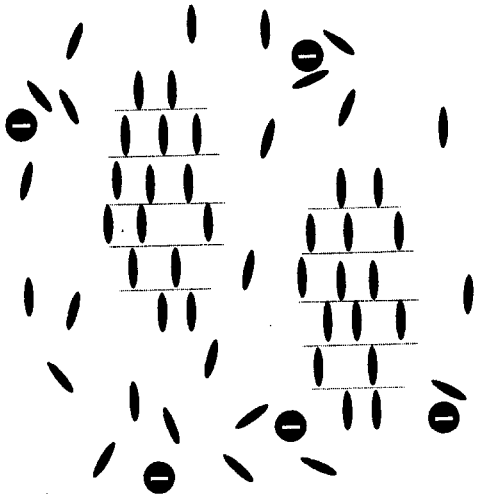

Fig. 4-1 : Image of pretransitional fluctuation: cybotactic cluster of SmA appears in Nematic phase. Ionic impurities conduct around the clusters

viscosity of the bulk.

4.1.2 Ionic Transport in Smectic Liquid crystals

The molecules of the cyano-biphenyl derivatives, such as 5CB, or 8CB, have only one alkyl chain. The aromatic core moieties have a π-conjugated overlap, which is responsible to stacking of condensed matter. Because the molecules stack very close to the alkyl chains of molecules in the adjacent layers of smectic phase,, there is no space for impurity to transport between layers without breaking the smectic phase stacking. On the other hand, the aromatic cores of the molecules composing SmLC, such as 2-phenyl naphthalene derivatives, as 8-PNP-O12 or 8-PNP-O4, have two long alkyl chains which are very far from one another (30Å~40Å). Impurity ions in this case can travel between the layerswithout affecting the π- π conjugated stacking between aromatic cores (Fig. 4.2).

Fast ionic conduction in SmLC can therefore occur in the "solvent" of the alkyl chains between smectic layers as long as the cohesive forces holding together the aromatic core moieties strong enough to prevent micro phase separation. One way to maintain the micro phase separation is to dimerize the molecules [12]. And another way is to synthesize the SmLC molecule so that it has long alkyl chains at both ends of the aromatic cores.

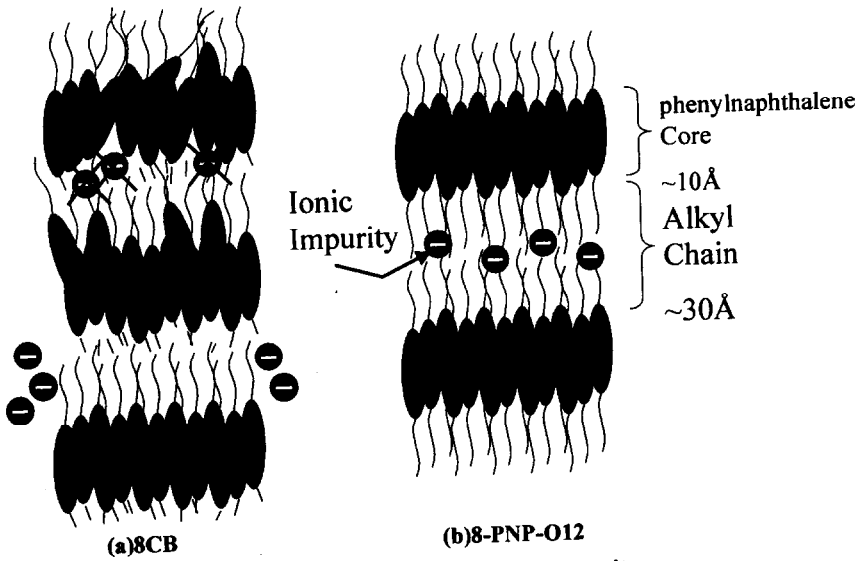

Fig. 4-2 :Schematic illustration of ionic impurity conduction for smectic liquid crystal

4.1.3 Electronic and ionic conduction in smectic liquid crystals

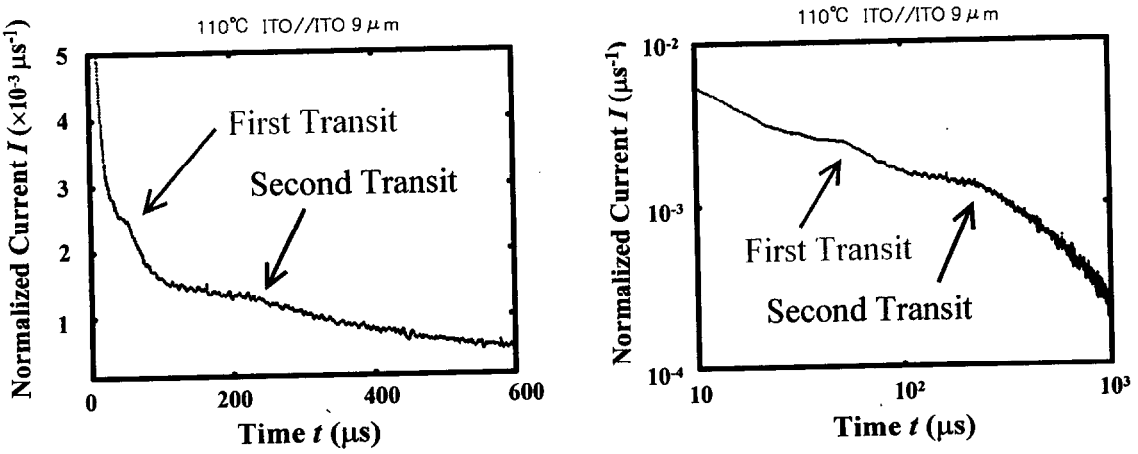

Fig. 4.3 : Transient photocurrents for negative carriers in SmA phase of 8-PNP-O12 at 120°C with (a)linear and (b)double logarithm plot. Two kink points were observed.

The details of the TOF measurement in SmLC of 2-phenylnaphtalene derivatives, i.e. 8-PNP-O12 is reported in detail in reference [2]. Even if the ionic conduction occurs in inter-layers, electronic conduction can independently occur through aromatic cores in intra-layer. An optical microscopic observation (Cross Nicol) shows that domain size is much larger than the sample thickness. A charge carrier can therefore move from one end of the sample to the other without having to cross over domain boundaries. As mentioned above, the transient photocurrent for negative carriers shows two kink points (transits) in both SmA and SmB phases (Fig.4.3). The idea that the first one is due to electrons and the second one is due to anions can be confirmed from two facts. One is concerns the temperature dependence of the mobilities which are calculated from the two transit times. The first transit time implies a mobility with no temperature dependence, which is similar in magnitude to the hole mobility obtained from a positively biased TOF measurement (~2.4×10^{-4}cm^2/Vs in SmA and ~1.6×10^{-3}cm^2/Vs in SmB[2]). On the other hand, the second transit time implies a thermally activated mobility (2~6×10^{-5}cm^2/Vs), having an activation energy of 0.23eV in the SmA phase and 0.31e in the SmB phase. These are typical values for the activation energies for ion transport in other fluids. The other fact is that, when the sample is diluted with n-dodecane (20mol% dilution in experiment), the mobility as calculated from the first

transit time shows little change as compared to the mobility in the pure sample, whereas the mobility calculated from the second transit time varies greatly with dilution. The dilution-dependence implies that n-dodecane does not migrate into the intra-layers but only into the inter-layers. Thus, the n-dodecane does not enlarge the distance between the nearest neighbor molecules in intra-layer, which are responsible to the mobility due to electron hopping. On the other hand n-dodecane reduces the viscosity in the inter-layers, which results in higher mobility for the diluted sample than that for pure sample by lowering the viscosity. These details are discussed in reference [2].

4.1.4 Photocurrent of Electronic and ionic carrier in smectic liquid crystals

In this thesis, we concentrate not on injecting current but on photocurrent of the cell sandwiched by blocking electrodes. Then, all of the detected charges, including both electrons and ions, are derived from charge separation due to exciton generated by light of pulsed laser. Thus the ionic impurities contributing to the photocurrent were neutral impurity before the pulsed laser was flashed. So, the simple question arises, i.e. "When is the neutral impurity ionized?" In this chapter, we analyze a negatively-biased TOF photocurrent, modeling the transient with a combination of MTM and convection-diffusion. We attempt to fit the experimental results of the TOF photocurrent, and we discuss our findings. Lastly, the physical implications of the parameters obtained from the fits will be discussed.

4.2 Models

Following the model developed in Chapter 3, we suppose here that the electron transport can be described by the MTM. Let us suppose that electrons travel with velocity v_e. To simplify the problem, let us consider the one-trap model, and neglect diffusion in the transport manifold. Let us further suppose that ionic transport can be described by the convection-diffusion equation with a drift velocity v_{ion} and a diffusion constant D_{ion}

Let us assume that the ions are generated by the same laser pulse which generates the electron-hole pairs for electron transport. In such a case, all photo-carriers detected

in the TOF photocurrent must originate from the charge separation of the excitons which are generated in the SmLC molecules. Mobile ions may form according to two models:

Model 1 : Bulk Ionizing Model

After the charge separation of an exciton occurs, initially all of the charge carriers are electrons. Ionic transport then follows electron transport when an electron is captured by an impurity molecules which is free to drift (impurity ionization process, Fig.4.4).

Model 2 : Interface Ionization Model

The charge separation of the exciton occurs by two processes. One process occurs on SmLC molecule, the other occurs on the impurity near the electrode interface. In this electronic and ionic conduction occur simultaneously and independently.(Fig.4.5)

4.2.1 Model1: Bulk Ionization Model (Fig.4.4)

This model assumes that the initial condition is such that the electron distribution is a delta function near the surface of the illuminated electrode, and that there are initially no carriers in trap states, and no anions in the bulk. Let us suppose that the total trapping rate γ is the summation of the "ordinary trapping rate" with which the carriers are shifted between the transport manifold and the trap manifold, and the "ionic rate" with which the carriers are shifted from the transport manifold to the impurity manifold. Taking X_{ion} to be the ratio of the ionic trapping rate to γ., the "ordinary trapping rate" will be denoted as $\gamma(1\text{-}X_{ion})$ and the "ionic rate" will be denoted as γX_{ion}. *The rate R* will be the release rate with which the carriers are able to move from a trap state to a transport state. We will assume that there the return rate from the ionic manifold to the

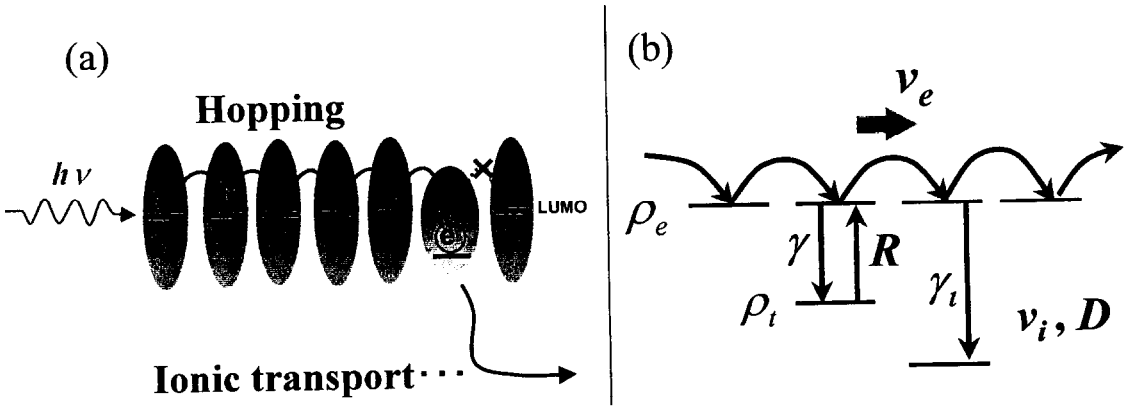

Fig. 4.4 :(a)Schematic illustration and (b) picture notated parameters of "ionizing on bulk model" : Impurity ionizing process occurs by capturing electron carrier on the impurity

transport manifold may be neglected. The MTM equation for electron transport state is therefore expressed as follows:

$$\frac{\partial \rho_e(x,t)}{\partial t} = -v_e \frac{\partial \rho_e(x,t)}{\partial x} - \gamma \rho_e(x,t) + R\rho_t(x,t) + \delta(x)\delta(t). \tag{4.2}$$

$$\frac{\partial \rho_t(x,t)}{\partial t} = \gamma(1 - X_{ion})\rho_e(x,t) - R\rho_t(x,t). \tag{4.3}$$

where x is the distance from illuminated electrode; $\rho_e(x,t)$ is the probability that an electron is in transport state, and $\rho_t(x,t)$ is the probability for an electron to be in a trap state. The last term in equation (4.2) is the initial condition. For ionic transport, we apply the convection-diffusion equation, i.e.,

$$\frac{\partial \rho_{ion}(x,t)}{\partial t} = -v_{ion} \frac{\partial \rho_{ion}(x,t)}{\partial x} + D_{ion} \frac{\partial^2 \rho_{ion}(x,t)}{\partial x^2} + \gamma X_{ion} \rho_e(x,t). \tag{4.4}$$

The last term describes the increase in the ionic charges as supplied by capture of electrons by impurities, and $\rho_{ion}(x,t)$ is the normalized density of ions.

Let us now introduce the Laplace transforms of equations (4.2)~(4.4).

$$s\tilde{\rho}_e(x,s) = -v_e \frac{\partial \tilde{\rho}_e(x,s)}{\partial x} - \gamma \tilde{\rho}_e(x,s) + R\tilde{\rho}_t(x,s) + \delta(x). \tag{4.5}$$

$$s\tilde{\rho}_t(x,s) = \gamma(1 - X_{ion})\tilde{\rho}_e(x,s) - R\tilde{\rho}_t(x,s). \tag{4.6}$$

$$\tilde{\rho}_{ion}(x,s) = -v_{ion}\frac{\partial\tilde{\rho}_{ion}(x,s)}{\partial x} + D_{ion}\frac{\partial^2\tilde{\rho}_{ion}(x,s)}{\partial x^2} + \gamma X_{ion}\tilde{\rho}_e(x,s). \tag{4.7}$$

where s is Laplace variable; The tildes denote the Laplace transform. The function. $\tilde{\rho}_t(x,s)$ is derived from eq.(4.6), i.e.,

$$\tilde{\rho}_t(x,s) = \frac{\gamma(1-X_{ion})}{s+R}\tilde{\rho}_e. \tag{4.8}$$

Substitution of eq.(4.8) into eq.(4.5) gives

$$s\tilde{\rho}_e(x,s) = -v_e\frac{\partial\tilde{\rho}_e(x,s)}{\partial x} - \gamma\tilde{\rho}_e(x,s) + \frac{\gamma R(1-X_{ion})}{s+R}\tilde{\rho}_e(x,s) + \delta(x). \tag{4.9}$$

Solving equation (4.9) for rho-e, we find

$$\therefore \tilde{\rho}_e(x,s) = \frac{1}{v_e}\exp[-\Gamma(s)x], \tag{4.10}$$

where $$\Gamma(s) = \frac{\gamma s}{v_e}\left[\frac{1}{\gamma} + \frac{s+RX_{ion}}{s(s+R)}\right]. \tag{4.11}$$

The trap state density may then be obtained by substituting (4.10) into (4.8), giving

$$\tilde{\rho}_t(x,s) = \frac{\gamma(1-X_{ion})}{v_e}\exp[-\Gamma(s)x]. \tag{4.12}$$

The normalized carrier density of the ions may be obtained by substituting eq.(4.10) into eq.(4.7);

$$\tilde{\rho}_{ion}(x,s) = -v_{ion}\frac{\partial\tilde{\rho}_{ion}(x,s)}{\partial x} + D_{ion}\frac{\partial^2\tilde{\rho}_{ion}(x,s)}{\partial x^2} + \frac{\gamma X_{ion}}{v_e}\exp[-\Gamma(s)x]. \tag{4.13}$$

It follows that

$$\tilde{\rho}_{ion}(x,s) = C_1 e^{\xi(1+\varsigma)x} + C_2 e^{\xi(1-\varsigma)x} - \frac{\gamma X_{ion}}{v_e}\frac{\exp[-\Gamma(s)x]}{D_{ion}\Gamma(s)^2 + v_{ion}\Gamma(s) - s}, \tag{4.14}$$

where

$$\xi = v_{ion}/2D_{ion}, \tag{4.15}$$

and

$$\varsigma = \sqrt{1+4D_{ion}s/v_{ion}^2}. \tag{4.16}$$

In the experiment, the sample is sandwiched by blocking electrodes. We will model this by taking a perfectly reflecting boundary at the injecting electrode and a perfectly absorbing boundary at the counter electrode, i.e.,

$$J_{ion}(x=0;t)=v_{ion}\rho_{ion}(0,t)-D_{ion}\frac{\partial\rho_{ion}(0,t)}{\partial x}\equiv 0 \tag{4.15}$$

and

$$\rho_{ion}(L,t)=0. \tag{4.16}$$

Under these conditions, we can determine the constants appearing in eq.(4.13);

$$C_1=\frac{\Omega X_{ion}}{v_e}\Phi, \tag{4.17}$$

and

$$C_2=-\frac{\Omega X_{ion}}{v_e}\Psi, \tag{4.18}$$

where

$$\Omega=\frac{\gamma}{D\Gamma(s)^2+v_{ion}\Gamma(s)-s}, \tag{4.21}$$

$$\Phi=\frac{(\Gamma(s)+2\xi)e^{\xi(1-\varsigma)L}-\xi(1+\varsigma)e^{-\Gamma(s)L}}{-\xi(1+\varsigma)+\xi(1-\varsigma)e^{-2\xi\varsigma L}}e^{-\xi(1+\varsigma)L} \tag{4.22}$$

and

$$\Psi=-\frac{\xi(3-\varsigma-2\Phi)+\Gamma(s)}{\xi(1+\varsigma)}. \tag{4.23}$$

An expression for the total charge in the sample, $Q(t)$, may then be drived by substituting (4.5)~(4.7);

$$\frac{dQ(t)}{dt}=\frac{d}{dt}\int_0^L dx\left[\rho_e(x,t)+\rho_t(x,t)+\rho_{ion}(x,t)\right]=D_{ion}\left.\frac{\partial\rho_{ion}(x,t)}{\partial t}\right|_{x=L}, \tag{4.24}$$

It follows that the current is given by

$$\begin{aligned}I&=\frac{1}{L}\int_0^L dx x\frac{\partial}{\partial t}\left[\rho_e(x,t)+\rho_t(x,t)+\rho_{ion}(x,t)\right]-\frac{dQ(t)}{dt}\\&=\frac{D_{ion}}{L}\left[\rho_{ion}(0)-\rho_{ion}(L)\right]-\frac{1}{L}\int_0^L dx\left[v_e\rho_e(x,t)+v_{ion}\rho_{ion}(x,t)\right].\end{aligned} \tag{4.25}$$

Substituting eqs.(4.10), (4.12) and (4.14) into eq.(4.25), we obtain a closed form for the current in the Laplace domain,

$$\tilde{I}(s)=\frac{1}{\Gamma(s)L}\left(1-e^{-\Gamma(s)L}\right)+\frac{\Omega X_{ion}}{v_e}\left\{\Phi\left[D_{ion}e^{-\xi(1+\zeta)L}+\frac{v_{ion}}{\xi(1+\zeta)}\left(1-e^{-\xi(1+\zeta)L}\right)\right]\right.$$

$$-\Psi\left[D_{ion}+\frac{v_{ion}}{\xi(1-\zeta)}\left(e^{\xi(1-\zeta)L}-1\right)\right]-\left[D_{ion}+\frac{v_{ion}}{\Gamma(s)}\left(1-e^{-\Gamma(s)L}\right)\right]\Bigg\} \quad . \tag{4.26}$$

4.2.2 Model 2: Interface Ionization Model (Fig. 4.5)

In this model, electrons and ions move independently. We begin by defining the initial ratio of ionic charge as

$$W_{ion}=\frac{Q_{ion}(0)}{Q_{all}(0)}, \tag{4.27}$$

where $Q_{ion}(t)$ and $Q_{all}(t)$ are the total ions in the sample and the total negative charges in the sample, respectively. The initial distribution of electrons in the transport state is given by

rhoe(x,0)=(1−W_{ion})*delta(x).

The initial distribution of ions in the ionic transport path between smectic layers is given by

rhoi(x,0)= W_{ion} *delta(x).

The trapping rate γ is the rate with which carriers are shifted from the transport manifold to the trap manifold, and R is the rate of return. The MTM equations for electronic transport are as follows:

$$\frac{\partial\rho_e}{\partial t}=-v_e\frac{\partial\rho_e}{\partial x}-\gamma\rho_e+R\rho_t+(1-W_{ion})\delta(x)\delta(t)\,., \tag{4.28}$$

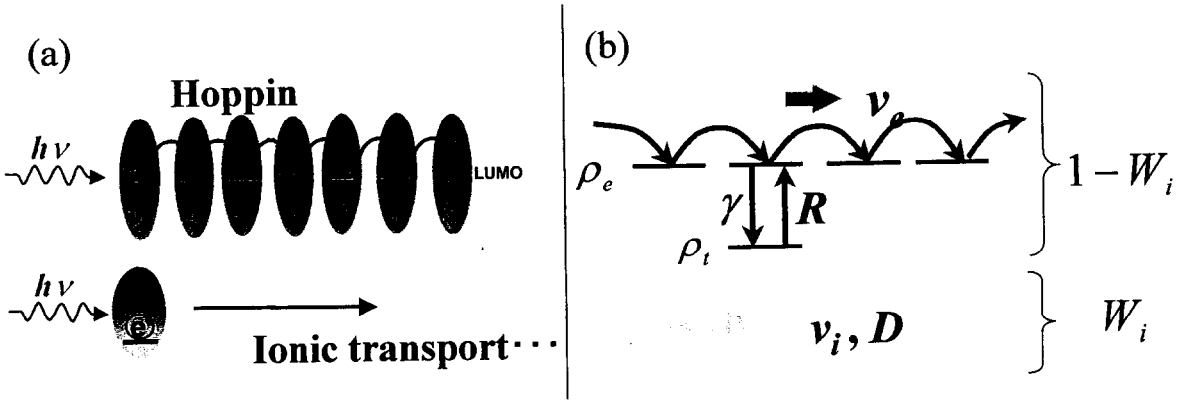

Fig. 4.5 :(a)Schematic illustration and (b) picture notated parameters of "ionizing on interface model" : Impurity ionizing process occurs by charge separation on interface independent from electron carrier generation

$$\frac{\partial \rho_t}{\partial t} = \gamma \rho_e - R\rho_t . \tag{4.29}$$

is the ionic transport is completely described by the convection-diffusion equation,

$$\frac{\partial \rho_{ion}}{\partial t} = -v_{ion}\frac{\partial \rho_{ion}}{\partial x} + D\frac{\partial^2 \rho_{ion}}{\partial x^2} + W_{ion}\delta(x)\delta(t) . \tag{4.30}$$

Equations (4.28) and (4.29) are equivelent to those used in the one-trap modela. The only distinction is that the total electronic charge is normalized to $1 - W_{ion}$. The solutions to eq. () – () are as follows:

$$\tilde{\rho}_e(x,s) = \frac{1-W_{ion}}{v_e}\exp[-\Gamma(s)x] \tag{4.31}$$

$$\Gamma(s) = \frac{\gamma s}{v_e}\left[\frac{1}{\gamma} + \frac{1}{s+R}\right] \tag{4.32}$$

$$\tilde{\rho}_t(x,s) = \frac{\gamma(1-W_{ion})}{v_e(s+R)}\exp[-\Gamma(s)x] \tag{4.33}$$

The solution to equation (4.30) is given by

$$\tilde{\rho}_{ion}(x,s) = C_1 e^{\xi(1+\zeta)x} + C_2 e^{\xi(1-\zeta)x} + \frac{W_{ion}}{2D_{ion}\xi}e^{\xi(1-\zeta)(x-a)} \quad \text{for } x \geq a , \tag{4.34-a}$$

and

$$\tilde{\rho}_{ion}(x,s) = C_1 e^{\xi(1+\zeta)x} + C_2 e^{\xi(1-\zeta)x} + \frac{W_{ion}}{2D_{ion}\xi}e^{\xi(1+\zeta)(x-a)} \quad \text{for } x \geq a \tag{4.34-b}$$

Here a is the location of the intial electron density, which we will set to zero. i.Under the same boundary conditions used in the bulk ionization model, the constants C1 and C2 are given by

$$C_1 = -\frac{W_{ion}e^{-2\xi L}}{D_{ion}\xi\left[1+\zeta+(1-\zeta)e^{-2\xi L}\right]} , \tag{4.35}$$

$$C_2 = -\frac{W_{ion}(1-\zeta)(1-e^{-2\xi L})}{1+\zeta+(1-\zeta)e^{-2\xi L}} . \tag{4.36}$$

where α and β are given by eq. (4.16).

Finally, we obtain a description of thephotocurrent in the Laplace domain, i.e.,

$$\tilde{I}(s)=\frac{1-W_{ion}}{\Gamma(s)L}\left(1-e^{-\Gamma(s)L}\right)$$
$$+\frac{1}{L}\left[D_{ion}(C_1+C_2)+\frac{W_{ion}}{2\xi}\right]$$
$$+\frac{v_{ion}C_1}{\xi(1-\zeta)L}\left[1-e^{-\xi(1-\zeta)L}\right]+\frac{v_{ion}C_2}{\xi(1+\zeta)L}\left[1-e^{-\xi(1+\zeta)L}\right]$$
$$+\frac{v_{ion}W_{ion}}{2\xi^2(1+\zeta)D_{ion}L}\left[1-e^{-\xi(1+\zeta)L}\right] \tag{4.37}$$

4.2.3 Mixture Model 1& Model 2

There is a possibility that the bulk-ionization process and the interface-ionization process occur simultaneously. This can be modeled by combining the two models, as follows:

(1) All negative carriers multiplied by W_{ion} initially ionize and transports as ions, such as the ions in Interface-Ionization Model.

(2) All negative carriers multiplied by (1-W_{ion}) transport accordingly as Bulk-Ionization Model.

In this manner, we find a form describing the Laplace transformed photocurrent for the combined model,

$$\tilde{I}(s)=\frac{1-W_{ion}}{\Gamma(s)L}\left(1-\exp\left(-\Gamma(s)L\right)\right)$$
$$+\frac{(1-W_{ion})\Omega X_{ion}}{v_e}\left\{\Phi\left[D_{ion}e^{-\alpha L}+\frac{v_{ion}}{\alpha}\left(1-e^{-\alpha L}\right)\right]\right.$$
$$\left.-\Psi\left[D_{ion}+\frac{v_{ion}}{\beta}\left(e^{\beta L}-1\right)\right]-\left[D_{ion}+\frac{v_{ion}}{\Gamma(s)}\left(1-e^{-\Gamma(s)L}\right)\right]\right\}$$

$$+\frac{W_{ion}}{L}\left\{\left[D_{ion}(C_1+C_2)+\frac{1}{\alpha+\beta}\right]\right.$$
$$\left.+\frac{v_{ion}C_1}{\beta}\left[1-e^{-\beta L}\right]+\frac{v_{ion}C_2}{\alpha}\left[1-e^{-\alpha L}\right]+\frac{v_{ion}}{\alpha(\alpha+\beta)D_{ion}}\left[1-e^{-\alpha L}\right]\right\} \quad (4.38)$$

Finally, we may also consider the inverse process of Model 1; Ionic transport due to impurity ions generated at the illuminated cathode may change into electronic transport in SmLC molecules after thermal excitation. But this process would result in a rapid increase of the photocurrent because the electron mobility is approximately ten times higher than the ionic mobility. We will not consider this possibility, as such behavior of thetransient has not been observed experimentally.

4.2.4 Analysis of experimental results

We have used the three models explained in 4.3 to fit the experimental photocurrent transients, normalized to the total integrated charge. For this study, the sample was 8-PNP-O12 sandwiched between ITO electrodes, and the cell thickness was 9 μm. The temperature ranged from 80°C to 125°C (SmA and SmB) the voltage ranged from –20V to –100V. the number of sampling data for the fitting was between 30 and 50 points for each transient. The parameters extracted from the fits were v_e, γ, R, v_{ion}, D_{ion}, X_{ion} and W_{ion}.

4.3 Photocurrent in Smectic A phase

4.3.1 Application of Bulk Ionization Model

In this section we will apply Model 1, the Bulk Ionization Model, in order to describe the phototransients for the Smectic A phase. We will see that it is not possible to fit the data, even when adjusting all 6 parameters. . First, let us focus on fitting the parameters concerning ion transport, i.e. v_{ion}, D_{ion}, and γX_{ion}, while holding the other 3 parameters concerning electron transport constant. We began by fitting 30 representative points in the neighborhood of the second kink point. As expected, the

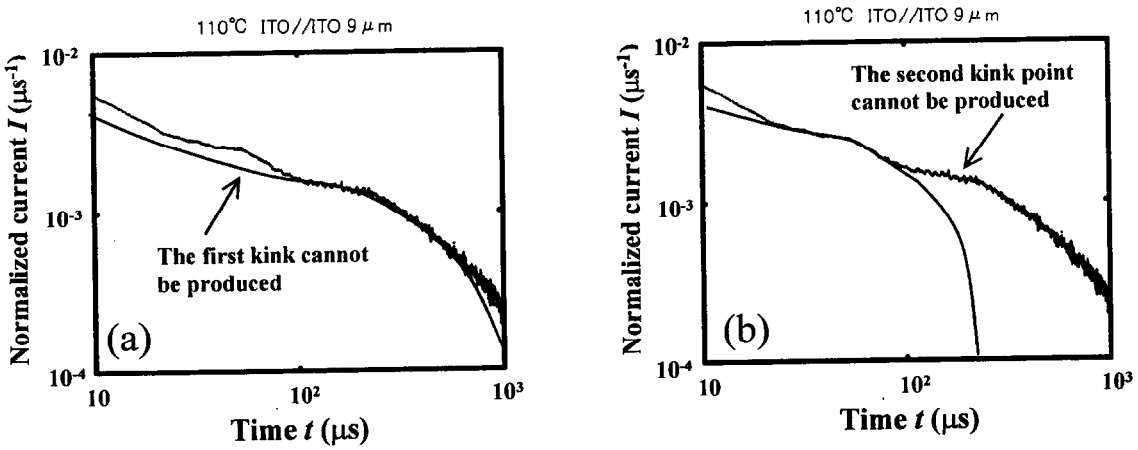

Fig. 4.6 : Applying Bulk Ionization Model to SmA phase: the procedure of (a) is fitting the parameters concerning ionic transport first, followed by fitting the parameters concerning electronic transport. The procedule (b) is fitting the parameters for electronic transport first, followed by that for ionic transport.

fitting around the second kink point was very good, but the fit was poor in the neighborhood of the first kink point. We then held these ionic parameters constant, and attempted to fit the electron transport parameters v_e, R and $\gamma(1-X_{ion})$, taking 30 points of sampling data around the first kink point. However, the theory was not flexible enough to reproduc the signal around the first kink point. The result of this fitting is shown in Fig4.6-(a).

The reason for the failure is as follows. The transported ions are generated by electron capture of impurities present. To reproduce the second kink point, therefore, a high enough density of charge must be captured in the within thetransit time of the second kink. This capturing occurs too rapidly for the electron density to produce the current signal around the first kink point. On the other hand, we also tried to fit by inverse procedure, i.e., fitting the electron kink first, followed by the fitting of the ionic kink To carry this out, the parameters v_e, R, and $\gamma(1-X_{ion})$ were chosen to fit around the first kink point while holding the ionic parameters fixed. After this fitting, we tried to find v_{ion}, D_{ion}, and γX_{ion} to allow the theory to pass through the second kink point. Again, the theory was unable to fit both kink points simultaneously, as shown in (Fig.4.6-(b)). To reproduce the first kink point of the current signal numerically, requires a high enough density of electrons. This requires that most of the negative carriers remain as

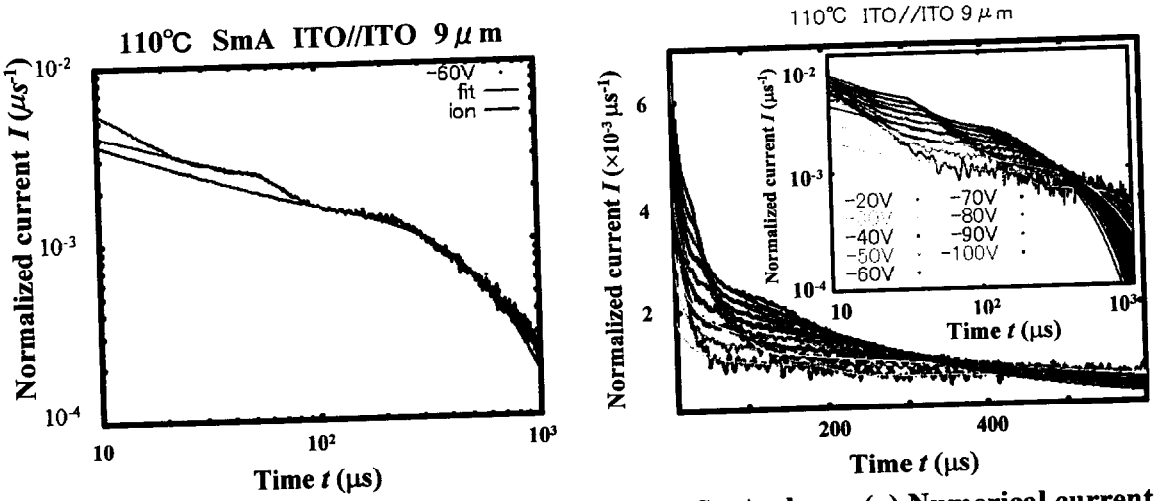

Fig. 4.7 : Applying Interface Ionization Model to SmA phase: (a) Numerical current fitting for experimental photocurrent and the current of ionic contribution. (b) The fitting for various field. (inset is on double logarithmic scale)

electrons, arriving at the counter electrode before being captured by impurities. Thus there remains little ionic charge to reproduce the second kink point of the current signal.

4.3.2 Application of Interface Ionization Model

We next attempted to describe negative carrier transport in the Smectic A phase with Model 2, the Interface Ionization Model. In this case, the 5 parameters, v_e, γ, R, v_{ion}, D_{ion} and W_{ion}, were fit simultaneously to 50 representative points, 20 of which were taken around the first kink point and the remaining 30 taken around the second kink point. The fitting worked extremely well, for the numerically calculated current was able to reproduce both kink points, as shown in Fig.4.7-(a). The failure of the Bulk Ionization Model, and the success of the Interface Ionization Model, implies thatthat the formation of impurity ions occurs primarily near the interface. Apparently, impurity ion formation due to capture of electrons transporting in the bulk is not as efficient a process.

The contribution from ionic transport of Bulk Ionization Model to the current is plotted in the Fig.4.7-(a). The difference between the fitting current and ionic contribution to the current is the contribution from electronic transport. The figure shows that major part of the numerical photocurrent comes from the contribution of

ionic transport. Namely, ionic conduction is dominant in negative charge conduction in thin cell of SmA material.

4.4 Photocurrent in Smectic B phase

4.4.1 Application of Bulk Ionization Model and Interface Ionization Model

In our examination of negative carrier transport in the SmB phase we repeated the same analysis used for the SmA phase. The best fit curves for the Bulk Ionization Model are shown in (Fig4.8-(a)). Just as in the SmA case, the Bulk Ionization Model was unable to fit both kink points.,

Unfortunately, the Interface Ionization Model was also unable to fit the data. Just as in the SmA case, the 5 fitting parameters, v_e, γ, R, v_{ion}, D_{ion} and W_{ion}, were adjusted simultaneously for 20 sampling points around the first kink point and for 30 sampling points around the second kink point. Although the theory can produce two kink points, as shown in Fig. 4.8-b, the location of these kink points can not be made to coincide with the two kink points in the data. To summarize, neither ionization processes in the bulk nor ionization processes at the interface appear to be dominant in SmB phase. This raises the question as to whether or not the transients in the SmB phase can be fit by a compbination of both processes, a model which we will call model 3, the Mixture

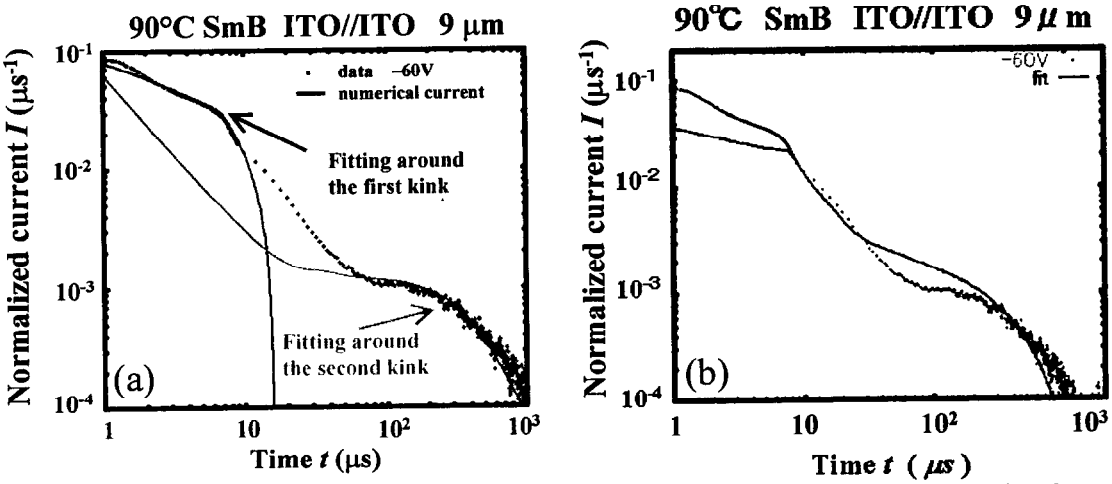

Fig. 4.8 : Applying the models to SmB phase: (a) Application of Bulk Ionization Model and (b) Application of Interface Ionization Model.

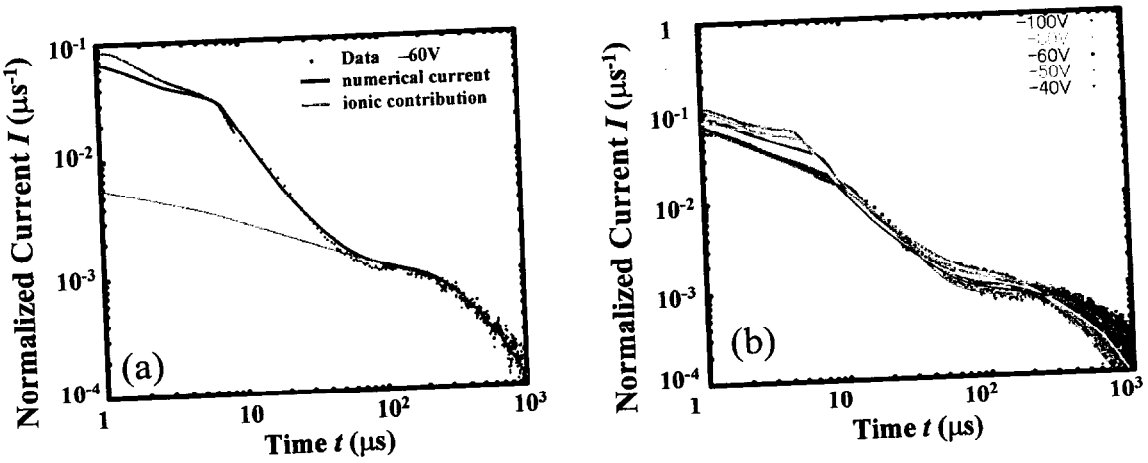

Fig. 4.9 : Appling of the Mixture Model to SmB phase: (a) Numerical current fitting for experimental photocurrent and the current of ionic contribution. (b) The fitting for various field.

Model.

4.4.2 Application of Mixture Model

Figure 4.9 shows the application of the Mixture Model to the experimental photocurrent in the SmB phase. When all 6 parameters are adjusted at the same time we find that we are able to describe the data.. Thus, Mixture Model can explain the experimental data. Fig.4.9-(a) also shows the ionic contribution separately. We can see that the ionic current changes behavior after the first transit time. The reason is because after the first kink, most of the electrons have reached the counter electrode, and so few remain which can still convert to mobile ions.

4.5 Results & Discussion

We have examined the several models to explain TOF photocurrents in both SmA and SmB phases of 8-PNP-12. The photocurrent in SmA phase can be explained by Interface Ionization Model. The photocurrent in SmB phase can be explained by Mixture Model. Both of the models yield various fitting parameters, including the total trapping rate γ, release rate R and ionic trapping rate γX. The initial ratio of ionic carrier W_{ion} can also extracted, this parameter depending on liquid crystalline phase.

Let us focus, however, on the electronic-intrinsic and ionic-intrinsic mobilities which can be inferred from the two velocity parameters.

4.5.1 Mobility

Figure 4.10 shows the field and temperature dependence of the mobility for both electrons and negative ions for the SmA and SmB phases. The calculated intrinsic mobility are the same as usually derived from experimental results, i.e., via the direct measurement of the transit time as determined from the kink [2,14,13]. The electric mobility is $2.4\times10^{-4}cm^2/Vs$, and does not have field nor temperature dependence in the range measured. The ionic mobility does not have field dependence but it does have an activated temperature dependence

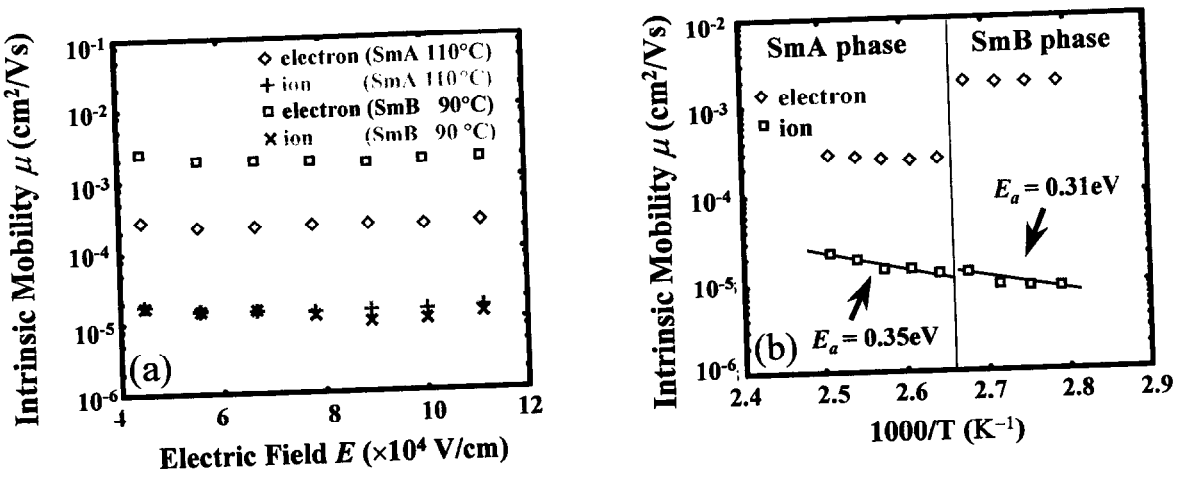

Fig. 4.10 : Intrinsic Mobility of electron and ion worked out fitting parameters. (a)Field dependence and (b) Temperature dependence are showed.

as shown in the Arrhenius plot of Fig.4.10-(b). The typical ionic mobility is $1.4\times10^{-5}cm^2/Vs$ for SmA phase at 110°C and $1.1\times10^{-5}cm^2/Vs$ for SmB phase at 90°C, as showed in Fig.4.10-(a). These values are about 1/3 of the value evaluated by a direct measurement of the transit time at the kink point. The reason for the discrepancy is that the time measured at the kink poin is the time when the carrier distribution starts to arrive the counter electrode., and so does not represent the average drift speed. The activation energy are determined from the slopes in Fig.4.10-(b), and are given by

0.35eV for SmA phase and 0.31eV for SmB phase. These are typical values for the activation energies of ions moving in a fluid media.

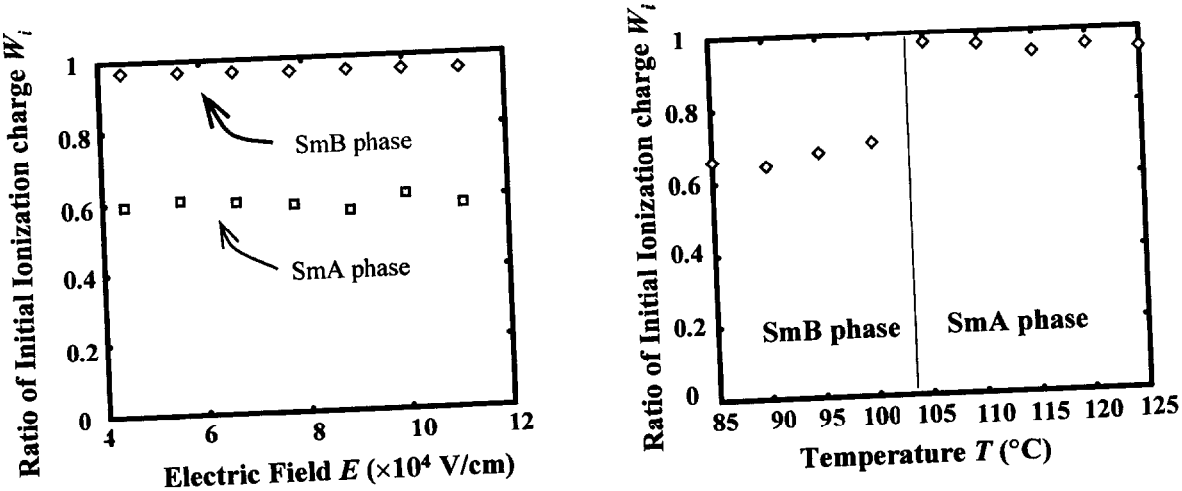

Fig. 4.11 : Ratio of initial ionization charge worked out by fitting. (a)Field dependence and (b) Temperature dependence are showed.

4.5.2 Ratio of initial ionic carrier W_{ion}

Figure 4.11 shows the field and temperature dependence of the ratio W_{ion} of the initial number of ions to the total number of injected charges.. In the SmA phase, about 95% of carriers initially contributing to photocurrent are impurity ions at 110°C. The ratio W_{ion} has no field dependence but has a little temperature dependence. As the temperature increases, the ratio decreases slightly. In the SmB phase, about 65% of the carriers contributing to the photocurrent are comprised of impurity ions at 90°C. The ratio increases with increasing field, but has a little temperature dependence. . The sample thickness dependence of the ratio of total electric carriers to all carriers, $1-W_{ion}$ is discussed on Iino *et al* in ref.2 (, i.e., $(Q_e/Q_{all})_{d=0}$ in ref.2). They measured the sample-thickness (d) dependence of $1-W_{ion}$ in the sample and derive $1-W_{ion}$ by extrapolation, $d\rightarrow 0$. They found that the extrapolated value did not become unity. They thought that a certain amount of negative ions is initially formed before the photo-generated electron transport start. This conclusion is consistent with the results here.

It is interesting that the initial ionization process is dominant compared with bulk ionization process. The fraction of carriers which become impurity ions before electronic transport starts is 0.95 (in SmA) and 0.65 (in SmB) The fraction strongly depends on the phase of the liquid crystal. We think that the initially ionizied impurity is created from the neutral impurities which are distributed on the interface of the illuminated cathode. For example, it is known that dissociation of excitons occurs favorably for highly ordered SmB phase, whereas, for the SmA phase, dissociation of excitons occurs in the presence of impurities at the cathode [16].

4.6 Conclusions

In this chapter we analyzed the negative carrier transport in SmA and SmB phases. The photocurrent decay curves having two kink points (transits) , the first having to do with the arrival of electrons, and the second having to do with the arrival of ions.We attempted to fit the photo transients with three multiple trapping models describing simultaneous transport of electrons and ions. We concluded that the Interface Ionization Model can explain the photocurrent in SmA phase, and the Mixture Model, which combines the processes of bulk ionization and interface ionization, can explain the photocurrent in SmB phase.

We then analyzed the parameters which are derived from the fitting of theses models to the experimental data. The temperature and field dependence of the mobility of the electrons, and of the ions was determined. The mobility of the ions was found to be about 1/3 of what you would expect based on estimating a transit time from the second kink point in the transient.

References

[1] M. Funahashi and J. Hanna, Phys. Rev. Lett. **78**, 2184 (1997).

[2] Hiroaki Iino, unpublished.

[3] H. Mada and S. Yoshino, Jpn. J. Appl.Phys **27**, L1361 (1988).

[4] G. H. Heilmeier and P. M. Heyman, Phys. Rev. Lett. **18**, 583 (1967).

[5] T. Yanagisawa, H. Matsumoto, and K. Yahagi, Jpn. J. Appl. Phys. **16**, 45 (1997).

[6] A. Sugimura, N. Matsui, Y. Takahashi, H. Sonomura, H. Naito and M. Okuda, Phys. Rev. B **43**, 8272 (1991); H. Naito, M. Okuda, and A. Sugimura Phys. Rev. A **44**, R3434 (1991); H. Naito, K. Yoshida, M. Okuda and A. Sugimura, J. Appl.Phys **73**, 1119 (1993); S. Murakami, H. Naito, M. Okuda and A. Sugimura, J. Appl. Phys **78**, 4533 (1995)

[7] C Colpaert, B. Maximums, and A. De Meyere, Liq. Cryst. **21**, 133 (1996).

[8] Atsushi Sawada, Kazuaki Tarumi, and Shohei Naemura, Jpn. J. Appl. Phys. **38**, 1418 (1999);

[9] Atsushi Sawada, Kazuaki Tarumi, and Shohei Naemura, Jpn. J. Appl. Phys. **38**, 1418 (1999);

[10] Atsushi Sawada and Shohei Naemura, Jpn. J. Appl. Phys. **41**, L195 (2002).

[11] S. Chandrasekhar F.R.S., *LIQUID CRYSTALS*, 2th edition (CAMBRIDGE UNIVERSITY PRESS, 1992), sec. **5**, Chap. 5

[12] Toshio Ohtake, Yauyuki Takamitsu, Kaori Itop-Akita, Kiyoshi Kanie, Masahiro Yoshizawa, Tomohiro Mukai, Hiroyuki Ohno, and Takashi Kato, Macromolecules **33**, 8109 (2000).

[13] Masahiro Funahashi, *Doctoral thesis,* 「液晶性有機半導体の創製と電気伝導に関する研究」 Tokyo Institute of Technology, 1999

Chapter 5

Analysis of Trap Distribution using Time-of-Flight Spectroscopy

5.1 Introduction

In previous chapters (Chaps. 3, 4), we applied the Multiple-Trapping Model (MTM) [1,2] to Time-of-Flight (TOF) photocurrent analysis for studying carrier transport of positive and negative charges in smectic liquid crystalline phases. For applying the model to the biased photocurrents due to positive charge transport in Chapter 3, we assumed the Gaussian distribution for hole trapping and obtained the results which could reproduce well the experimental photocurrents including the effects of applied electric field, temperature and sample length on the current. Here, the MTM with a few trap states only could reproduce the currents for a specific experimental condition, but not enough for other experimental conditions. Other trap states needed to be supposed to explain the whole photocurrents observed at all the conditions. As for negative charge (electron) transport in Chapter 4, we need not assume the trap-state distribution for electrons, as ionic carriers were so dominant that the current due to electrons was not separated clearly. So it may be concluded that the adequate assumption is very important in determining the carrier trap distribution and obtain the results explaining the whole experiments.

In this chapter, we try to extract directly the information of hole-trap distribution from the experimental photocurrent, not based on any assumption about the distribution. This is the reverse procedure of the MTM fitting to the photocurrent described in Chapter 3. The fitting procedure in Chapter 3 was:

(1) Assuming the trap distribution

(2) Constructing MTM based on trap distribution

(3) Deriving the Laplace transformed current from the Laplace transformed Solution of Laplace transformed MTM

(4) Obtaining the inverse Laplace transform and fitting the parameters

Thus, we may extract the trap distribution, at least in principle, by the following (reverse) procedure:

(1) Direct Laplace transformation of the photocurrent

(2) Applying the Laplace transformed MTM to Laplace transformed current

(3) Extracting the function concerning trap distribution

(4) Deriving the trap distribution from the function

This method has been attempted to apply to the photocurrents in organic materials for a couple of decades [3,4]. But the application to organic disordered materials is difficult, because (i) It is quite difficult to separate the contributions from diffusion and trapping process to the observed transient photocurrent. (ii) $\tilde{\psi}(s)$, as explained in 3.2.2, Chap. 3, concerns the function in procedure (3) above and has an integrated form. This integration can not be solved without the trap-distribution function included in the integrand of $\tilde{\psi}(s)$. (iii) Fitting can be well performed for a given condition by using only a few trap states, but not for other conditions: e.g., field-, temperature- and sample length-effects. Here, a possibility may exist that the trap distribution should be replaced by any other distributions. How can we resolve this problem?

Meanwhile, in studying biased photocurrent due to charge transport in SLC, we found that there exits a region where Einstein relation holds in low field region (in Chapter 3). In this region the diffusion constant must be field-independent. So we need not to worry about the problem (i) for SLC in the low field region. In this chapter we will show how we can solve the problem of (ii). We will explain the method how to extract the trap-state distribution from the experimental transient photocurrent. Using the trap-state distribution thus obtained, we may hopefully extend our discussion on other effect such as temperature, as mentioned in (iii).

We measure TOF photocurrent signals for 8-PNP-O12 under applied low field where the Einstein relation holds. In this region, we only observe the charge decay caused by trapping and diffusion of holes where carrier transport occurs in thermal equilibrium.

We will also show the limitation of the method as well, but the limitation coming from the measurement and not from the theory. Lastly, the function mentioned in procedure (3) or an universality curve A(s), which may be used for the trap distribution, will be suggested. It is useful to understand how does the trap distribution contribute to the transient current.

5.2 Analysis of Trap Distribution

5.2.1 Average time between trapping events $\tau(s)$

To derive the equation for trap distribution from the photocurrent, we discussed the method for calculating Laplace transformed current $\tilde{I}(s)$. In Chapter 3 we examined the MTM with carefully considering on boundary conditions at the anode (carrier injection) and cathode (carrier absorbing). We could derive the conventional solution of $\tilde{I}(s)$, i.e.,

$$\frac{\tilde{I}(s)}{\tilde{I}(0)} = \frac{1}{A(s)}(1 - e^{-A(s)}), \tag{5.1}$$

$$A(s) = Ms\tau(s), \tag{5.2}$$

where s denotes Laplace variable and $M = \gamma L/v$ (γ is the total trapping rate, L is the sample length and v is the velocity of transporting carriers, as discussed in detail in Chapter 3). $\tau(s)$ is the average time between successive-trapping events for a carrier. In terms of the detrapping or release rate R

$$\tau(s) = \frac{1}{\gamma} + \frac{1}{s+R} \qquad \text{for one-trap model,} \tag{5.3}$$

$$= \frac{1}{\gamma} + \frac{1-\tilde{\psi}(s)}{s} \qquad \text{for trap-distribution model.} \tag{5.4}$$

The s dependence in Eqs. (5.3) and (5.4) reflects an initial condition that none of the charges are trapped yet, and thus the dwell time for a carrier spent in a trap state increases with time as a consequence of equilibration. For a spread of release rates $R(\varepsilon)$ coming from a distribution of trap energies $\rho(\varepsilon)$, the dependence on s may be expressed in terms of the average distribution of dwell times,

$$\tilde{\psi} = \int_{-\infty}^{\infty} d\varepsilon\, \rho(\varepsilon) \frac{R(\varepsilon)}{s + R(\varepsilon)} \tag{5.5}$$

Inverting Eq. (5.1) we observe that the trapping function

$$A(s) = f\left(\tilde{I}(s) \Big/ \tilde{I}(0) \right) \tag{5.6}$$

depends on the normalized transient $\tilde{I}(s)/\tilde{I}(0)$ through the iterated log function

$$f(x) = \frac{1}{x} + \ln\left(\frac{\frac{1}{x}\ln\left(-\frac{1}{x}\right)}{-\ln\left(\frac{\ln(-\frac{1}{x})}{-\ln\cdots}\right)} \right) \tag{5.7}$$

Assuming convergence of Eq. (5.7), it is therefore possible to work backwards to determine the trap and release function $\tau(s)$ from the current vs. time curve. We should point out that $\tau(s)$ depends only on the trapping and release rates, and is independent of field, at least for low fields [5].

5.2.2 Calculation of the trap distribution $\rho(\varepsilon)$

From the function $\tau(s)$, we can determine the trap energy distribution $\rho(\varepsilon)$ if we assume release rates from all traps of the Arrehnius form

$$R(\varepsilon) = \nu_0 \exp\left(-\frac{\varepsilon}{kT}\right), \tag{5.8}$$

where the energy ε is the trap depth and ν_0 is the attempt frequency. Then,

$$1 - \tilde{\psi} = \int_0^{\infty} d\varepsilon \rho(\varepsilon) \frac{s}{\nu_0 \exp(-\beta\varepsilon) + s}, \tag{5.9}$$

where $\beta = 1/kT$. As we pointed out in previous section 5.1, this integration can not be solved for arbitrary trap distribution function with the same form remaining. Here, we introduce what plays the role of the chemical potential λ, i.e.,

$$s = \nu_0 \exp(-\beta\lambda)\,. \tag{5.10}$$

In such a case, the function

$$1-\tilde{\psi}=\int_0^\infty d\varepsilon\rho(\varepsilon)\frac{1}{\exp(-\beta(\varepsilon-\lambda))+1} \tag{5.11}$$

can be written in the form of a backwards Fermi-Dirac integral through substitution of Eq. (5.10). This integration can be calculated by a convenient way to generate the Sommerfeld corrections to the $T = 0$ (see Fig. 5.1) by the approach followed by Blankenbecler [6,7] for averaging a function of energy over Fermi-Dirac distribution. Integrating Eq. (5.11) by parts gives

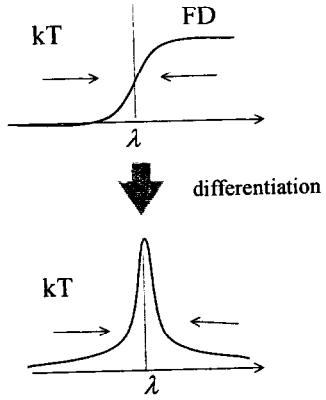

Fig 5.1 Sommerfeld expansion: When we take derivative of Fermi-Dirac (FD) function, it becomes delta-like function. Taking series of differentiations around λ and FD energy as large compared to kT, it converges rapidly.

$$1-\tilde{\psi}(s)=\int_0^\infty d\varepsilon\frac{dQ(\varepsilon)}{d\varepsilon}\frac{1}{\exp(-\beta(\varepsilon-\lambda))+1}$$

$$=\frac{Q(\varepsilon)}{1+\exp(-\beta(\varepsilon-\lambda))}\Bigg|_0^\infty-\int_0^\infty d\varepsilon Q(\varepsilon)\frac{\beta\exp(-\beta(\varepsilon-\lambda))}{\left[1+\exp(-\beta(\varepsilon-\lambda))\right]^2}, \tag{5.12}$$

where we have introduced the cumulative density of states

$$Q(\varepsilon)=\int_0^\varepsilon d\varepsilon'\rho(\varepsilon'). \tag{5.13}$$

In Eq. (5.12) the first term is equal to 1, because $Q(\varepsilon)$ is cumulative $\rho(\varepsilon)$ which is normalized to 1 ($Q(\infty)$ =1). The integrand except for $Q(\varepsilon)$ in Eq. (5.12) is normalized with respect to ε and localized exponentially at $\varepsilon = 1$ with a width of the order of kT (see Fig. 5.1). Therefore, for a density of states sufficiently smooth on the scale of kT, we can approximate Eq. (5.12) as

$$\tilde{\psi}(s)\approx Q(\lambda)\big|_{\lambda=-kT\ln(s/\nu_0)} \tag{5.14}$$

providing a convenient relationship between the density of states and the distribution of dwell times. This has been noted, for example, in reference [3]. Essentially we are replacing the Fermi-Dirac distribution function by a step function, so that its derivative goes to a

delta function. First, the formal definition of Q = 0 when $\varepsilon<0$ allows us to extend the lower limit of the integration to $-\infty$. With changing the variable of integration into $x = \varepsilon - \lambda$, we can write

$$1-\tilde{\psi}(s)=1-\beta\int_{-\infty}^{\infty}dxQ(x+\lambda)\frac{e^{-\beta x}}{1+e^{-\beta x}}$$

$$=1-\beta\int_{-\infty}^{\infty}dx\frac{e^{-\beta x}}{(1+e^{-\beta x})^2}e^{\beta x\hat{\delta}}Q(\lambda) \tag{5.15}$$

where $Q(\lambda)$ in the second line is operated on by the displacement operator $\exp(\beta x\hat{\delta})$. Here, $\hat{\delta}=\beta^{-1}\partial/\partial\lambda$, then $Q(x+\lambda)$ can be expanded around $Q(\lambda)$,

$$Q(z+\lambda)=Q(\lambda)+x\beta\hat{\delta}Q(\lambda)+\frac{(x\beta\hat{\delta})^2}{2!}Q(\lambda)+\cdots\cdots$$

$$=e^{\beta x\hat{\delta}}Q(\lambda) \tag{5.16}$$

There is considerable simplification of Eq. (5.14) with $\eta=\exp(\beta x)$

$$1-\tilde{\psi}(s)=1-\int_{0}^{\infty}d\eta\frac{\eta^{\hat{\delta}}}{(1+\eta)^2}Q(\lambda). \tag{5.17}$$

The evaluation of the integral over η can be done as a contour and the calculation of residues. Consider

$$\oint dz\frac{z^{\hat{\delta}}}{(1+z)^2}=2\pi i a_{-1} \tag{5.18}$$

A pole of order 2 exists at $z=-1$ with resulting in the residue $a_{-1}=\hat{\delta}e^{-\pi i\hat{\delta}}$, and a branch point exists at z=0. We use contour integral shown in Fig. 5.2,

$$\int_{AB}+\int_{BC}+\int_{CD}+\int_{DA}$$

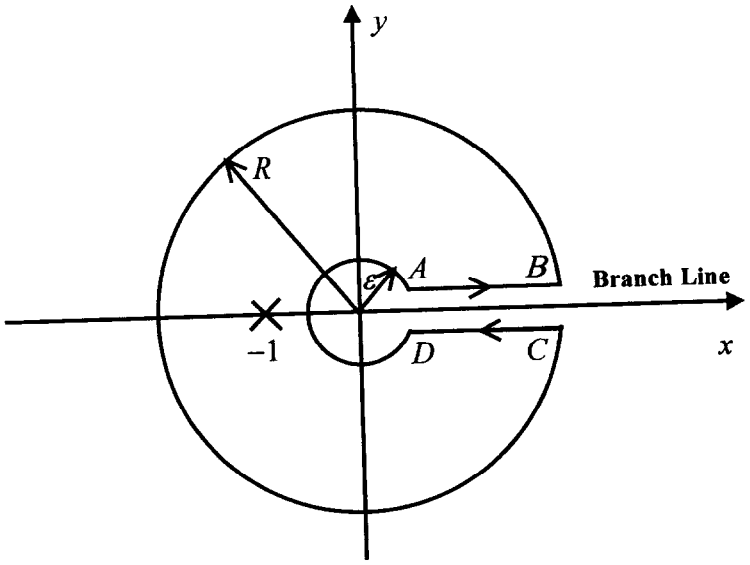

Fig. 5.2 :The contour integral used to evaluate $\int_0^\infty d\eta \eta^{-\hat{\delta}}/(\eta+1)^2$

$$= \int_\varepsilon^R d\eta \frac{\eta^{\hat{\delta}}}{(1+\eta)^2} + \int_0^{2\pi} d\theta \frac{iRe^{i\theta}(Re^{i\theta})^{\hat{\delta}}}{(1+Re^{i\theta})^2} + \int_R^\varepsilon d\eta \frac{(\eta e^{2\pi i})^{\hat{\delta}}}{(1+\eta e^{2\pi i})^2} + \int_{2\pi}^0 d\theta \frac{i\varepsilon e^{i\theta}(\varepsilon e^{i\theta})^{\hat{\delta}}}{(\varepsilon e^{i\theta}+1)^2}$$

$$= 2\pi i\hat{\delta} e^{-\pi i\hat{\delta}} \tag{5.19}$$

In the limit of $R \to \infty$ and $\varepsilon \to 0$, the second and fourth integrals vanish. Then

$$(1-e^{-2\pi i\hat{\delta}})\int_0^\infty d\eta \frac{\eta^{\hat{\delta}}}{(1+\eta)^2} = 2\pi i\hat{\delta} e^{-\pi i\hat{\delta}} \tag{5.20}$$

or

$$\int_0^\infty d\eta \frac{\eta^{\hat{\delta}}}{(1+\eta)^2} = \frac{\pi\hat{\delta}}{\sin\pi\hat{\delta}}. \tag{5.21}$$

Thus the remaining integral in Eq. (5.16) over ε can be done as a contour, leaving

$$1-\tilde{\psi}(s) = 1-\frac{\pi\hat{\delta}}{\sin\pi\hat{\delta}} Q(\lambda)\Big|_{\lambda=-kT\ln(s/\nu_0)} \tag{5.22}$$

Multiplying both sides of Eq. (5.21) by $\beta/\pi \sin\pi\hat{\delta}$ from the left gives

$$\beta\hat{\delta} Q(\lambda) = \frac{\beta}{\pi}\sin\pi\hat{\delta}\tilde{\psi}(s) \tag{5.23}$$

The density of states, however, $\rho(\varepsilon) = \partial Q(\lambda)/\partial\lambda = \beta\hat{\delta}\, Q(\lambda)$, so we are left with an exact expression for the density of states in terms of the average dwell-time distribution,

$$\rho(\varepsilon) = \frac{\beta}{\pi}\sin\pi\hat{\delta}\tilde{\psi}(s)\Big|_{s=\nu_0\exp(-\beta\lambda)}. \tag{5.24}$$

Thus we see that a simple operation on $\tilde{\psi}(s)$ will give the density of trap states. The first term in the expansion of $\sin\pi\hat{\delta}$ already gives the approximation of equation Eq. (5.14).

Unfortunately, the quantity which is experimentally accessible is not $\tilde{\psi}(s)$ but rather the trapping function, Eq. (5.2), i.e.

$$A(s) = M\left(s\gamma^{-1} + 1 - \tilde{\psi}(s)\right) \tag{5.25}$$

having an unknown prefactor M and the trapping rate γ^{-1}, and so it would seem that to determine the density of trap states we will have to find a way to extract $\tilde{\psi}(s)$ from this composite function. We should consider, however, the operation

$$\frac{\beta}{\pi}\sin\pi\hat{\delta}\, A(s) = M\frac{\beta}{\pi\gamma}\sin\pi\hat{\delta}\, s - M\frac{\beta}{\pi}\sin\pi\hat{\delta}\tilde{\psi} \tag{5.26}$$

The operation causes the additional term which is linear in s in $A(s)$ to vanish

$$\sin\pi\hat{\delta}\, s = \sin\left(\pi\beta^{-1}\frac{\partial}{\partial\lambda}\right)\nu_0 e^{-\beta\lambda} = -\nu_0\sin\pi = 0. \tag{5.27}$$

It therefore follows, by introducing Eqs. (5.24) and (5.27) into (5.26), that operation on A(s)

$$-\frac{\beta}{\pi}\sin\pi\hat{\delta}\, A(s) = M\rho(\varepsilon) \tag{5.28}$$

gives the density of states up to a simple constant of proportionality. For numerical calculations, it is convenient to represent the operator $\hat{\delta}$ in terms of s, such that

$$\hat{\delta} = \frac{1}{\beta}\frac{\partial}{\partial\lambda} = -\frac{\partial}{\ln s}. \tag{5.29}$$

Then

$$\rho(\varepsilon) = \frac{1}{\mathrm{M}}\frac{\beta}{\pi}\sin\left(\pi\frac{\partial}{\partial\ln s}\right)A(s)\Big|_{s=\nu_0 e^{-\beta\varepsilon}}. \tag{5.30}$$

The unknown factor M can be determined by requiring that ρ be normalized.

Although this procedure determines the functional form of the density of trap states, it determines only relative energies rather than absolute energies, because the attempt frequency ν_0 is undetermined. For example, we can always introduce a new frequency $\nu_0' = \nu_0 \exp(\beta\varepsilon_0)$, where ε_0 is an arbitrary energy. Since the density of states is to be evaluated by setting $s = \nu_0 \exp(\beta\varepsilon)$, changing ν_0 to ν_0' is equivalent to shifting the origin of the density of states by ε_0. Therefore, the only way to estimate the absolute location of the density is to perform experiments at different temperatures and find the activation energy. Once this is specified, then ν_0 can be estimated. Without this information, however, the best we can do is to place a lower bound on ν_0 by requiring that the trap energies be positive.

5.2.3 Calculation of the trap distribution in the case of MTM with D ≠ 0

In this section we extend the analytical method of trap-distribution extraction explained in previous section to cases in which diffusion process is not ignorable. In Chapter 3 we also solved the MTM with $D \neq 0$, as the same way as for the MTM with $D = 0$, by carefully reflecting of boundary conditions at the anode (carrier injection) and cathode (carrier absorption). We could derive the conventional solution of $\tilde{I}(s)$, i.e.,

$$\frac{\tilde{I}(s)}{\tilde{I}(0)} = \frac{D}{vL}\left(C_1 e^{-(1+\kappa)vd/2D} + C_2 + \frac{1}{\kappa}\right) + \frac{2DC_1}{vL(1+\kappa)}\left(1 - e^{-(1+\kappa)vd/2D}\right) - \frac{2D(C_2+\kappa^{-1})}{vL(1-\kappa)}\left(1 - e^{(1-\kappa)vd/2D}\right) \tag{5.31}$$

where

$$\kappa = \sqrt{1 + 4Ds\gamma\tau/v^2} = \sqrt{1 + 4DA(s)/vL} \tag{5.32}$$

$$C_1 = -\frac{2e^{vL/2D}}{\kappa + 1 + (\kappa - 1)e^{-\kappa vL/D}} \tag{5.33}$$

$$C_2 = -\frac{(\kappa - 1)(1 - e^{-\kappa vL/D})}{\kappa\left[\kappa + 1 + (\kappa - 1)e^{-\kappa vL/D}\right]} \tag{5.34}$$

Then we may conclude that the normalized Laplace transformed current (5.31) will be a function of only two parameters, κ and $vd/2D$, i.e.,

$$\begin{aligned}\frac{\tilde{I}(s)}{\tilde{I}(0)} &= g\left(\frac{vL}{2D};\kappa\right) \\ &= g\left(\frac{vL}{2D};\sqrt{1+\frac{4DA(s)}{vL}}\right) \\ &= g\left(\frac{1}{2}\beta eV;\frac{4A(s)}{\beta eV}\right)\end{aligned} \tag{5.35}$$

We have simplified the expression of the third line by using the Einstein relation. After D is omitted by using Einstein relation, we can numerically invert g to obtain $A(s)$ from the $\tilde{I}(s)$ vs s curves using Newton's method. Then we may derive the $A(s)$ vs. s curves for different voltages. As in the same manner for D = 0 case, we can derive trap-density distribution from A(s) by using Eq. (5.30)

5.3 Deriving Trap Distribution from Experimental-TOF Photocurrent

This provides a test for the applicability of the MTM through a procedure which we outline as follows. Measurements on a single sample at a single temperature T yield a family of normalized $I(t)$(or $I(t)/\tilde{I}(0) = I(t)/(\text{total charge})$) vs. t traces, parametric in applied field. A corresponding family of $\tilde{I}(s)/\tilde{I}(0)$ vs. s curves, parametric in E can then be determined by performing a numerical Laplace transform of each trace. Substitution into Eq. (5.7) for $D = 0$ or numerical calculation of inverted g using Newton's method for $D \neq 0$, gives a family of $A(s)$ vs. s curves. While the factors $M=\gamma L / v$ are not determined explicitly, for linear response, M is inversely proportional to the field. If the multiple-trapping model is applicable, it should be possible, therefore, to obtain a single universal AV vs. s curve by their respective voltages, because $AV=(MV)s\tau$, then, MV is not field dependent. And we derive the figuration of $\rho(\varepsilon)$ from collection Eq. (5.30),

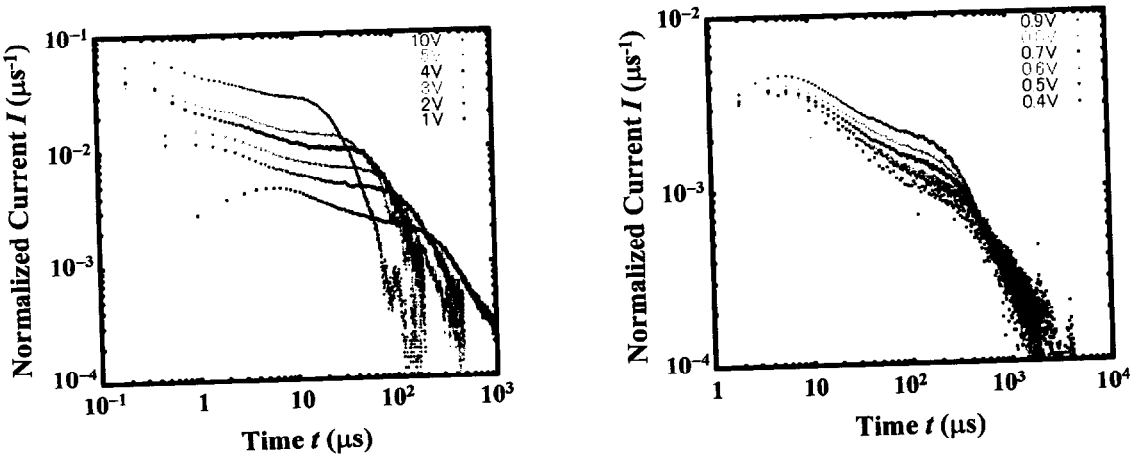

Fig. 5.3 :Double-log plots of photocurrents in SmB of 8-PNP-O12 for each applied voltage

$$\rho(\varepsilon)=\frac{\beta v}{\pi\gamma L}\left[\left(\pi\frac{\partial}{\partial\ln s}\right)-\frac{1}{3!}\left(\pi\frac{\partial}{\partial\ln s}\right)^{3}+\cdots\right]A(s)\Big|_{s=\nu_0 e^{-\beta\varepsilon}} \tag{5.36}$$

The present method will be applied to experimental transient photocurrents. The currents were measured by conventional TOF set-up explained in Chapter 2. The sample is 8-PNP-O12 sandwiched by Al electrodes. The cell thickness is 5 μm. A measurement range of

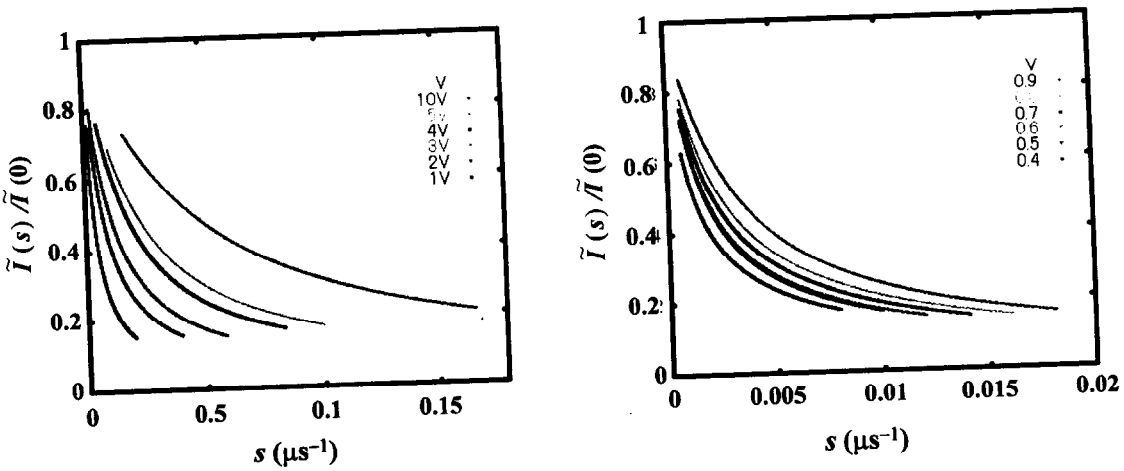

Fig. 5.4 :Laplace transformed photocurrents in SmB of 8-PNP-O12 for each applied voltage

applied voltage $V = 0.4\text{V} \sim 10\text{V}$. Temperature is maintained at $T = 80°\text{C}$ (SmB) because we cannot see temperature dependence for such a narrow temperature range of SmB phase. Photocurrents are dealt with computer for Laplace transform and Newton method to extract $A(s)$, then $\rho(\varepsilon)$.

In Fig. 5.3 is shown the corresponding family of experimentally normalized current

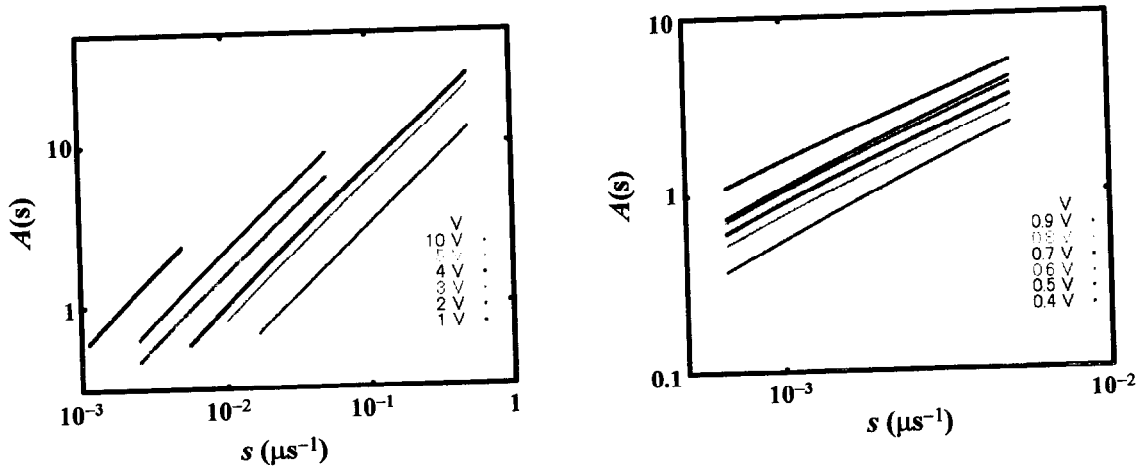

Fig. 5.6:Double-log plots of A(s) vs. s in SmB of 8-PNP-O12 for each applied voltage with assumption D=0

$I(t)/\tilde{I}(0)$ vs. t curves. Evaluated Laplace transformed currents $\tilde{I}(s)/\tilde{I}(0)$ vs. s curves are shown in Fig. 5.4. The lower and upper limits of s should be in the order of the reciprocals of the maximum and minimum times in the $I(t)$ vs. t curves. The maximum value of s is ultimately set by the time interval between data points in the current-time curve without considering RC problem. However, we did not take the minimum time of the current signal but the minimum time in which the signal delay due to RC problem did not affect the photocurrents. We took the order of reciprocals of the maximum time for the minimum s. The minimum value of s is determined by the maximum time on the current-time curve. Therefore, we only have reliable information concerning the shape of $\rho(\varepsilon)$ between the minimum and maximum energy, respectively, i.e.,

$$\varepsilon_{\min} = -kT\ln(s_{\min}/\nu_0) \tag{5.37}$$

$$\varepsilon_{max} = -kT\ln(s_{max}/\nu_0) \tag{5.38}$$

If we attempt to go far in either direction, the shape becomes unreliable. It is easy to determine the range of ε in which the data should be reliable,

$$\Delta\varepsilon = \varepsilon_{max} - \varepsilon_{min} = -kt\ln(s_{max}/s_{min}).$$

First we applied the method to the case with $D = 0$ based on Eq. (5.6) to obtain the $A(s)$ vs. s curves as shown in Fig. 5.5. Since M should be inversely proportional to the field, A(s) is inversely proportional to applied voltage V. Thus, AV must be constant for each voltage. Fig 5.7-(a) shows the AV vs. s with assumption of $D = 0$. These curves form a slightly progression to higher AV for higher voltage, which shows that they are not universal. This lack of universality shows that the MTM with $D = 0$ is not entirely applicable. This may be due to the fact that the multiple trapping model neglects the contribution of diffusion to the broadening of the transients. The experiment was performed at $T = 350$K, so that at the low voltage end, ca. 1 V, $\sqrt{2kT/eV} = 1/5$. While this is certainly smaller than 1 it is not zero, and, after all, the important question for the validity of the MTM is whether the diffusion broadening can be neglected as compared to the broadening due to trapping. In view of the failure of the universality of AV in the case with D=0, we therefore go to the case including the diffusion process.

Figure 5.7-(b) shows the evaluated $A(s)$ vs. s by using computer aided Newton's method with concerning diffusion. These curves were improved better than those in Fig. 5.7-(b). We can hardly see the progression to higher AV for higher voltage. Although these curves still have difference from each other, this difference is not systematic. We think this difference comes from error in measurement of the voltage. In measurement, it was difficult to adjust the voltage in the order 0.01V in our setup. Moreover, the internal voltage may be different from external applied voltage in the order 0.01V, because we cannot control the resistance at contact surface between Al electrode and organic sample. Thus we concluded that the curves in Fig. 5.7-(b) are identical with each other within the error of measurement and that AV curve is universal. This is very important because AV curves, where we think no difference of trap condition exists for each field, show no difference from each field

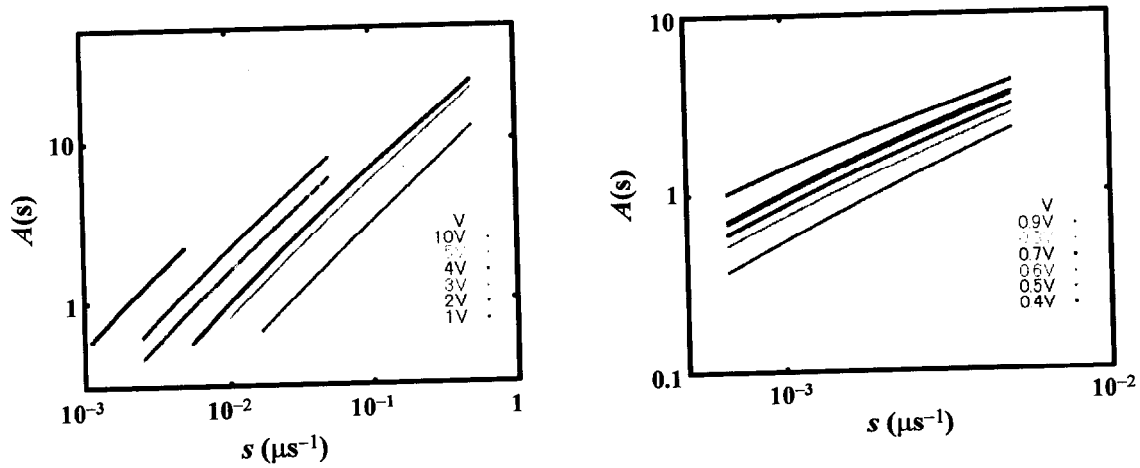

Fig. 5.5:Double-log plots of A(s) vs. s in SmB of 8-PNP-O12 for each applied voltage with assumption D=0

Finally we derive the trap distribution $\rho(\varepsilon)$ based on Eq. (5.36) using $A(s)$ derived with the method $D \neq 0$. As stated before, unfortunately, we do not know the attempt frequency ν_0 nor $M(V)$. Here we set $\nu_0 = 5\times10^4\ s^{-1}$, arbitrarily and we set

$$M = V_0 / V \tag{5.39}$$

where V is applied voltage and V_0=100 V, arbitrarily. This M value is improved after $\rho(\varepsilon)$ is derived by normalization. We try to calculate $\rho(\varepsilon)$ for each field by using computer. But most of the signal of evaluated $\rho(\varepsilon)$ is hidden in noise and is monotonically increases with

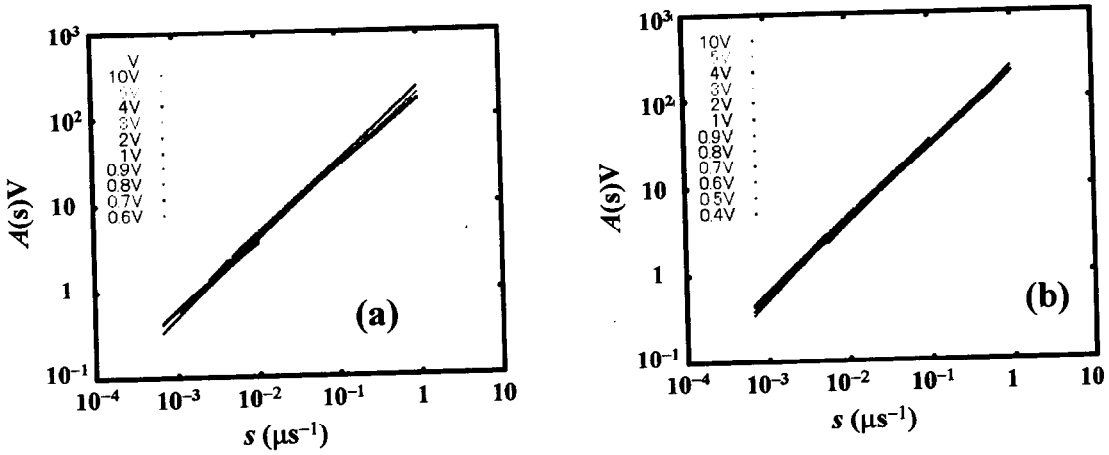

Fig. 5.7:Double-log plots of A(s)V vs. s in SmB of 8-PNP-O12 for each applied voltage : (a)D=0, (b)D≠0

decreasing ε even if we take higher order of the series. These depend on sampling number

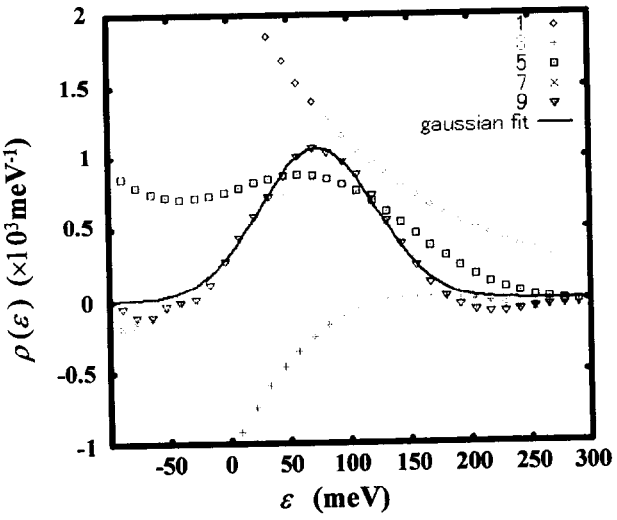

Fig. 5.8 Trap distribution: For SmB of 8-PNP-O12 with applied voltage of 0.7V.

of the data. Furthermore, s range is too narrow to configure whole $\rho(\varepsilon)$. So, we try again to take s range to allow large s corresponding to small t in the range where there is a possibility to affect delay of RC. Then, Fig. 5.8 shows the derived $\rho(\varepsilon)$ for the current data V = 0.7 V. Numbers correspond to the order in Eq. (5.36). As the order of the series increases, calculated $\rho(\varepsilon)$ is becoming close to Gausssian function. The line in Fig. 5.8 shows the fitting of Gaussian function to the series of $\rho(\varepsilon)$ having the order 9. Evaluated Gaussian function is

$$g(\varepsilon) = 1.07\times10^{-3}\exp\left(-\frac{(\varepsilon-74)^2}{2\times48^2}\right). \tag{5.40}$$

Normalization so as to $\int_0^\infty d\varepsilon\, g(\varepsilon) = 1$ gives:

$$g(\varepsilon) = 1.48\times10^{-2}\exp\left(-\frac{(\varepsilon-74)^2}{2\times48^2}\right). \tag{5.41}$$

and we may conclude that our material, SLC, has a trap distribution of the Gaussian type. Therefore, by using one of the experimental results of TOF-transient photocurrents in SmB of 8-PNP-O12, we analytically derived the trap distribution of the Gaussian type with

standard deviation σ= 48 meV. One may also conclude that the center of the Gaussian distribution is 74meV lower from the transport level, but this means nothing because we arbitrarily assume $\nu_0 = 5\times10^4$ s^{-1}. So, if the correct value of ν_0 was found, the distribution slides by kT ln ((correct value of ν_0)/(arbitrarily assumed value of ν_0)). The important thing we can say is that, without assuming the Gaussian type for trap distribution, we have derived the Gaussian distribution as the result of direct analysis of TOF-transient current.

5.4 A New Method for Fitting based on MTM

In this section we suggest a new method for fitting based on MTM. In previous section, we tried to extract the trap distribution from TOF-transient photocurrents. We could scarcely extract the trap distribution from a photocurrent signal. Most of the photocurrents with noisy signal and narrow-time range can not give the trap distribution. In Fig. 5.7-(b), on the other hand, we found that $A(s)V$ curve including all the information of trap distribution showed no field dependence. This is consistent with the idea that the trap distribution should not changed directly by the field or temperature. Here, a new idea arises that if we do not fit the current-curves but try to fit the A(s)V-curves for a wide range of field, the $A(s)V$-fitting may work better than the current-fitting. This method has another merit from the numerical side. For current-fitting, we must calculate the inverse Laplace transform and also employ the least square method at a time. But we need not calculate the inverse Laplace transform in the new method. $A(s)V$-curves are fitted directly by using the least square method.

5.4.1 Formula of $A(s)$ for various trap distribution

To fit $A(s)$ we must derive the formula of $A(s)$ for each trap distribution. These calculations were more often than not complicated and their calculations are vexatious complex. But now we have Eq. (5.22), we can discuss systematically for each trap distribution.

(i) One trap-state

One trap-state can be denoted as delta function, $\delta(\varepsilon-\varepsilon_0)$, where ε_0 is energy measured with respect to transport-state. Delta function is denoted as

$$\delta(\varepsilon-\varepsilon_0)=\frac{1}{2\pi}\int_{-\infty}^{\infty}dke^{ik(\varepsilon-\varepsilon_0)}, \tag{5.42}$$

in Fourier transform. Then, cumulative function is

$$\begin{aligned} Q(\lambda) &= \int_0^{\lambda} d\varepsilon\delta(\varepsilon-\varepsilon_0) \\ &= \frac{1}{2\pi}\int_{-\infty}^{\infty}dk\frac{e^{ik(\lambda-\varepsilon_0)}+e^{-ik\varepsilon_0}}{ik} \end{aligned} \tag{5.43}$$

By inserting Eq. (5.43) into (5.22),

$$\begin{aligned} 1-\tilde{\psi} &= 1-\frac{1}{2\pi i}\int_{-\infty}^{\infty}\frac{dk}{k}\frac{\pi(ik/\beta)}{\sin\pi(ik/\beta)}\left[e^{ik(\lambda-\varepsilon_0)}-e^{-ik\varepsilon_0}\right] \\ &= 1-\frac{1}{1+e^{-\beta(\lambda-\varepsilon_0)}}. \end{aligned} \tag{5.44}$$

We do not present here the details of calculation including complex integration to derive the second equation above. Equation (5.44) is rewritten by using definition of λ, Eq. (5.10), with s in stead of λ,

$$\begin{aligned} A(s) &= Ms\left[\frac{1}{\gamma}+\frac{1}{s}\left(1-\frac{1}{1+(s/\nu_0)e^{\beta\varepsilon_0}}\right)\right] \\ &= Ms\left[\frac{1}{\gamma}+\frac{1}{s}\left(1-\frac{1}{1+s/R}\right)\right] \\ &= Ms\left(\frac{1}{\gamma}+\frac{1}{R+s}\right), \end{aligned} \tag{5.45}$$

where $R = \nu_0 e^{-\beta\varepsilon_0}$. This result is consistent with the results of Chapter 3.

(ii) Gaussian trap-state

Deriving Gaussian trap-state from $A(s)$ is difficult, but we can systematically try along the same procedure of (i). Gaussian distribution is denoted as

$$\rho(\varepsilon)=\frac{A}{\sqrt{2\pi\sigma^2}}\exp\left[-\frac{(\varepsilon-\varepsilon_0)^2}{2\sigma^2}\right]. \tag{5.46}$$

And the cumulative function,

$$Q(\lambda) = \frac{A}{\sqrt{2\pi\sigma^2}} \int_0^{\lambda} d\varepsilon \exp\left[-\frac{(\varepsilon-\varepsilon_0)^2}{2\sigma^2}\right]$$

$$= \frac{A}{2}\left(\mathrm{Erf}\left(\frac{\lambda-\varepsilon_0}{\sqrt{2}\sigma}\right) + \mathrm{Erf}\left(\frac{\varepsilon_0}{\sqrt{2}\sigma}\right)\right). \tag{5.47}$$

A is defined as normalization constant, i.e.,

$$Q(\infty) = \frac{A}{2}\left(1 + \mathrm{Erf}\left(\frac{\varepsilon_0}{\sqrt{2}\sigma}\right)\right) = 1. \tag{5.48}$$

Then

$$A = \frac{2}{\left[1 + \mathrm{Erf}(\varepsilon_0/\sqrt{2}\sigma)\right]}. \tag{5.49}$$

By inserting Eq. (5.47) into (5.22) and taking series

$$1-\tilde{\psi} = 1 - \frac{A}{2}\left(1 - \frac{\pi^2}{3!}\hat{\delta}^2 + \frac{\pi^4}{5!}\hat{\delta}^4 - \cdots\right)\left[\mathrm{Erf}\left(\frac{\lambda-\varepsilon_0}{\sqrt{2}\sigma}\right) + \mathrm{Erf}\left(\frac{\varepsilon_0}{\sqrt{2}\sigma}\right)\right] \tag{5.50}$$

Thus we can derive $A(s)$ on the basis of Eq. (5.50):

$$A(s)V = \frac{L^2}{\mu}\left(s + \gamma(1-\tilde{\psi})\right) \tag{5.51}$$

We also used this formula in Chapter 3.

5.4.2 $A(s)V$-fitting

Based on Eq. (5.50) and taking the 4th order, $A(s)V$ curves in Fig. 7 were fitted. This fitting is shown in Fig. 5.9. Derived parameters are shown in TABLE 5.1. Then we can reproduce the photocurrent for each field from the same $A(s)V$. The results are shown in Fig. 5.10. Herewith, it is confirmed that the new method of fitting is to be useful. We think the Gaussian trap distribution having the parameters shown in TABLE 5.1 is most reliable to explain the features of transient photocurrent. Of course we can obtain the parameters of

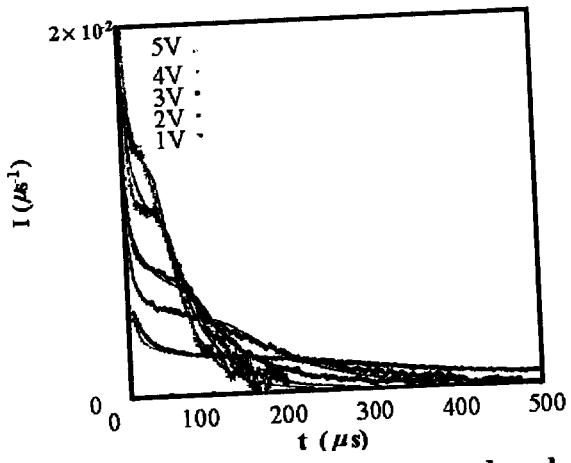

Fig. 5.9 Photocurrents compared with reproduced currents based on the parameters derived by $A(s)V$-fitting of Gaussian trap in SmB of 8-PNP-O12.

Gaussian trap distribution by other methods: Direct-photocurrent fitting explained in Chapter 3, and the fitting for evaluated-trap distribution explained in section 5.3. But these can be applied only for a specific field region, while the trap distribution, we believe, does not change with varying the field. The present method for fitting is applicable for all field region without loosing the universality.

TABLE 5.1 Extracted parameters from $AV(s)$-fitting

μ (cm^2 / Vs)	γ (μs^{-1})	ε_0 (meV)	σ (meV)	ν_0 (μs^{-1})
6.3×10^{-4}	0.54	3.2×10^{-4}	51	2.8×10^{6}

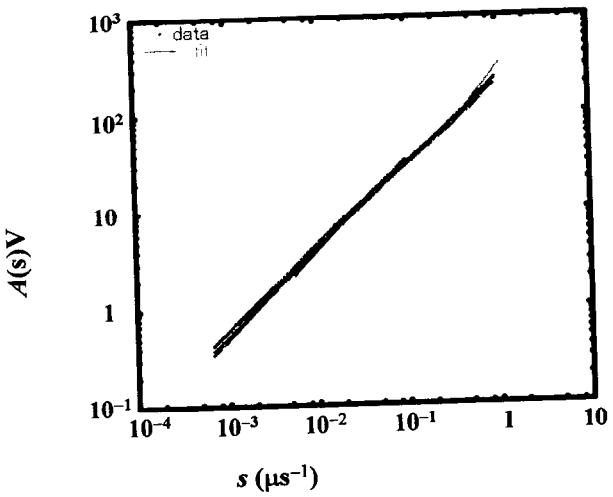

Fig. 5.9: $A(s)V$ fitting of Gaussian trap in SmB of 8-PNP-O12:data shows AV vs. s for various voltage 0.4V~10V

5.5 Conclusion

We derived a new method for extracting trap distribution from TOF-transient photocurrent. For deriving the method, principally useful to extract the distribution, we clarified three problems. First, our material, SLC, provides a field-independent diffusion process in consistent with Einstein relation at low fields. Thus, by introducing Einstein relation we can distinguish the diffusion effect from trapping effect in photocurrent. Second, we solved the integration of $1-\tilde{\psi}$ corresponding to average-dwell time for arbitrary-trap distribution by using Blankenbecler' way to take Sommerfeld corrections. Finally, a problem may be addressed that another different trap distribution may also well explain the current signal. This problem may correspond to that v_0 is not to be determined from a single current signal. We only derive the shape of trap distribution without knowing how the trap distribution is apart from the transport state. This problem may be solved by applying to current signals at varying temperatures. Unfortunately our material, SLC, is stable for a very narrow temperature range and, thus, we cannot study temperature dependence.

As a practical matter, however, the range of time measurement may be the limitation for the energy range of extracted trap distribution. Furthermore, in deriving trap distribution using high-order derivative functions, noises can often be enhanced, and so we are forced to use only a set of data to obtain a Gaussian trap distribution.

On the other hand we found a universal curve of $A(s)V$ which retains all the information on trap. Thus we suggest a new method for fitting to apply the universal curve, $A(s)V$. This method can be applied to photocurrents for various field ranges. The Gaussian trap distribution thus derived is most reliable among other methods. Finally we conclude that our material has a Gaussian trap distribution with the parameters denoted in TABLE 5.1.

References

[1] J. Noolandi, Phys.Rev. B **16**, 4466 (1977).

[2] J. Noolandi, Phys. Rev. B **16**, 4474 (1977).

[3] E. Muller, D. Haarer, and H. Scher, Phys. Rev. B **35**, 1275 (1987).

[4] H. Naitou and M. Okuda, J. Appl Pys **77**, 3541 (1995).

[5] We should point out that the well-known universality of Scher and Montroll requires, in addition, the property that $\tau(s)$ may be well-represented by a single power law for a broad distribution of traps.

[6] R. Blakenbecler, Am. J. Phys. **25**, 279 (1957).

[7] W. A. Barker, J. Math. Phys. **27**, 302 (1986).

Chapter 6

Microscopic Analysis Using Gaussian Disorder Model

6.1 Introduction

In the previous chapters we have analyzed the TOF photocurrent by using multiple-trapping model (MTM) .. We are now in the stage of good understanding of carrier transport features in smectic liquid crystals (SLC), i.e. field and temperature dependence of the mobility, which has not been clarified before. We now know how to analyze the TOF photocurrent result for the new materials with rather new electronic transport features. We found out that SLC is among the materials having electronic transport behavior for which the Einstein relation holds at low electric fields. No organic materials except for crystalline phases have been studied in a regime in which the mobility is consistent with the Einstein relation. The multiple trapping model is based on the idea that charges hop between nearly isoenergetic molecules, and occasionally they become trapped in defect molecules which are at a lower energy than their neighbors. For many years, the conventional model of photo injected charge transport in disordered organic conductors, in particular the molecularly doped polymers, has been one in which charges hop among molecules with different energies coming from a Gaussian distribution. In the GDM it is difficult to separate the low energy sites from the high energy sites, and to label some of them as traps and others of them as free. Nevertheless, it is quite possible that the predictions of the GDM are not incompatible with the predictions of the MTM, and that the MTM may serve as a handy approximation for the GDM To investigate this, in this chapter we will assume that the Gaussian Disorder Model (GDM) [1] describes electronic transport in the Smectic

Liquid Crystals (SLC), and develop a two-dimensional GDM to investigate carrier transport features in SLC. We will use Monte Carlo simulations to compare the predictions of the GDM with the experimental results.

As has been discussed in Chapter 2, the GDM explains some of the electronic transport properties of amorphous organic solids very well. These materials often show the mobility with strong-field and strong-temperature dependence. Off-diagonal disorder, due to Gaussian type deviation with respect to position and orientation from the simulated 3-D periodic lattice points, comes from the disorder of the position and orientation of each molecules in amorphous organic material. Diagonal disorder, due to Gaussian type deviation with respect to energetic level, comes from energetic disorder of the HOMO (for holes) or LUMO (for electrons) levels.

Unfortunately, however, there is no direct and easy way to find the origin of the off-diagonal disorder because we can not measure the inter- and intra-molecular contributions to the transfer activation energy. The optical spectra of molecular solids reflect excitonic transitions in contrast to valence-conduction band transitions in inorganic semiconductors. So, the direct probing by absorption spectroscopy can hardly give information about the density of states (DOS) function for charge transport state. The origin of the disorder may be ascribed to the superposition of ubiquitous contribution arising from Van der Waals interactions between a charge carrier and the electrically polarizable random medium [2,3,4] and the contribution of the summation of electrostatic potential caused by randomly distributed permanent dipoles [5,6]. The van der Waals interaction contribution to the energetic disorder is practically negligible compared to the charge-dipole interactions. This permanent dipole contribution may be related to the Poole-Frenkel like field dependence, i.e.,

$$\mu \propto \exp\left(\gamma\sqrt{E}\right) \tag{6.1}$$

where E is an applied electric field and γ a coefficient depending on temperature. This relation (6.1) cannot be derived from a simple GDM. GDM alone would lead to the field-dependent mobility in high-field region ($>10^5 cm^2/Vs$). On introducing the correlation of the electrostatic potentials of the permanent dipoles, the relation expressed by eq. (6.1) appears. This was first examined by Garstein *et al* for a simplified case [7] and, for one-dimensional

case, was analytically solved by Dunlap *et al* [8]. We call this model the Correlated Disorder Model (CDM). In experiments, the Poole-Frenkel field dependence of the mobility usually appears in amorphous organic materials in a wide range of field [9]. This behavior was confirmed with the CDM, analytically for one-dimensional case, and numerically for three-dimensional case [10].

In this Chapter, as mentioned above, we apply the two-dimensional disorder model to investigate the carrier transport properties in SLC with the aid of Monte Carlo simulations. We think that this model can be described by the GDM, for the condensed state has still the disorder relevant to SLC. The molecular alignment is thought to have no long distance order. The alignment often shifts and, furthermore, the molecules rotate in SmA and SmB and flap in SmE phases [11]. Although it has been suggested by others [13] that a band-transport picture is appropriate due to the structure in SLC, we suggest that this is not the case. SLC is quite different from the molecular crystals often encountered and, moreover, the mobility depends neither on electric field nor on temperature. So it is likely that disorder formalism pertinent to SLC may be quite different from the formalism for the amorphous organic solids. As will be shown, however, a two-dimensional disorder model with a small Gaussian width of 50~60 meV can explain many of the carrier transport properties in the smectic mesophase, such as field- and temperature-independent mobility. Also a field- and temperature-dependent mobility is predicted in the smectic mesophase by the same model with a large Gaussian width of 100~120meV which is comparable to amorphous material.

6.2 Two-dimensional Disorder Model

We are concerned here with a system where the carriers hop among the molecules in the smectic mesophase. All the molecules sit in the layers with thermal fluctuation and the molecular alignment in the layers determines each mesophase. The inter-layer molecular distance of about 30~40 Å is much greater than the intra-layer distance of 3~4Å in 8-PNP-

O12 and 8-PNP-O4 [12]. Therefore undoubtedly, the charge carrier transport exclusively takes place within the smectic layer. This has been confirmed from experiments using diluted smectic liquid crystals [13]. Therefore, our model for carrier transport in the smectic mesophases will be a GDM where the motion of the carriers is restricted to hopping in a two-dimensional (2D) disordered system.

A different molecular alignment makes different hopping paths available according to the configuration in the smectic mesophases such as SmA, SmB, and SmE. We make the site configuration in each smectic layer as follows: i) In SmA, the molecular alignment is random in the layer, ii) In SmB, each site is aligned in hexagonal lattice points, and iii) In SmE, each site is aligned in rectangular lattice points.

We incorporated the off-diagonal disorder for the SmA phasein a manner similar to that introduced by Pautmeier *et al* [14,15]. We assumed that the inter-site distance is subject to local variation while that the coupling among the transport molecules having mutually different orientation is not important in liquid crystalline phases. In the model, each site is assigned to a unique point on a square lattice . The spatial disorder is then represented heuristically by varying the distances which enter the hopping matrix elements according to a Gaussian distribution with deviation σ_r. The amount of disorder is quantified by the off-diagonal disorder parameter $\Sigma=\sqrt{2}\ \sigma_r/\alpha$, where α is the decay length of the the wave function in the localized states. This parameter measures the deviation from the distance distribution between nearest-neighbor sites per lattice distance.

The important consideration in SmB and SmE phases is the number of available (nearest) hopping paths and the distance between the neighboring sites. Differences in the magnitude of the mobility between these two mesophases comes from the difference in the intermolecular distance and the number of available hopping paths within the layers.

We assume that the energy-localized state at ε is characterized by a Gaussian-distributed density of states (DOS)

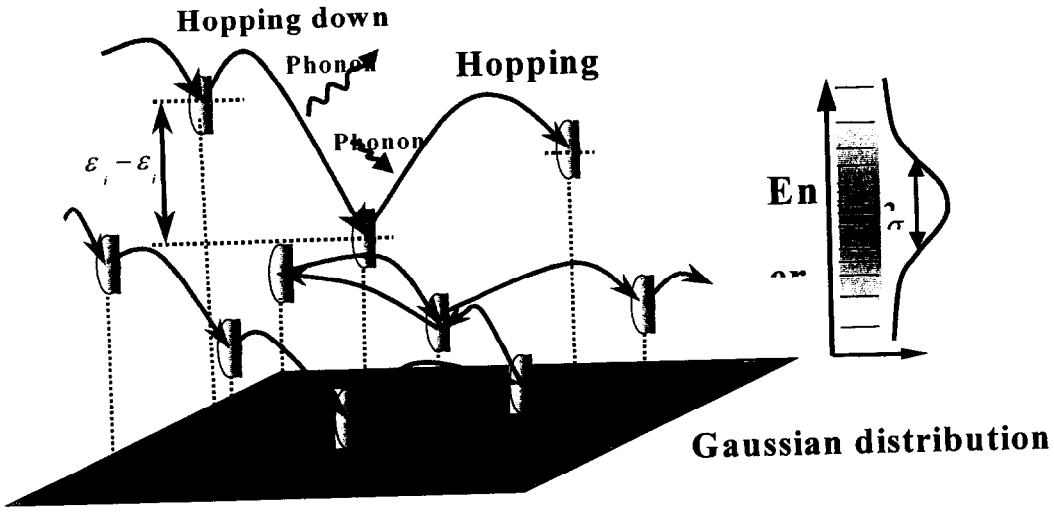

Fig. 6.1 : Scheme of hopping process concerning the energy levels without applied field. Hopping needs activation for jumping up from i to j site, while hopping down needs no energy. Gaussian distribution is supposed for the energy levels.

$$g(\varepsilon) = \frac{1}{\sqrt{2\pi}\sigma} \exp\left(-\frac{\varepsilon^2}{2\sigma^2}\right), \tag{6.2}$$

as is used in the case of the disordered organic solids, where σ is the energetic width. In an amorphous organic material, the energetic disorder characterized by σ reflects the fluctuation in the polarization energy and charge-dipolar interactions. The long-range nature of the charge-dipole interaction has been shown to play a crucial role, for it creates a spatial correlation in the DOS, so that the potential change an neighboring sites is smooth. Inour materials, however,the molecular dipole moment is small, and the energetic disorder is caused by the carrier-dipole interactions is negligable. We attribute σ to the SLC structure or to relative position between cores of molecules as producing polarization energy.

A reasonable transition rate for hopping processes was suggested by Miller and Abrahams [18]. It is the product of pre-factor ν_0, a carrier wave-function overlap factor, and a Boltzmann factor for jumps upward in energy [16], i.e. the jump rate between sites i and j, the distance between the sites being r_{ij}, is

$$\nu_{ij} = \nu_0 \exp\left(-\frac{2r_{ij}}{\alpha}\right)\begin{cases}\exp\left[-\dfrac{\varepsilon_j - \varepsilon_i - e\boldsymbol{E}\cdot\boldsymbol{r}_{ij}}{kT}\right] & (\text{for } \varepsilon_j - \varepsilon_i - e\boldsymbol{E}\cdot\boldsymbol{r}_{ij} > 0.)\\ 1 & (\text{for } \varepsilon_j - \varepsilon_i - e\boldsymbol{E}\cdot\boldsymbol{r}_{ij} < 0.)\end{cases} \tag{6.3}$$

Here, α is a specific decay length of the wave function in the localized states , $\boldsymbol{r}_{ij}$ is the vector from the site i to j, and $\boldsymbol{E}$ is the applied electric field. The quantity $e\boldsymbol{E}\cdot\boldsymbol{r}_{ij}$ is the difference of electro-static potential between the ith and jth hopping sites. The only source of activation energy comes from the difference in site energies, and the rate is only thermally activated for an "uphill" hop (Fig.6.1). In the smectic mesophases, except for smectic A phase, the dependence the off-diagonal disorder is less important than the energetic disorder. In the Smectic A phase, we introduce spatial disorder by modifying the value of r_{ij} which enters into the jump rate according to fluctuations which are determined from a number drawn from a Gaussian distribution

$$g(\Gamma_k) = \frac{1}{\sqrt{\pi\Sigma^2}}\exp\left[-\frac{(\Gamma_k - R_{ij}/\alpha)^2}{\Sigma^2}\right], \tag{6.4}$$

In (6.4) Γ_k is the dimensionless positional parameter for each site, R_{ij} is the distance between the lattice points i and j, and r_k is the deviation of the site from the lattice point. Ignoring non-nearest neighbor hopping, we have $R_{ij} = a$ and in such a case the distance r_{ij} is given by

$$r_{ij} = \alpha(\Gamma_i + \Gamma_j). \tag{6.5}$$

The probability P_{ij} for jumping from a site i to a site j within a two-dimensional lattice is

$$P_{ij} = \frac{\nu_{ij}}{\sum_k \nu_{ik}}. \tag{6.6}$$

and the dwell time of a carrier at a site i is described by the following equation:

$$t_{ij} = -\frac{\ln(x)}{\sum_k \nu_{ik}}. \tag{6.7}$$

Here, x is a random number taken from a uniform distribution between 0 and 1. The sum is taken over all connected sites k except for the site i from which the hop commences.

6.3 Scheme of Monte Carlo Simulation

We carried out two-dimensional simulations on a model layer consisting of 100×1000 or 100×5000 sites aligned as a hexagonal lattice and a rectangular lattice, to compare with the experimental results in SmB and SmE phase, respectively. The lattice configuration for the SmA phase was also taken to be rectangular, but the sites were shifted from their lattice points according to the recipe described above. To extend the lattice size in the direction perpendicular to the applied field we applied a periodic boundary condition. For the site

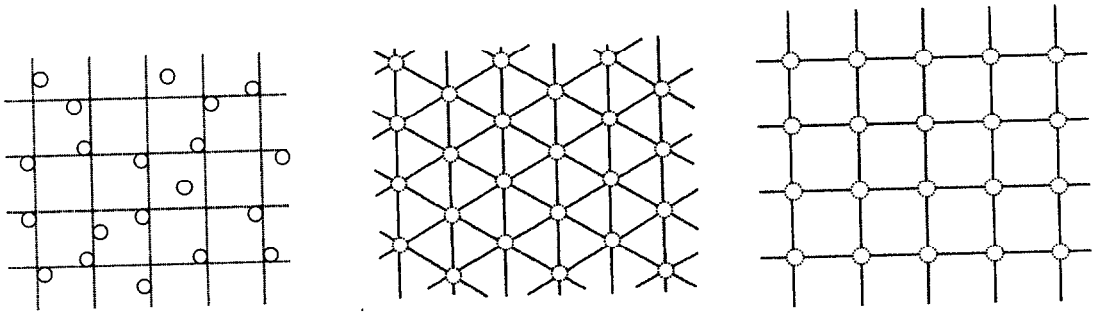

(a) SmA (b) SmB (c) SmE

Fig. 4.2 :Schematic illustration of alignment of the site in the layer for each pahase.

distance a=3~5Å, 5000 sites corresponds to a sample length of 2μm, which is typical of the thickness of the actual samples examined in time-of-flight experiments (Fig. 6.3). The parameters were chosen as: ν_0= 6×10^{12} Hz, and α=2.3 Å. The distance between neighboring sites, a, is to be 4.6 Å in SmB and 3.5 Å in SmE phase based on the measurements of nearest neighbor distance between molecules by X-ray diffraction [17].

Prior to the simulation, each of the hopping sites is assigned an energetic shift ε_i and a positional parameter Γ_i. In the simulation we allow a charge to start at arbitrary selected sites located near the top electrode. The charge then hops randomly around the sites according to the probability P_{ij} to transfer from i to j (eq.6.6) during the time t_{ij} (eq.6.7), and disappears on arriving at one of the sites adjacent to the counter electrode. This process is repeated N=1000 times. For each random walk a transit time t_n is calculated. Average velocity <v> is thu

$$<v>=\frac{1}{N}\sum_{n=1}^{N}{}_{n}$$

Fig. 4.3: Scheme of GDM simulation: The simulation measures the transition time from the top electrode to the counter electrode on the two-dimensional layer.

where L is the sample length. The mobility μ_a is calculated as

$$\mu_a=\frac{<v>}{E}=\frac{1}{NE}\sum_{n=1}^{N}\frac{L}{t_n}. \qquad (6.9)$$

6.4 Simulation of Field Dependence

6.4.1 Simulation results for SmB compared with experimental results of 8-PNP-O12

We made computational simulations for each of the phases. First, we examined the simulation for the SmB phase and compared this with the measurements on 8-PNP-O-12.

The behavior of the calculated charge carrier mobility as a function of the electric field is shown in Fig. 6.4, for varying values of σ. We can recognize

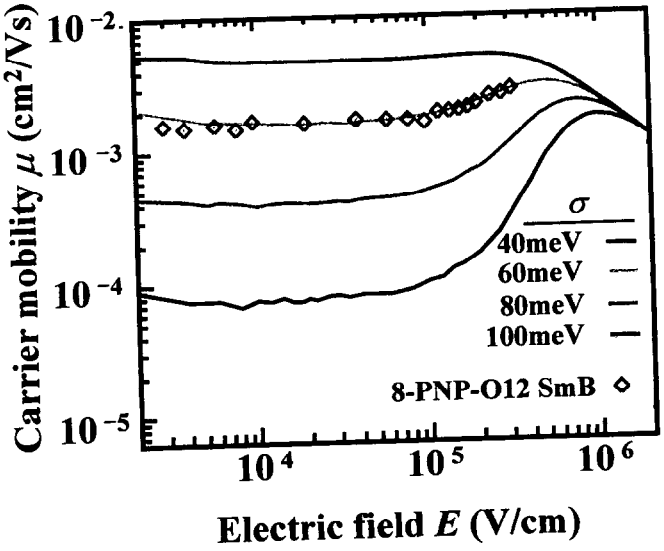

Fig. 6.4: Field dependence of carrier mobility in SmB. The lines show the simulation results. Open diamonds are experimental data.

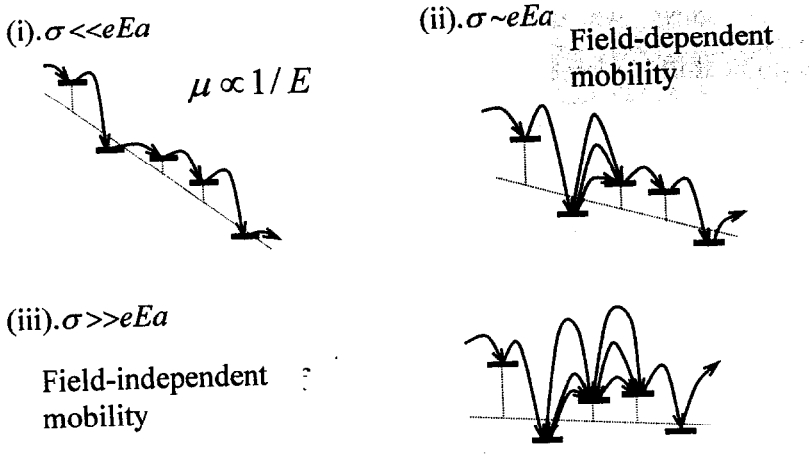

Fig. 6.5 :Schematic illustration of hopping process for various field

Fig. 6.5: Schematic illustration for hopping process under various field. (I) High-field region experimentally not realized. (ii) Field dependence with Pool-Frenkel like behavior. (iii) Field-independent region.

the existence of a region having a Poole-Frenkel behavior as well as a region of field-independent mobility. In fact, there are three separate regions:. (i)a high-field region $\sigma << eEa$, where the mobility decreases with increasing electric field, (ii) a region with a field-dependent mobility (the Poole-Frenkel region) in the range $\sigma \sim eEa$, and (iii) a region with a field-independent mobility ($\sigma >> eEa$).

One may also notice a transition at low field. Below a certain field the mobility is no longer constant, but begins to decrease with increasing field.. If we look at the low-field region for various sample lengths, from 0.04 to 2μm (from 100 to 5000 sites), we find that the transition point shifts to lower fields (Fig. 6.6) for longer sample lengths. The reason for the transition is as follows. If the sample length is very thin, the carriers can arrive at the counter electrode through diffusion motion, even in the absence of an applied field. The diffusive motion is field independent, to first order. Thus, the calculated transit time in simulation becomes field

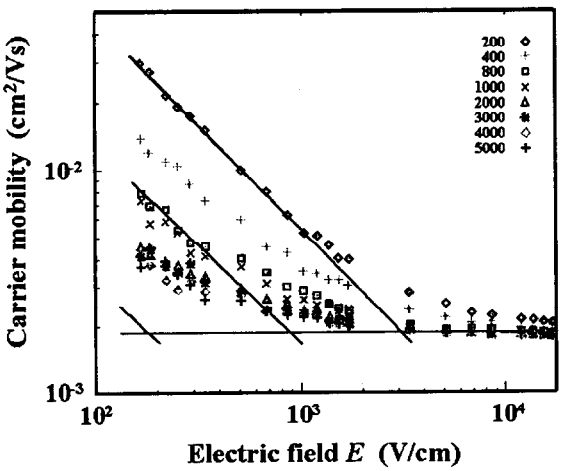

Fig. 6.6: Sample-thickness (site number) dependence of the mobility at low field: "μ-1/E dependent region at low fields" shifts to the left with increasing number of sites existing along the direction of applied field.

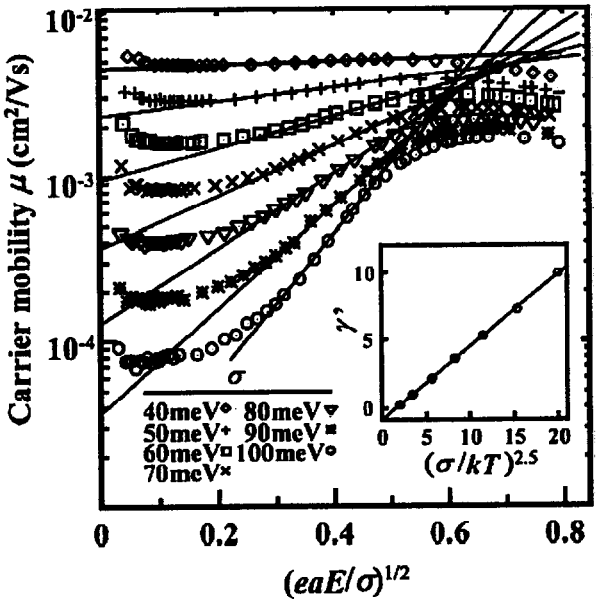

Fig. 6.7: Simulation results showing field dependence of the carrier mobility in SmB phase. The inset shows the slope of log(γ) vs. $\sigma^{2.5}$.

independent, leading to an inferred time-of-flight mobility $\mu \sim$ 1/E which decreases with increasing electric field.

In region (i) where the field is very high, over 10^6 V/cm, and the potential difference between two neighboring molecules due to the field is larger than the mean energetic fluctuation σ, most of the hops take place in the direction of the field. For the Miller and Abrahams rates, the hopping down process does not depend on the field, the drift velocity becomes field-independent, and therefore $\mu_a \propto 1/E$. This region cannot be realized in the present experiment because in most cases our samples break down.

In region (ii) where the electric field strength is in the range of about 10^5~10^6V/cm, the drift and diffusion of the carriers depends on E. To parameterize the Poole-Frenkel behavior, we apply a trial function of the following form:

$$\mu = \mu_0 \exp\left[(c\hat{\sigma})^n + \gamma'\sqrt{eaE/\sigma}\right], \tag{6.10}$$

$$\gamma' = C'(\hat{\sigma}^m - \Gamma), \tag{6.11}$$

where $\hat{\sigma} = \sigma / kT$. This form was first introduced by Novikov *et al* [18] to describe the results in the case of correlated disorder. Fig. 6.7 shows the mobility *vs.* $\sqrt{eaE/\sigma}$ for calculations pertaining to the SmB phase. This behavior is also typical for three-dimensional (Bässler *et al* [1]) and one-dimensional systems (Bleyl *et al* [19], Novikov *et al* [20] and Kohary *et al* [11]). We have obtained $\mu_{zf} = \mu_0 \exp[-(c\hat{\sigma})^2]$ *via* extrapolation to zero field. We plot the $\log\mu_{zf}$ *vs.* $\hat{\sigma}^2$ to obtain $\mu_0 = 1.44\times10^{-2}$ cm^2/Vs, c = 0.8 and n = 2. However, the value of c varies only slightly with the decay length α or the distance between neighboring sitesr, as is indicated in Table 4.1. To get C', m, and Γ, we calculated γ', the slope of $\log(\mu)$ vs. $(eaE/\sigma)^{1/2}$ and plotted γ' against $\hat{\sigma}^{2.5}$ as shown in the inset of Fig. 6.7. We obtained: $C' = 0.54$, $m = 2.5$ and $\Gamma = 0.87$.

TABLE 4.1 Coeffcients c in Eq. (6.10) versus decay length α

α(Å)	1.6	1.8	2.0	2.2	2.3	2.6	2.8
C	0.83	0.84	0.82	0.80	0.80	0.80	0.80

We also performed simulations for a two-dimensional hexagonal lattice applied to SmB phase, and fit the mobility to the expression

$$\mu_{SmB} = \mu_0 \exp\left[-\left(0.80\frac{\sigma}{kT}\right)^2\right]\exp\left\{C'\left[\left(\frac{\sigma}{kT}\right)^{2.5} - \Gamma\right]\sqrt{\frac{eaE}{\sigma}}\right\}. \quad (6.12)$$

This equation describes asymptotes to the simulated data in Fig. 6.7. The range in which eq. (6.12) holds is very narrow. When we applied Correlation Disorder Model (CDM), on the other hand, eq. (6.12) holds in a wide-field range as pointed out in ref 20. But CDM supposes the charge-dipole interactions [9]. We cannot find such kind of strong interactions in our SLC, 8-PNP-O12 or 8-PNP-O4. So we did not think of adopting CDM instead of GDM in this chapter. Thus, in GDM, we can say that region (ii) is the region in which field-dependent mobility is shown and eq. (6.12) is shown around the inflection point of this region.

Fig. 6.4 shows that region (ii) with field-dependent mobility becomes pronounced with increasing σ. These results suggest that for smectic liquid crystal, where only small value of σ is expected due to orientation effect, the Poole-Frenkel-like behavior will disappear in the field range of 10^4~ 10^5 V/cm often employed in TOF experiments.

In region (iii) where the electric field is in the range < 10^5V/cm and the mobility is independent of electric field, we found that the model with σ = 60 meV showed a good agreement with experiment [20], as shown with diamonds in Fig. 6.4. The width of the disorder σ =60 meV is considerably smaller than a typical value σ =100~120meV in the organic disordered solids [1]. This is probably due to the fact that the hopping sites in the smectic mesophase have more structure. As shown in Fig. 6.4, different behaviors of the mobility appear in regions (ii) and (iii), where the diffusion process plays a significant role in the hopping process, depending on the σ and E. These results are shown in Fig. 6.8, where $\log(\mu T)$ is plotted vs. $(1000/T)^2$ at constant field $E = 8\times10^4$ V/cm belonging to region (iii). We find that the simulated results are consistent with the relation:

$$\mu = \frac{e}{kT} A \exp\left[-(B\hat{\sigma})^2\right] \quad (6.13)$$

This implies that the diffusion coefficient depends on $\hat{\sigma}^2$, $D = A\exp[-(B\hat{\sigma})^2]$, assuming that the Einstein relation holds. This is confirmed from the inset of Fig. 6.8. Here, all the points were calculated by using eq. (6.13) with the same parameters: $A = 2.9\times10^{-4}\text{cm}^2/\text{s}$ and $B = 0.67$. The eq. (6.13) shows that the diffusion process does not depend on field E in region (iii)..

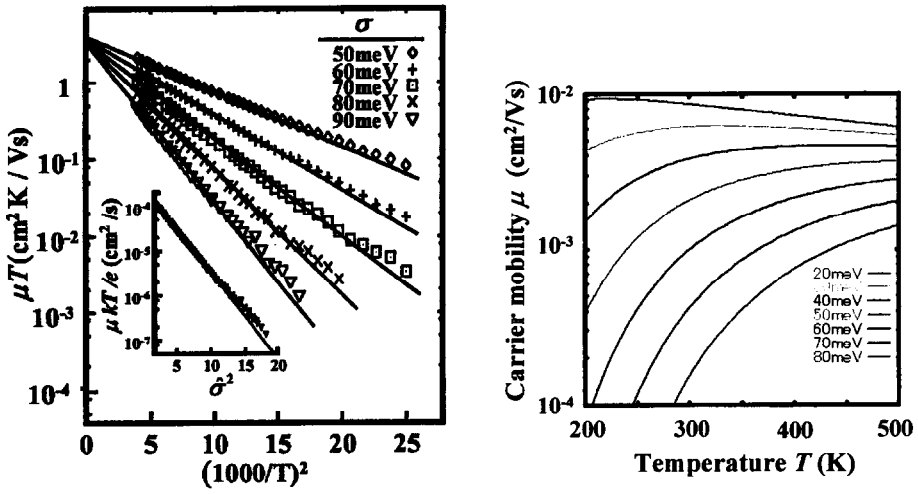

Fig. 6.8 Temperature dependence of the carrier mobility: (a) μT *vs* $(1000/T)^2$ The inset shows $\log(\mu kT/e)$ vs. $\hat{\sigma}^2$ (b) m vs T plots based on eq.(6.13)

Our simulated results are consistent with the experimental ones on 8-PNP-O12 [22]. The simulation, however, predicts the appearance of field-dependent mobility at the high fields E for 8-PNP-O12. To test this prediction, we have attempted a mobility measurement using 8-PNP-O12 over an extremely wide range of electric field including strengths over 10^5V/cm. The temperature of the sample was maintained at 80°C so as to maintain the SmB phase. The experimental details are described in Chapter 2. The diamonds in Fig. 6.4 show the experimentally measured mobility as a function of electric field in SmB. The transition from a field-independent mobility to a field-dependent mobility in the experiment is consistent with the simulated predictions using σ = 60meV. The separation of region (iii) from region (ii) is dependent on σ, as is clearly seen in Fig.6.4. The region (ii) will extend with an increase in the σ value. The conventional disordered organic solids with a small σ

value over 100 meV have a narrow region (ii) at lower electric fields, e.g., 10^5 V/cm. This is the reason why the field-independent mobility has been overlooked hitherto in the amorphous organic solids.

6.4.2 Simulation results for SmE and SmA phases

We also performed simulations to describe the behavior in the SmE and SmA phases. We did not directly compare with the experimental results in these cases because we could not find suitable parameters to fit the experimental data. (We do not know the distance between neighboring sites in the SmA phase. The distance between neighboring sites in SmE have been obtained from x-ray diffraction studies [14]. Instead of fitting eqs. (6.12) and (6.13) to the results of the simulation, We also fit the results to Bässlers equation,

$$\mu = \mu_0 \exp\left[(c\hat{\sigma})^n + \beta\sqrt{E}\right], \tag{6.14}$$

$$\beta = C(\hat{\sigma}^m - \Sigma_0), \tag{6.15}$$

To model transport in the SmE phase, the distance between neighboring sites a was set to 3.5 Å. The other parameters were taken to be the same as those for the SmB phase. In the simulation, we let 2000 carriers walk randomly, one at a time, through 100×1000 sites aligned in rectangular lattice. The typical behavior of the calculated charge-carrier mobility is shown in Fig. 6.9 , as a function of the electric field, and parametric in the value of σ .

As in the simulations for the SmB phase, we find a region showing a field-dependent mobility and a region showing a field-independent mobility. We also see two other regions showing $\mu \sim 1/E$, in lower- and higher-fields, which have been discussed previously in the context of the SmB phase. When Fig. 6.9 for the SmE phase is compared with Fig. 6.4 for the SmB phase, one may notice that the regions in Fig. 6.9 shift to right side (to higher fields) by about a factor of three and that the mobility values increase dramatically, by an order of magnitude. These changes come about because of changes in the distance between the nearest neighbor sites. We verified this by simulating SmE with the same parameters

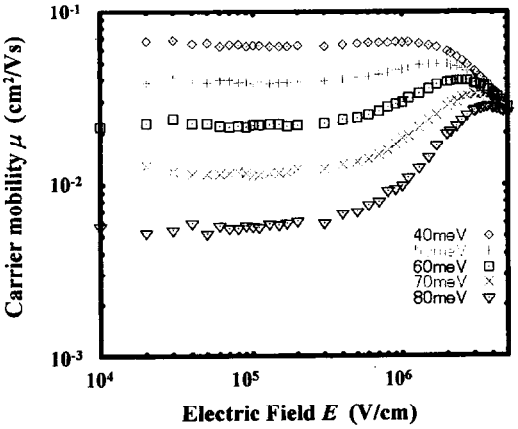

Fig. 6.9: Simulation results showing field dependence of carrier mobility in SmE

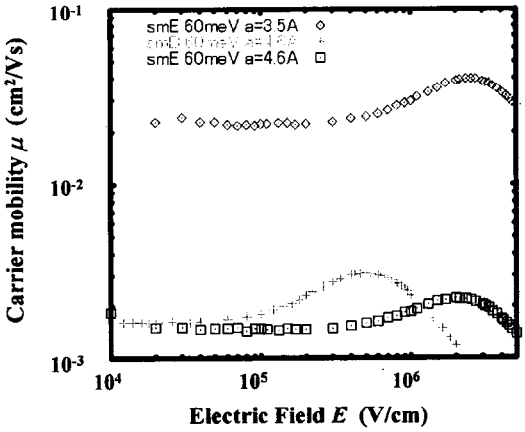

.Fig. 6.10: Simulation results showing field dependence of mobility: (i) SmE, (ii) SmB and SmE with the nearest-neighbor site distance being taken as the same as in SmB.

used for SmB, except for a = 4.6Å, In such a case, the mobility for SmE is the same as the mobility for SmB. (see Fig. 6.10).

Figure 6.11-(a) shows the mobility *vs.* $\sqrt{E}$ relation for SmE phase. We obtain $\mu_{zf} = \mu_0 \exp[-(c\hat{\sigma})^2]$ by extrapolation to zero field. Plotting the $\log\mu_{zf}$ *vs.* $\hat{\sigma}^2$ gives

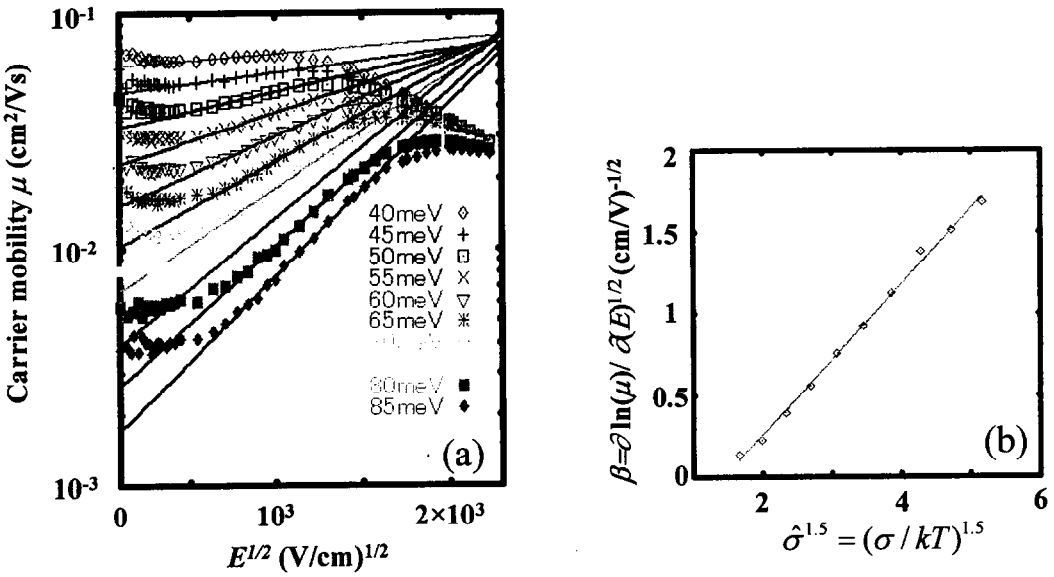

Fig. 6.11 (a) Simulated result on field- dependences of the carrier mobility of SmE phases. (b)The inset shows the slope of log(β) vs. $(\sigma/\kappa T)^{1.5}$

$\mu_0 = 1.66\times10^{-1}$ cm^2/Vs and c = 0.74. However, the value of c varies only slightly with the decay length α or the distance between neighboring sites a, as indicated in TABLE 6.2. Fig. 6.11-(b) shows the Poole-Frenkel slope $\beta = \partial\log(\mu)/\partial\sqrt{E}$ vs. $\hat{\sigma}^{1.5}$. We obtained the parameters of eq. (6.15): $C = 4.6\times10^{-4}$, m = 1.5 and Σ_0 = 1.4 by fitting the line as shown in Fig. 6.11-(b). Finally we derived the corresponding parameters for a two-dimensional rectangular

TABLE 6.2 Coefficient c in Eq. (6.14) vs. decay length α

α(Å)	1.6	1.8	2.0	2.2	2.3	2.6	2.8
c	0.75	0.75	0.74	0.74	0.74	0.74	0.73

lattice to compare with the experimental results in the SmE phase.

In the region of field-independent mobility, where E < 3×10^5 V/cm, log(μT) is plotted vs. (1000/T)^2 for E = 1×10^5 V/cm as shown in Fig. 6.12. Eq. (6.13) is also consistent with the simulated results, with $A = 3\times10^{-3}$cm^2/s and B = 0.53.

In in order to compare with the SmA phase, the simulations were carried out as follows. The distance between neighboring sites a was set to be 5Å. The number of random walks carried out was 2000 These took place on a rectangular lattice of 100×1000. The value of Σ was talen to be 1, 1.2,1.4, 1.5, and 2. in the other parameters were taken to be the same as were taken to desribe the SmB phase. The calculated behavior of the charge carrier mobility for SmA is shown as a function of the electric field, and as a function of σ, as shown in Fig. 6.13.

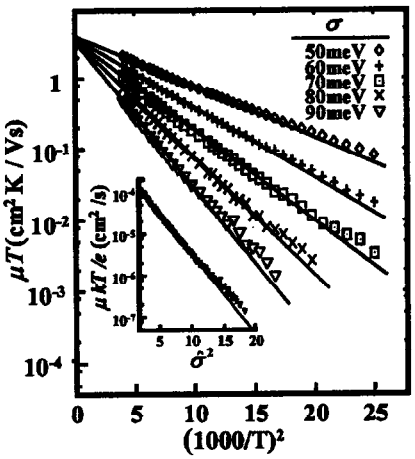

Fig. 6.12 :Temperature dependence of the carrier mobility in SmE, The inset shows log(kT/e) vs. σ^2

As in the previous simulations, we find regions showing field-dependent and field-independent mobilities. In addition, there is a new region in which the mobility decreases with increasing field. This region is not the region showing $\mu \sim 1/E$, which we already mentioned. This dependence takes place at E = ??????, and is instead caused by the off-diagonal disorder Σ when Σ>1.5. Because this dependence has not been found in the experiment, we conclude that Σ<1.5. Each region shifts by a factor of three to the left side (to lower fields) as compared with SmB. This behavior is shown in Fig. 6.4. Mobility

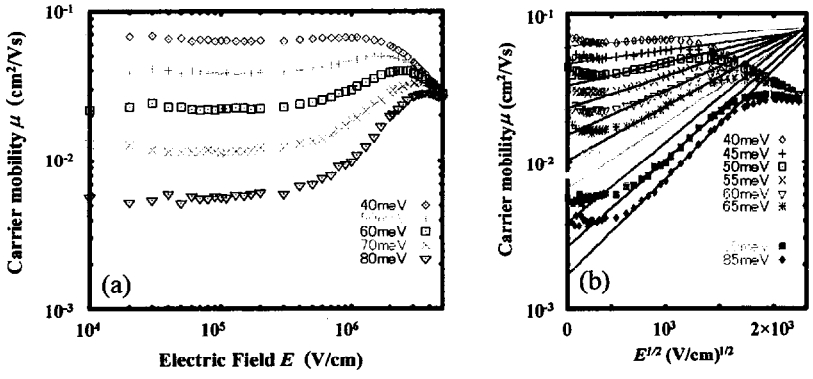

Fig.6.15: Field dependence of the mobility in SmA: (a) on double-logarithmic plot, (b) $E^{1/2}$-dependence.

decreases with increasing lattice constant by half an order of magnitude more than it does in SmB.

Fig.6.13-(b) shows the mobility *vs.* $\sqrt{E}$ curve in the SmE phase. Again we have fit the function $\mu_{zf} = \mu_0 \exp[-(c\hat{\sigma})^2]$ by extrapolation to zero field, and plotted the $\log\mu_{zf}$ *vs.* $\hat{\sigma}^2$ to obtain $\mu_0 = 5.2\times10^{-3}\,\mathrm{cm^2/Vs}$ and c = 0.75. The inset of Fig. 6.13-(b) shows the slope $\beta = \partial\log(\mu)/\partial\sqrt{E}$ vs. $\hat{\sigma}^{1.5}$. We obtained the following fit parameters $C = 2.2\times10^{-4}$, m = 1.5 and Σ_0 = 1.5.

Finally we performed simulations on a two-dimensional rectangular lattice in order to compare with experimental results for the SmE phase.

In the region of field-independent mobility, E < 3×10^5 V/cm, we have compared the $\log(\mu T)$ vs. $(1000/T)^2$ at a constant field E = 1×10^5 V/cm. This comparison is made in

Fig.6.14. The relation described by eq. (6.13) is consistent with the simulated resultswith $A = 3\times10^{-3}$ cm^2/s and $B = 0.53$.

In summary, we have applied the disorder formalism for charge transport in SmA, SmB and SmE phases, obtaining field dependencies which are as follow:

$$\mu_{SmA} = \mu_0 \exp\left[-\left(0.75\frac{\sigma}{kT}\right)^2\right]\exp\left\{C\left[\left(\frac{\sigma}{kT}\right)^{1.5} - 2.25\right]\sqrt{E}\right\}, \quad (6.17)$$

$$\mu_{SmB} = \mu_0 \exp\left[-\left(0.80\frac{\sigma}{kT}\right)^2\right]\exp\left\{C\left[\left(\frac{\sigma}{kT}\right)^{2} - \Sigma_0\right]\sqrt{E}\right\}, \quad (6.12)'$$

$$\mu_{SmE} = \mu_0 \exp\left[-\left(0.74\frac{\sigma}{kT}\right)^2\right]\exp\left\{C\left[\left(\frac{\sigma}{kT}\right)^{1.5} - \Sigma_0\right]\sqrt{E}\right\}. \quad (6.16)$$

Here we denote disorder formalism of SmB by the same form of eqs. (6.14) and (6.15) of disorder formalism for various SLC phases as shown in TABLE 6.3. The parameters of one-dimensional [1] and three-dimensional [21] disorder formalism are shown too. These two parameters seem to reflect dimensions.

TABLE 6.3 Disorder parameters concerning dimension number.

	1D[21]	SmE	SmA	SmB	3D[1]
c	0.9	0.74	0.75	0.80	0.67
m	1	1.5	1.5	2	2

With higher dimensions, a lower value of the parameter c is obtained. The reason for this behavior is because, when more nearest neighbor sites are available, carriers can find a site to hop more easily, and they are able to avoid the higher energetic barriers. This lowers the activation energy. On the other hand, m increases with increasing dimension, m being concerned to the number of path from the carrier-dwelling site to the nearest-neighbor sites. The path number is two for 1D, four for SmE (2D) and SmA (2D) and six for SmB (2D) and 3D, each categories having the same number of m, respectively.

6.4.3 Comparison to the experiments

The various smectic mesophases in the smectic liquid crystals exhibit carrier transport properties which are different from those found in conventional organic disordered materials. For example, most of the smectic mesophases so far investigated including 2-phenybenzothiazole [21], 2-phenylnaphthalene [22], terthiophene [23], and terphenyl derivatives [24], exhibit a temperature- and field-independent mobility. One exception, discussed in section 6.4.1, concerns the SmB of 8-PNP-O12, which shows a region exhibiting a Poole-Frenkel behavior at high fields.. Because of electrostriction occurring at high fields, we could not confirm a similar behavior in the SmA phase of the same material.. The activation energy for 8-PNP-O12 cannot be determined accurately because the temperature range is narrow in each of the phases.

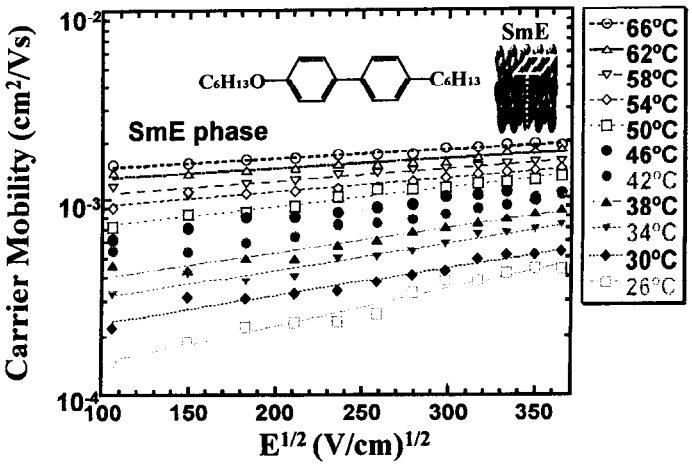

Fig. 6.15: Charge carrier mobility of SmB and SmE phases in a biphenyl derivative of 6O-BP-6 as a function of electric filed and temperature.[27]

Haruyama *et al* [25] have found recently that some of the biphenyl derivatives, 6O-BP-6, show a field- and temperature-dependent mobility. This behavior should be attributed to the intrinsic charge-carrier transport properties, judging from the fact that this property was observed in 6O-BP-6 irrespective of the synthetic routes. Applying the SmE phase-disorder

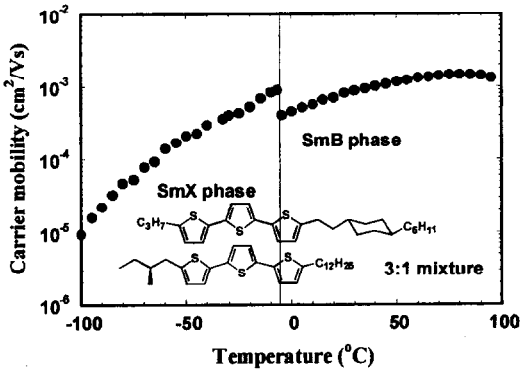

Fig. 6.16: Charge carrier mobility in SmB and SmX phases of a terthiophene mixture as a function of temperature.[28]

formalism, eq. (6.16), to the experiments in the SmE phase, we found parameters.σ = 114meV, μ_0 = 14(cm^2/Vs), C = 2.1x10^{-3} (cm/V)$^{1/2}$, and Σ_0 = 7.2. These values are rather large compared with those extracted from the simulation. As noted before, the carrier transport in our material ought to be explained by the GDM rather than CDM. So, the range where the eq. (6.16) holds is very narrow. The range found in simulation seems to be at higher fields than that found in the experiment. Moreover, the disorder parameter σ is larger than expected, and close to that found in amorphous organic materials.

Funahashi *et al* [26] investigated the temperature-dependent mobility in SmB and SmX phases of terthiophene derivatives (3:1 mixture of 3-TTP-C2CH-5 and 5*TTP-12) in which the temperature range of SLC phase is wide, from –15°C to 100°C for the SmX phase and from –15°C to 101°C for the SmB phase. The plots demonstrate a strong-temperature dependence at low temperatures (Fig. 6.16). They analyzed the results in the two phases by using the three-dimensional disorder formalism. The calculated paramters are shown in TABLE 6.4. Instead of using the 3D-disorder formalism, we compared our SmB- and SmE-disorder formalism to SmB and SmX phases, respectively. The modified parameters are included in TABEL 6.4. The value of σ in SmB of terthiophene is smaller than before, and 2/3 smaller than that in the SmB phase of of 8-PNP-O12. When liquid-crystalline phases of the materials are maintained at low temperatures aroundT=250 K, , we observe a temperature dependence of the mobility. This shows that the lack of temperature dependence at high temperatures does not imply an absence of disorder, but only that the disorder is small.

TABLE 6.4 Disorder parameters of terthiophene derivative mixtures

Phase (applied model)	μ_0 (cm^2/Vs)	σ(meV)	C (cm/V)$^{1/2}$	$\Sigma(\Sigma_0^{1/2})$
SmB (3D)	2.4×10^{-2}	50.7	1.02×10^{-3}	1.77
SmB (SmB, eq. (6.12)')	2.4×10^{-2}	42.5	1.45×10^{-3}	1.48
SmX (3D)	4.3×10^{-2}	50.1	9.07×10^{-4}	1.67
SmX (SmE, eq. (6.16))	4.3×10^{-2}	45.4	1.11×10^{-3}	1.34

6.5 Summary

We have investigated the charge carrier transport in the smectic mesophases of liquid crystals of 2-phenylnaphthalene derivatives of 8-PNP-O12, by computational Monte Carlo simulation as well as by TOF experiments. The unique feature of a field-independent mobility observed is well explained by a two-dimensional disorder model with a Gaussian DOS The standard deviation of the Gaussian distribution σ is determined to be 60meV for the SmB phase by simulation, and by analyzing the experimental observations. This small σ value, about half the typical value of 100~120meV observed in disorder organic materials, is characteristic to carrier-transport properties in smectic liquid crystalline phases. The disorder model predicts the existence of a field-dependent region at very high fields which has not been reported experimentally. To confirm this prediction, we carried out time-of-flight measurements of 8-PNP-O12 in an extended field region . We found that the mobility depended on the electric field, confirming the validity of the model.

For the SmB, SmE and SmA phases, we applied the disorder formalism for the field-dependent region .. For the field-independent mobility region we derived another formalism described by eq. (6.13. Some parameters of the formulae reflect dimension and site configuration.

It has been shown in this Chapter that the charge-carrier transport behavior, field- and temperature-dependence as demonstrated by TOF experiments in smectic mesophases of biphenyl derivatives, may be well described by a two-dimensional hopping transport model with a Gaussian-distributed density of states. By contrast, the charge carrier transport in organic disordered materials is described by a three-dimensional disorder model.

The terthiophene mixture exhibited a temperature-dependent mobility below ambient temperatures for a wide temperature range. The Gaussian width σ was estimated to be about 40meV by using the present two-dimensional disorder formalism. This value is by 10meV smaller than that obtained by 3D formalism.

References

[1] D. H. Bässler, Phys. Status. Solidi. B **175**, 15 (1993).

[2] N. Sato, H. Inokuchi, and E. A. Silinsh, Chem. Phys. **115**, 269 (1987).

[3] R. F. Loring, J. Phys. Chem **94**, 513 (1990).

[4] R. Richart and A. Wagner, J. Phys. Chem. **97**, 3146 (1993).

[5] A. Dieckmann, H. Bässler, and P. M. Borsenberger, J. Chem. Phys **99**, 8136 (1993).

[6] S. V. Novikov and A. V. Vannikov, JETP **79**, 482 (1994).

[7] Y. N. Garstein, J. Chem. Phys. **100**, 9175 (1994).

[8] D. H. Dunlap, P. E. Parris, and V. M. Kenkre, Phys. Rev. Lett. **77**, 542 (1996).

[9] G. Pfister and H. Griffiths, Phys. Rev. Lett **40**, 659 (1978).

[10] H. Cordes, K. Kohary, P. Thomas, S. yamasaki, F. Hensel, and J. -H. Wendorrff, Phys. Rev. B **63**, 094201 (2001); K. Kohary, K. Kohary, H. Cordes, S. D. Barnovskii, P. Thomas, S. Yamasaki, F. Hensel, and J. -H. Wendorff, *ibid* **63**, 094202 (2001).

[11] G. W. Gray and J. W. Goodby, *Smectic Liquid Crystals* (Leonard Hill, Glasgow, 1985)

[12] Masahiro Funahashi, *Doctoral thesis, 「液晶性有機半導体の創製と電気伝導に関する研究」* Chap. 4, Tokyo Institute of Technology, 1999

[13] K. Kurotaki and J. Hanna, J. Iamg. Sci. Tech. **43**, 237 (1999).

[14] L. Pautomeier, B. Ries, R. Richert, and H. Bassler, Chem. Phys. Lett. **143**, 459 (1988).

[15] L. Pautomeier, R. Richert, and H. Bassler, Synth. Metals **37**, 271 (1990).

[16] A. Miller and E. Abrahams, Phys. Rev.. **120**, 745 (1960).

[17] M. Funahashi, and J. Hanna J. Mol. Cryst. Liq. Cryst. **368**, 4071 (2001).

[18] S. V. Novikov, D. H. Dunlap, V. M. Kenkre, P. E. P.arris, and A. V. Vannicov, Phys. Rev. Lett. **81**, 4472 (1998).

[19] I. Bleyl, C. Erdelen, H. -W. Schmidt, and D. Haarer, Philos. Mag. B **79**, 463 (1999).

[20] M. Funahashi and J. Hanna, Appl. Phys. Lett. **71**, 602 (1997).

[21] M. Funahashi and J. Hanna, Phys. Rev. Lett **78**, 2184 (1997).

[22] M. Funahashi and J. Hanna, and J. Hanna, Appl. Phys. Lett **71**, 602 (1997).

[23] F. Funahashi, Appl. Phys. Lett **76**, 2574 (2000).

[24] T. Shimakawa, Y. Talkayashiki, and J. Hanna, unpublished data , ( ).

[25] A. Haruyama, Master's thesis (2002)

[26] M. Funahashi, and J. Hanna, Mol. Cryst. Liq. Cryst., inpress.

Chapter 7

Consistency between the Multiple Trapping Model and the Gaussian Disorder Model

7.1 Introduction

The implications of the disorder model described in Chapter 6 is understood via a Monte Carlo simulation in which it is assumed that the density of states (DOS) is a Gaussian [1].It is difficult to compare the GDM simulation with experimental results, because the results are statistical, and cannot easily be fit to the experimental data using, say, the method of least squares. For this reason, it is difficult to confirm the accuracy of the GDM-photocurrent predictions. On the other hand, as shown in Chaps. 3 and 5, in the MTM things are simpler, for we consider a dichotomy consisting of the "transport state" [2] and the "trap states". Nevertheless, even at the level of the MTM, the two parameters, the attempt frequency ν_0 for the thermally activated trap release rate and the energy ε_0 which decides the center position of the Gaussian trap distribution can not be determined simulataneously. The best we can do is to arbitrarily fix one one of these parameters and fit the other. In this chapter we will form a bridge between the GDM and the MTM by fitting the the photocurrent produced by the GDM with the MTM. We find that the GDM and the MTM are complementary to one another.

7.2 TOF Photocurrent of GDM

We begin by showing how to obtain the photocurrent transient from Monte Carlo (MC) simulations of the GDM (another method, which does not use MC simulation, is explained in Ref [3]). The normalized current $I_N(t)$ is the current divided by total charge Q initially existing between both electrodes, i.e.

$$I_N(t) = \frac{I}{Q} = \frac{en < v(t) >}{eN} = \frac{< v(t) >}{L}, \tag{7.1}$$

where N is total number of carriers and n is average carrier density in the system. The sample length L is equal to the product of the length a between the nearest-neighboring sites and the number of sites j_0 between the electrodes.

$$L = a \times j_0 . \tag{7.2}$$

The instantaneous drift velocity

$$< v(t) > = \frac{1}{N} \sum_{i=1}^{N} \frac{x_i(t) - x_i(t - \delta t)}{\delta t} . \tag{7.3}$$

is given by an average over an ensemble of N random walks (N=2000 – 5000) of the

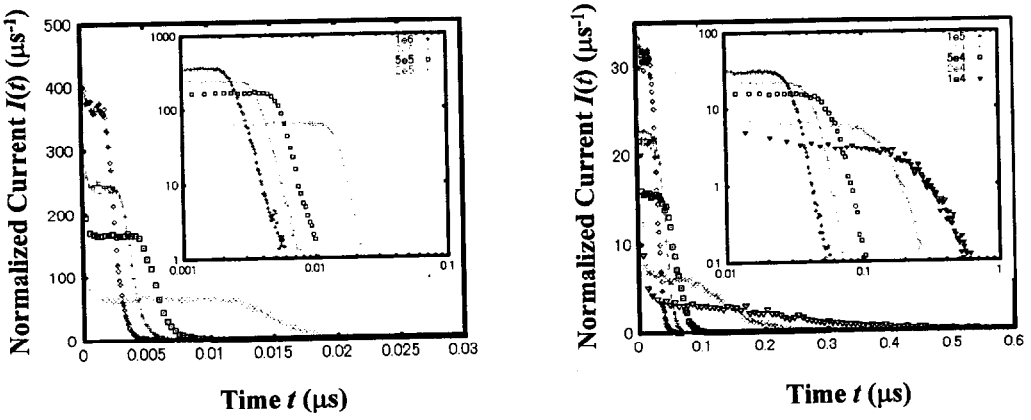

Fig. 7.1 :TOF transient photocurrent of GDM

difference in location $x_i(t)$ of a carrier at time t and the location $x_i(t-\delta t)$ of a carrier after a time interval δt, where the time interval is taken to be much smaller than the transit time, but much larger than the time for a typical hop.

The diffusion constant is defined through the second moment;

$$D = \frac{< x(t)^2 > - < x(t) >^2}{2t}. \qquad (10)$$

By substitution of Eq. (7.3) in Eq.(7.1) we obtain the TOF photocurrents as produced by the simulation.

We produced transients for the following specifications: Sample length L = 3Å×1000 = 0.3μm, temperature T = 340 K , tunneling decay rate $\alpha = 2.3$Å and attempt frequency $\nu_0 = 10^{12}$ Hz. The results are shown in Fig. 7.1. The evaluated currents seem to be similar to the shape of the experimental transients.

7.3 TOF Photocurrent of GDM fiited by Gaussian type of MTM with Diffusion

Now we apply the MTM model with diffusion to fit the TOF signal produced by the GDM [4]. As we mentioned, one problem with the MTM is that we can not determine the energetic position of the distribution of traps relative to the "free" state manifold without knowledge of the detrapping attempt frequency. However, we can estimate the effective mean of the trap density by applying the MTM to the simulated data and taking the detrapping attempt frequency to be the same as the attempt frequency for the Miller-Abrahams jump rate. Let us take the trap distribution to have the same Gaussian shape as the density of states for the GDM, having a standard deviation σ= 60meV. We made a comparison for the case of E=2×10^{4}V/cm . For this choice of electric field, the fitting works well, as shown in Fig. 7.2.We fit the GDM transients for other values of E, maintaining the same Gaussian trap density in the MTM, but we allowed the centroid ε_0 to shift in order to

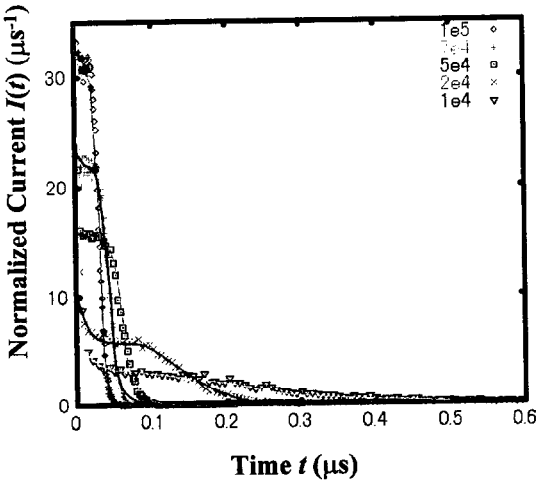

Fig. 7.2 :TOF transient photocurrent of GDM fitted by Gaussian MTM with diffusion

obtain the best fit.TABLE 7.1 shows the values of ε_0 for various fields. The behavior is rather significant, for if the MTM of the first part of this thesis is to be consistent with the GDM studied in the second part of the thesis, then ε_0 should be constant, independent of field. We see in Table 7.1 that, while there is a variation with field, the fluctuations are such that it is not possible to draw conclusions at this point as to whether ε_0 should increase or decrease with field, or generally remain constant, at least for these values of E.

TABLE 7.1 value of ε_0 versus field

E(V/cm)	7×10^5	5×10^5	1×10^5	7×10^4	5×10^4	2×10^4	10^4
ε_o(meV)	4.7	5.2	3.3	4.6	4.7	4.1	7.2

7.4 Discussion

In summary, if we demand that the two Gaussan distributions remain the same, that is that the Gaussian DOS used to generate transients with the GDM is the same as the

Gaussian trap density used in the MTM, we find that the fits of the generated transients with the MTM are excellent, over a wide range of fields, provided that we let the centroid of the Gaussian trap density be a fit paramter. At this point, however, our studies are insufficient to determine if the centroid will increase with field, decrease with field, or remain constant.

References

[1] D. H. Bässler, Phys. Status. Solidi. B **175**, 15 (1993).

[2] F. W. Schmidlin, Phys. Rev. B **16**, 2362 (1977).

[3] Jose A. Freir, J . Chem. Phys. **119**, 2348 (2003).

[4] B Hartenstein, H. Bassler, A. Jakobs, and K. W. Kehr, Phys. Rev. B **54**, 8574 (1996).

Chapter 8

Summary

We finally arrive at summarizing this dissertation. We began by describing the motivations and the background for this work. This was followed in Chapter 1 by a statement of aims and a brief introduction of the contents.

In Chapter 2, we first introduced the molecular structure properties of typical liquid crystals, which lead to the self-organized smectic mesophases, SmA, SmB, and SmE, and their molecular alignments, exhibiting orientational and positional (structural) order in two dimensions. We discussed how LCs represent an intermediate class of organic materials between single crystals and amorphous disordered materials, and how positional and energetic disorders can be involved, i.e., they form self-assembling, two-dimensional conducting pathways with dynamically induced disorders. Smectic liquid crystals (SmLC) are a unique model system for studying the relationship between molecular organization and charge transport properties. We explained why we selected the TOF-measurement among existing techniques for obtaining charge transport properties. This was followed by a detailed description of the experimental method we used, with merits and demerits included. We also presented some important theoretical approaches to clarify carrier transport mechanisms for organic disordered materials, such as modelings and simulation techniques.

In Chapter 3, we investigated carrier transport in smectic-liquid crystals by using the multiple-trapping model (MTM) to describe the experimental photocurrent. We showed that neither the simple MTM without diffusion, nor the convection-diffusion equation without trapping, can explain the time of flight current-time curves for SLC. Instead, we found that the two sources of dispersion, trapping and diffusion, must be combined.. We attempted to fit the data using the MTM with diffusion for several assumptions regarding the underlying trap distribution. We found that a Gaussian trap distribution with a width of 60meV can explain the carrier transport in SLC for a wide range of electric field. We found this fitting to be compatible with the Einstein relation in the low field region. We thus verified that the mobility is field-independent at low fields. In Chapter 4, we concentrated on negative charge carrier transport. Ionic

conduction has been observed for nematic liquid crystals (NLC) , but has not been observed for SmLC. We analyzed the negative carrier transport in SmLC and investigated the relation between electronic and ionic transport by applying the multiple-trapping model (MTM) for electrons and the convection-diffusion equation for ions. In doing so, we demonstrated that the dynamics of ionic conduction in SmLC appears to be different from that in NLC.

In Chapter 5 we tried to extract directly the information on the trap distribution from the experimentally observed TOF-photocurrent curves. Once this goal was met, three problems were discussed. First, as SmLCs provide a field-independent diffusion process consistent with the Einstein relation at low fields, diffusion effects may be separated from trapping effects in the broadening of the photocurrent. Second, the average-dwell time for an arbitrary-trap distribution may be determined by using Blankenbecler' technique to generate the Sommerfeld corrections. Finally, only the shape of trap distribution can be obtained without knowing how far apart the trap distribution is from the transport state. We point out that this problem may be solved by fitting current-time curves at various temperatures. Unfortunately, the SLC is stable for a very narrow temperature range. Additional problems, such as the range of time in the measurement and high-order derivative functions, producing enhanced noise, were discussed. We came up with a new method which can be applied to photocurrents for various field ranges and concluded that an SmLC has a Gaussian trap distribution. We also found a universal curve which retains all the information on trap. The parameters for describing this curve are given in TABLE 5.1

In Chapter 6, among the present results on the charge carrier transport in the smectic mesophases of liquid crystal, 2-phenylnaphthalene derivative of 8-PNP-O12, it was shown that a field-independent mobility may be explained by a two-dimensional disorder model with a Gaussian density of states (DOS). The width of the Gaussian was found to be 60meV for the SmB phase through simulation and by experimental observation. This small value is about half the typical value of 100~120meV observed in disorder organic materials, is characteristic of the SmLC.phases. The disorder model predicted the existence of a new field-dependent region at very high fields which had not been reported. So, we attempted to carry out the time-of-flight measurement of 8-PNP-O12 in an extended field region and found experimentally a mobility which depends on the electric field. We think that the validity of the present model has thus been confirmed experimentally. For SmB, SmE and SmA phases, we derived a disorder formalism to describe transport in a field-dependent region showing Poole-Frenkel-like mobility and, for the field-independent mobility region, we derived another formula

described by Eq. (6.13), which explains why we could not find temperature-dependent region in SLC. Some of these parameters reflect dimension and site configuration.

It was shown in Chapter 7 that the charge-carrier transport behavior, field- and temperature-dependence as demonstrated by TOF experiments, in smectic mesophases of biphenyl derivatives, may be well be described by a two-dimensional hopping transport model with a Gaussian-distributed density of states. By contrast, the charge carrier transport in the organic disordered materials is described by a three-dimensional disorder model.

The last Chapter was intended for a discussion of the consistency of energetic disorder as represented by the MTM and the GDM. Only a brief description was presented, however. We expect the present study will be extended to give a comprehensive understanding of charge transport properties of condensed organic materials covering a broad class of substances, from single crystals and liquid crystals, to amorphous materials including polymers and molecularly-doped polymers, thus contributing of our understanding of the relationship between molecular organization and photoelectric properties such as charge carrier transport under applied electric fields.

Understanding the microscopic behavior of carrier transport in smectic liquid crystals can provide a reliable guiding principle for designing molecules with improved transport properties.

8. Summary

List of Publications

Original publications relating to this thesis

1. **Akira Ohno** and Jun-ichi Hanna,
   "Simulated carrier transport in smectic mesophase and its comparison with experimental result"
   Applied Physics Letters, **82**, 751(2003) (in the chapter 6)

2. **Akira Ohno**, Kensuke Kurotaki, Akihide Haruyama, Masahiro Funahashi and Jun-ichi Hanna
   "Modeling of electronic charge transport in smectic liquid crystals"
   PROCEEDINGS OF SPIE Organic Photonic Materials and Devices **4991**,274 (2003) (in the chapter 6)

3. **Akira Ohno**, Jun-ici Hanna and David H. Dunlap
   "Extraction of trap distribution in organic semiconductors by transient photocurrnt spectroscopy"
   Japanese Journal of Applied Physics Pt2 Express Letter **43**, No.4A (2004) (in the chapter 3,5)

4. **Akira Ohno**, Jun-ici Hanna, Bijan Movaghar and Hiroaki Fujita
   "Monte Carlo simulation of carrier transport in crystalline phase of smectic liquid crystalline materials"
   Physical Review B to be submitted (Simulation method is related with the chapter 7)

International conferences and symposiums

1. **Akira Ohno** and Jun-ichi Hanna, "Modeling and Monte Carlo Simulation of Carrier Transport in Liquid Crystalline Semiconductor", Workshop on Hopping Transport in Organic Solids, ECOER'01, University of Potsdam, Germany (2001)

2. **Akira Ohno** and Jun-ichi Hanna, "Modeling and Simulation of Carrier Transport in Liquid Crystalline Semiconductor, American Physics Society March Meeting, Indianapolis, Indiana, U.S.A. (2002)

3. **Akira Ohno**, Jun-ichi Hanna and D.H. Dunlap, "Analysis of trap distribution for smectic liquid crystals using time of flight spectroscopy", Gordon Reserch Conference, Salve Regina University, Newport, RI, U.S.A. (2002)

4. **Akira Ohno**, Jun-ichi Hanna and D.H. Dunlap, "Analysis of trap distribution for smectic liquid crystals using time of flight spectroscopy", seminar on Department of Engineering Physics, Ecole Polytechnique de Montreal, Canada (2002)

5. **Akira Ohno**, Masahiro Funahashi, Akihide Haruyama Kensuke Kurotaki and Jun-ichi Hanna, "Modeling of electronic charge transport in smectic liquid crystals", SPIE Photonics West [4991-22] , San Jose, California, U.S.A. (2003).

6. Akira Ohno, Jun-ichi Hanna and D.H. Dunlap, "Analysis of trap distribution for smectic liquid crystals using time of flight spectroscopy", SPIE Photonics West [4991-24], San Jose, California, US.A (2003).

7. Akira Ohno, Jun-ichi Hanna and D.H. Dunlap, "Analysis of trap distribution for smectic liquid crystals using time of flight spectroscopy", American Physics Society March Meeting, Austen, Texas, U.S.A. (2003)

Domestic conferences and symposiums

1. 大野玲、舟橋正浩、半那純一、「液晶性有機半導体の伝導機構のモデル化とモンテカルロシミュレーション」；2001 年秋期応用物理学会学術講演会（名古屋工業大学、 平成 13 年 9 月）

2. 大野玲、舟橋正浩、半那純一、「液晶性有機半導体における電荷輸送のモデル化とシミュレーション」；日本液晶学会討論会 （大宮ソニックシティ、 平成 13 年 10 月）

3. 大野玲、半那純一、「液晶性有機半導体における低電場領域でのｱｲﾝｼｭﾀｲﾝの関係式の評価およびﾄﾗｯﾌﾟ密度の解析」；2002 年秋期応用物理学会学術講演会（新潟大学、平成 14 年 9 月）

4. 大野玲、半那純一、Bijan Movaghar、「有機半導体の結晶相における電荷輸送とモンテカルロシミュレーションによる検討」；2003 年秋期応用物理学会学術講演会（福岡大学、平成 15 年 8 月）

5. 大野玲、半那純一、D.H.Dunlap、「TOF 法を用いた有機半導体におけるトラップ密度分布の解析」；2003 年日本物理学会秋季大会（岡山大学、平成 15 年 9 月）

6. 大野玲、飯野裕明、半那純一、「不純物を含むスメクティック液晶における電荷輸送特性のダイナミクス」;2003 年日本液晶学会討論会 （青森市文化会館、平成 15 年 10 月）

Acknowledgement

This thesis is based on the research performed during the doctoral course at Imaging Science and Engineering Laboratory, Tokyo Institute of Technology, Japan, from October 2000 to March 2004, under the supervision of Professor Jun-ichi Hanna.

First of all, I would like to express my sincere appreciation to Professor Jun-ichi Hanna for his consistent guidance, helpful discussions and significant suggestions.

I wish to express my great appreciation to Associate Professor David H. Dunlap of University New Mexico for his helpful advices and discussions.

I wish to acknowledge also the immense help given by Dr. Bijan Movaghar of SOMS, University of Leeds, in his valuable comments and suggestions.

I would like to gratefully acknowledge to Dr. Masahiro Funahashi of Hanna laboratory for his valuable comments and useful discussions.

Special thanks are extended to Hiroaki Iino of Hanna laboratory for his useful suggestions and supports of beautiful Time-of Flight measurements.

In addition, I also thank all of other members of Hanna laboratory, especially, Ms. Yukiko Takayashiki, Dr. Naoki Yoshimoto, Hiromi Maeda, HyonSoo Ahn, Takahiro Kamitani, Hideaki Haruyama, Ryota Ohishi for their considerable discussions and encouragements in my doctoral course.

Finally, I heartily express my appreciation to my parents, Dr. Shin-ichi Ohno and Ms. Mizuho Ohno and my friends for their encouragements and supports during this study.

03/08/2004

大野玲

Akira Ohno